

Washington University in St. Louis

Washington University Open Scholarship

Engineering and Applied Science Theses &
Dissertations

McKelvey School of Engineering

Summer 8-15-2021

Investigation of Microdroplet Generation, Morphological Evolution, and Applications Under Quasi-steady and Dynamic States

Li Shan

Washington University in St. Louis

Follow this and additional works at: https://openscholarship.wustl.edu/eng_etds



Part of the [Mechanical Engineering Commons](#)

Recommended Citation

Shan, Li, "Investigation of Microdroplet Generation, Morphological Evolution, and Applications Under Quasi-steady and Dynamic States" (2021). *Engineering and Applied Science Theses & Dissertations*. 664. https://openscholarship.wustl.edu/eng_etds/664

This Dissertation is brought to you for free and open access by the McKelvey School of Engineering at Washington University Open Scholarship. It has been accepted for inclusion in Engineering and Applied Science Theses & Dissertations by an authorized administrator of Washington University Open Scholarship. For more information, please contact digital@wumail.wustl.edu.

WASHINGTON UNIVERSITY IN ST. LOUIS

Department of Mechanical Engineering and Materials Science

Dissertation Examination Committee:

J. Mark Meacham, Chair

Damena Agonafer, Co-advisor

Philip Bayly

Julio D'Arcy

Patricia Weisensee

Investigation of Microdroplet Generation, Morphological Evolution, and Applications Under
Quasi-steady and Dynamic States

by

Li Shan

A dissertation presented to
The Graduate School
of Washington University in
partial fulfillment of the
requirements for the degree
of Doctor of Philosophy

August 2021
St. Louis, Missouri

© 2021, Li Shan

Table of Contents

List of Figures	iv
List of Tables	ix
Acknowledgments.....	x
Abstract of the Dissertation	xii
Chapter 1: Introduction	1
1.1 Background and Motivation.....	1
1.2 Objectives.....	3
1.3 Outline.....	4
Chapter 2: Device concept, design and fabrication	6
2.1 Introduction	6
2.2 Hollow micropillars for sessile droplet generation	8
2.2.1 Design of hollow micropillars.....	8
2.2.2 Fabrication of hollow micropillars.....	10
2.3 Nozzle microarray for free droplet generation	16
2.3.1 Design of nozzle microarray	16
2.3.2 Fabrication of nozzle microarray	16
Chapter 3: Shape evolution of microdroplets in steady and dynamic states.....	18
3.1 Sessile microdroplets pinned on hollow micropillars	18
3.1.1 Experimental setup.....	18
3.1.2 Morphology evolution of the droplets pinned on hollow micropillars	20
3.1.3 Summary	28
3.2 Free microdroplets ejected from nozzle microarray	29
3.2.1 Experimental setup.....	32
3.2.2 Simulation Methodology.....	34
3.2.3 Results and discussion	40
3.2.4 Conclusion	54
Chapter 4: Implementations for sessile and free microdroplets.....	56
4.1 Introduction	56
4.1.1 Thin-film evaporation of pinned sessile droplets.....	56
4.1.2 The ejection behavior of the microdroplets ejected from an array of micronozzles.....	58
4.2 Evaporation from microdroplets confined on heated micropillar structures with different cross-section shapes	61
4.2.1 Experimental apparatus.....	61

4.2.2 Liquid vapor interface of pinned sessile droplet	64
4.2.3 Experimental methods.....	68
4.2.4 Results and discussion	70
4.2.5 Summary	86
4.3 Spray ejection from an array of micronozzles	87
4.3.1 Experimental apparatus.....	87
4.3.4 Summary	98
Chapter 5: Future work for the investigation of microdroplets under quasi-steady and dynamic states.....	100
5.1 Droplets under quasi-steady states	100
5.2 Droplets under dynamic states	101
References	103
Appendix.....	107
Appendix 1	107
Appendix 2	109
Appendix 3	111

List of Figures

Figure 1. A schematic demonstration of the increased perimeter-to-area ratio and higher surface curvature as the solid-liquid contact area of the droplet changes from a circle to a square and triangle. The comparison is made with all three droplets sharing the same solid-liquid contact perimeter and liquid-vapor interfacial area. Changing the solid-liquid contact shape from a circle to a square and a triangle respectively results in 13% and 29% increases in the perimeter-to-area ratio as well as 14% and 21% enhancements in the surface curvature, κ 2

Figure 2.1 Sessile droplet generation methods: hollow micropillar with different cross-section shapes. 7

Figure 2.2 Top view schematic of the contact line evolution of a droplet meniscus confined on a triangular pillar structure at different stages: **(a)** the contact line is pinned along the pore in the center of the micropillar; **(b)** the contact line expands freely with a circular shape on the top surface and just comes in contact with the outer edge of the micropillar; **(c)** part of the contact line gets pinned along the outer edge while part of the contact line starts to protrude into the corner area of the micropillar; **(d)** further expansion of the contact line as it protrudes into the corner area of the micropillar. 9

Figure 2.3 Fabrication flow charts of the samples for (a) pinning analysis and (b) heat transfer experiment. (c) The top view and the geometric dimensions for three micropillars: i) circular micropillar, (ii) square micropillar, and (iii) a triangular micropillar. 11

Figure 2.4 (a) Photographs of Batch 1 for (i) circular micropillar, (ii) square micropillar, and (iii) a triangular micropillar. (b) SEM images of Batch 1 for (i) circular micropillar, (ii) square micropillar, and (iii) a triangular micropillar. 12

Figure 2.5 (a) SEM isometric view images of the fabricated (i) circular micropillar, (ii) square micropillar, and (iii) a triangular micropillar. (b) Pt thin film region and the resistance temperature detector on the back side of the sample. (i) There are two connection pads for the RTD detector and two connection pads for the RTD heater near the center of the samples. The resistance detector and Pt thin film heater pattern occupied the region around the center of the samples. The small wire width of the Pt thin film patterns shown in (ii) have ~95% of the total electrical resistance. (iii) For the through hole at the center of each sample, the distance from the RTD elements to the through hole is 25 μm . The image was taken on a Kimwipe® tissue with a backside LED light. 14

Figure 2.6 Fabrication flow chart of nozzle microarrays. 17

Figure 3.1 (a) Schematic representation of the experimental setup: (1) particle filter, (2) minichamber degasser, (3) Pressure transducer, (4) Idex 3-way fitting, (5) camera. (b) Photograph of experimental platform setup for pinning experiments. 19

Figure 3.2 (a) Snapshots of a DI water droplet growing on a micropillar with a circular cross section taken at several time points. (b) Pressure curve during the growth of the DI water droplet on the circular micropillar. 22

Figure 3.3 (a) Snapshots of a DI water droplet growing on a micropillar with a square cross section taken at several time points. (b) Pressure curve during the growth of the DI water droplet on the circular micropillar. 23

Figure 3.4 (a) Snapshots of a DI water droplet growing on a micropillar with a triangular cross section taken at several time points. (b) Pressure curve during the growth of the DI water droplet on the triangular micropillar. 25

Figure 3.5 Snapshots of IPA solution (70% v/v) droplet growing on a (a) circular, (b) square, and (c) triangular micropillar. 27

Figure 3.6 Snapshots of Novec™ 7500 growing on a (a) circular, (b) square, and (c) triangular micropillar. 28

Figure 3.7 Summary of DI water, IPA, and Novec™ 7500 microdroplets growing on a circular, square, and triangular micropillar structure at different stages. 29

Figure 3.8 Computational modeling approach: (a) finite element analysis (FEA) domain including component geometry and applied boundary conditions (BC), (b) detail of the nozzle geometry and tip BC, (c) representative meshes used for mesh refinement and solution convergence, and (d) comparison of the electrical input impedance and pressure errors for coarse and fine meshes. 36

Figure 3.9 Comparison of model (finite element analysis) and experimentally measured (Picoscope) normalized electrical input impedances for the unloaded PZT/Al actuator over the frequency range 500 kHz to 2.5 MHz. 39

Figure 3.10 Normalized pressure contours in the liquid reservoir at the first resonance of (a) $f^{(1)} = 0.5$ MHz, $t_{res} = 1.56$ mm, (b) $f^{(1)} = 1$ MHz, $t_{res} = 0.56$ mm, and the second resonance of (c) $f^{(2)} = 1.5$ MHz, $t_{res} = 0.47$ mm, and (d) $f^{(2)} = 2$ MHz, $t_{res} = 0.29$ mm. 40

Figure 3.11 Five different liquid ejection moments observed in the experiments that were performed with an increasing input voltage and operated at the 2 MHz and 0.29 mm liquid reservoir height (2nd longitudinal resonance) with an orifice size of 15 μ m: (a) small and random droplets escaped from orifice, (b) straight jet or discrete droplet periodically ejected from orifice, (c) the liquid that just exited the orifice shows a screw-symmetric shape, (d) liquid is atomized by acoustic energy to form a cluster of small droplets, and (e) a large drop blocks the orifice. ... 43

Figure 3.12 The microscopic images of the liquid ejected from a 15 μ m orifice with an increasing input voltage at a frequency of (a) 0.5 MHz and a liquid reservoir height of 1.56 mm, (b) 1 MHz and a liquid reservoir height of 0.56 mm, (c) 1.5 MHz and a liquid reservoir height of 0.47 mm, and (d) 2 MHz and a liquid reservoir height of 0.29 mm. 45

Figure 3.13 The microscopic images of the liquid ejected from a 10 μ m orifice with an increasing input voltage at a frequency of (a) 0.5 MHz and a liquid reservoir height of 1.56 mm, (b) 1 MHz and a liquid reservoir height of 0.56 mm, (c) 1.5 MHz and a liquid reservoir height of 0.47 mm, and (d) 2 MHz and a liquid reservoir height of 0.29 mm. 46

Figure 3.14 The microscopic images of the liquid ejected from a 5 μ m orifice with an increasing input voltage at a frequency of (a) 0.5 MHz and a liquid reservoir height of 1.56 mm, (b) 1 MHz and a liquid reservoir height of 0.56 mm, (c) 1.5 MHz and a liquid reservoir height of 0.47 mm, and (d) 2 MHz and a liquid reservoir height of 0.29 mm. 48

Figure 3.15 Physical interpretation of the ejection process. Three orifices with different operating conditions are illustrated. 50

Figure 3.16 A regime map showing the five different ejection regimes including the small droplets region, droplet-on-demand region, transition region, jet region, and atomization region. The cases shown on the map also include our previous experimental data.....	53
Figure 4.1 (a) Schematic drawing of the experimental setup. (b) – (e) Photographs of the experimental setup. (b) and (e) show the expanded views of the evaporation platform and the fluid routing system, respectively.	63
Figure 4.2 Flow chart for determining the desired microdroplet geometries with the same liquid-vapor interfacial area and solid-liquid perimeter for droplets on circular, square, and triangular micropillars.	66
Figure 4.3 (a) – (c) shows an isometric view, top view, and cross section view of the equilibrium droplet profile on a square micropillar structure. (d) – (f) show an isometric view, top view, and cross section view of the equilibrium droplet profile on a triangular micropillar structure. The cross-section view shown in (c) and (f) are taken at three different azimuthal angles, α . The definition of the azimuthal angle is given in (b) and (e). The minimum and maximum local apparent contact angle, $\theta a, local$, are found at the directions with the smallest and largest azimuthal angles, respectively.....	67
Figure 4.4 Schematic representation of the two principal radii of curvature at the center of the side edge and at the corner for a droplet on a square micropillar.	68
Figure 4.5 (a) Profile of microdroplet on a circular micropillar from Surface Evolver. (b) Image of a droplet confined on a circular micropillar captured from experiments. The apparent contact angle, θa , of this capped sphere microdroplet is 72° . (c) Evaporative flux and the heat transfer coefficient for circular microdroplets at substrate temperatures ranging from $40^\circ\text{C} - 98^\circ\text{C}$	73
Figure 4.6 (a) Profile of microdroplet confined on a square micropillar from Surface Evolver. (b) Image of a microdroplet confined on a square micropillar captured from experiments. Both (a) and (b) are the microdroplet meniscus profile along the diagonal direction. (c) Evaporative flux and heat transfer coefficient for square microdroplets at substrate temperatures ranging from $40^\circ\text{C} - 98^\circ\text{C}$	73
Figure 4.7 (a) Profile of microdroplet on a triangular micropillar from Surface Evolver. (b) Image of a microdroplet confined on a triangular micropillar captured from experiments. Both (a) and (b) are the cross-sectional profile taken along the centerline of the micropillar top surface. (c) Evaporative flux and heat transfer coefficient for microdroplets on triangular micropillars with temperatures from $40^\circ\text{C} - 98^\circ\text{C}$	74
Figure 4.8 Heat transfer coefficients for three shapes of microdroplets from experiments and simulations. At all temperatures (from 40°C to 98°C), the heat transfer coefficient for triangular microdroplets is always the highest, 44.4% larger than that of a circular microdroplet at 60°C , and 71.2% larger than that of a circular microdroplet at 98°C . The difference is due to the slightly higher evaporation rate and the significantly smaller solid-liquid area (40% smaller than a circular micropillar top surface).....	76
Figure 4.9 (a) and (b) are temperature contours for droplets on circular, square and triangular micropillars at substrate temperatures of 40°C and 98°C , respectively. (c) and (d) are the vapor concentration profiles near the liquid-vapor interface at substrate temperatures of 40°C and 98°C , respectively.	78

- Figure 4.10** The distribution of the local conduction resistance along the radial direction taken at cross section planes with different azimuthal angles in an evaporating droplet on a (a) square and (b) triangular micropillar structure. With increasing normalized radial distance, the conduction resistance decreases sharply to zero due to the reduction in liquid thickness. At the same normalized radial distance, the conduction resistance decreases slightly with increasing azimuthal angle which represents an increase in the local liquid thickness when moving from the corner region to the center of the side edge of the asymmetric droplet. 81
- Figure 4.11** The radial distribution of the local diffusion resistance taken at cross-section planes with different azimuthal angles in an evaporating droplet on a square and triangular micropillar under different substrate temperatures. 82
- Figure 4.12** The change in the average conduction and diffusion thermal resistances for droplets evaporating on circular, square, and triangular micropillars at five different temperatures. 85
- Figure 4.13** Experimental setup: (a) schematic illustrating assembly of the PZT piezoelectric/ aluminum actuator, fixed nozzle microarray, and optional polyethylene thin film separator, (b) piezoelectric drive waveform V_{PZT} with burst period T_{burst} where signal is on for a period $n\tau$ and off for a period T_{off} (n is the number of cycles on; τ is the inverse of drive frequency f), (c) photograph of spraying experiment with labeled assembly components, and (d) top and side view images of the 13×13 nozzle silicon microarray. 89
- Figure 4.14** Effect of orifice size on sample spraying: (a) model (M) results showing the normalized pressure distribution within a reservoir of height $t_{res,M} = 0.5$ mm with orifice diameter $d_o = 10 \mu\text{m}$, $20 \mu\text{m}$, and $40 \mu\text{m}$ [the predicted first longitudinal resonant frequency $f_M(1) = 1.06$ MHz for all three cases], and (b) experimental (E) images of ejection from $10 \mu\text{m}$ -, $20 \mu\text{m}$ -, and (f) $40 \mu\text{m}$ -orifice nozzle microarrays obtained at the same operating frequency used in the simulations. 92
- Figure 4.15** Ejection modes for a fixed reservoir geometry. Model-predicted normalized pressure distributions and experimental observation of spraying from a $t_{res} = 0.5$ mm-height reservoir with $d_o = 10 \mu\text{m}$ orifices driven at the first three longitudinal resonances $f_M = f_E =$ (a) 1.06 MHz, (b) 1.60 MHz, and (c) 2.19 MHz. Model and experimental conditions are denoted by a subscript “M” and “E”, respectively. 93
- Figure 4.16** Effect of drive voltage: (a) pressure distribution, images of droplet ejection as a function of drive voltage, and model-predicted tip pressure gradients at the first longitudinal resonance of a 0.5 mm-height reservoir with orifice diameter $d_o = 10 \mu\text{m}$ [$f_M(1) = f_E(1) = 1.06$ MHz], and (b) results at the second longitudinal resonant frequency [$f_M(2) = f_E(2) = 1.60$ MHz]. 94
- Figure 4.17** Distributed, sparse ejection driven by lateral resonant modes: (a)-(c) model-predicted normalized pressure distributions, images of droplet ejection, and model-predicted tip pressure gradients at three lateral resonances (a) $f_E = 0.630$ MHz ($f_M = 0.625$ MHz), (b) $f_E = 0.808$ MHz ($f_M = 0.809$ MHz), and (c) $f_E = 0.920$ MHz ($f_M = 0.915$ MHz). The orifice diameter $d_o = 10 \mu\text{m}$ and the liquid reservoir height $t_{res} = 0.5$ mm for all cases. 95
- Figure 4.18** Multi-resonance operation by adjusting the liquid reservoir height: (a)-(d) images of droplet ejection and model-predicted normalized pressure distributions for excitation at $f_E = f_M = 1.00$ MHz and $V_{pp,E} = 300$ mV at gradually decreasing reservoir height: (a) $t_{res} = 2.73$ mm, (b) $t_{res} = 2.09$ mm, (c) $t_{res} = 1.13$ mm, and (d) $t_{res} = 0.60$ mm. 97

Figure 4.19 Use of a polyethylene film to bisect the liquid reservoir: (a)-(c) images of droplet ejection and model-predicted normalized pressure distributions for excitation at $f_E = f_M = 1.02$ MHz and $V_{pp,E} = 300$ mV with (a) no plastic film, and films positions such that (b) the film-to-microarray distance $t_{FM} = 1.0$ mm and (c) $t_{FM} = 1.5$ mm. The total liquid reservoir height was 2 mm in all cases..... 98

Figure A.1 The boundary conditions for the numerical simulation of microdroplets evaporating on heated micropillars. At far field, the vapor concentration and the temperature are assigned as the ambient condition (the relative humidity and temperature are 25% and 22°C); a vapor concentration boundary condition was assigned at the liquid-vapor interface, which equals to the local saturation concentration; a constant temperature boundary condition is applied at the pillar bottom surface; and all other walls are assigned as no-penetration boundary condition..... 114

List of Tables

Table 3.1 Working liquid properties and flow rates.....	20
Table 3.2 Summary of the critical bursting pressures and bursting volumes of DI water droplets on the circular, square, and triangular micropillars.	24
Table 3.3 Summary of the critical bursting pressures and bursting volumes of IPA and Novec™ 7500 droplets on the circular, square, and triangular micropillars.	25
Table 3.4 Model material properties.	35
Table 3.5 Summary of droplet sizes and the volume of liquid ejected from each cycle.....	49
Table 3.6 Summary of the time scales for the process (t_f), inertia (t_U), surface tension (t_σ), and viscosity (t_μ) for some ejection cases.....	54
Table 4.1 The thermophysical properties, Capillary number, and Bond number of the water microdroplet explored in this study.	65
Table 4.2 Experimentally measured evaporative flux and calculated heat transfer coefficients of the circular, square, and triangular microdroplets at different temperatures.	75
Table 4.3. The change in the conduction and diffusion resistances for droplets with different shapes evaporating at different substrate temperature conditions.	85
Table A.1 Dimensionless numbers and time scales for process, inertia, capillary, and viscosity for all cases investigated experimentally.	107
Table A.2. Simulation setup.....	114
Table A.3 Mesh independence study.	115

Acknowledgments

First and foremost, I would like to thank my parents, Guiyin Xie and Yihong Shan, without whose support I would not achieve this. I am so grateful for their endless understanding and encouragement.

I would like to thank my mentor during my bachelor's research in Hohai University, Zhen Zhang, who led me to enter the path of research, and with whose help I realized the real beauty of scientific research. Then, I would like to thank my first academic advisor in Washington University in St. Louis, Dr. Damena Agoanfer, who offered me the opportunity to study at a higher level. In the meantime, I sincerely thank Dr. Binjian Ma and Dr. Wenming Li, who provided me so much help during my two-year Ph. D. student life via both professional and personal support without any reservations. I also want to express my thanks to my second advisor in Washington University in St. Louis, Dr. J. Mark Meacham, who offered me a second chance and brought me back to academic research at the trough of my Ph. D. life, without whose help, I would have never successfully achieved so much.

Then, I would like to thank the professors in my committee, Dr. Patricia Weisensee, Dr. Julio D'Arcy, and Dr. Philip Bayly, who guided me and offered invaluable ideas. The support from other faculty members in the Department of Mechanical Engineering and Materials Science was also an invaluable resource to me, especially the aid from Dr. Jessica Wagenseil, from whom I experienced the utmost care from the university.

Last but not least, I would like to thank the previous and current members in both labs. They helped me a lot not only in my academic but also in my personal life. And I thank all my Chinese

friends I have met in my Ph.D. student life. Your kind support and care during these four years encouraged me and helped me overcome all the difficulties and challenges.

Li Shan

Washington University in St. Louis

August 2021

ABSTRACT OF THE DISSERTATION

Investigation of Microdroplet Generation, Morphological Evolution, and Applications Under Quasi-steady and Dynamic States

by

Li Shan

Doctor of Philosophy in Mechanical Engineering

Washington University in St. Louis, 2021

Dr. J. Mark Meacham, Chair

Dr. Damena Agonafer, Co-advisor

Microscale droplets are commonly encountered in the fields of materials processing, thermal fluids, and biology. While these droplets are naturally occurring, recent advances in microfabrication have enabled researchers to harness their enhanced transport characteristics for numerous laboratory and industrial applications from controlled chemical synthesis to inkjet printing and thermal management. Smaller droplets have larger specific surface area and a greater perimeter-to-area ratio when resting on a surface (i.e., sessile), which accelerates processes occurring at droplet surfaces like evaporation, chemical reaction, or combustion. The demand for microdroplets with smaller and more uniform sizes has motivated investigation of how such droplets can be created using robust and repeatable methods.

Here, I present a comprehensive study of the generation, morphological evolution, and the potential implementations of droplets formed under quasi-steady (sessile) and dynamic (spray) states. Sessile droplets were generated and retained by pumping water into hollow micropillar structures with different cross-sectional shapes. The sharp edges of the hollow micropillar structures create an energy barrier that hinders the further advance of the three-phase (liquid-

solid-gas) contact line, accompanied by an increase in the contact angle. This feature hinders the formation of flat liquid films on substrates, thus providing a longer triple phase contact line per unit area and potentially enabling the use of these structures in heat transfer devices. The shape evolution and evaporation rate of microdroplets pinned on micropillars with circular, square, and triangular cross-sections are investigated. For dynamic droplet studies, sprays comprising high velocity microdroplet clusters are generated using a micromachined nozzle array driven at ultrasonic frequencies by vibration of piezoelectric actuators, breaking the surface tension energy to create droplets. The microscopic evolution of the droplet profile, velocity, diameter, and ejection modes were investigated to evaluate atomization performance.

Pinned sessile microdroplets and fine sprays with uniform droplet sizes benefit different applications. For example, the steady droplet profile of pinned sessile microdroplets allows controllable evaporative cooling, while fine sprays are widely used for inkjet printing, combustion, and materials synthesis, among others. In this project, the heat transfer performance of droplets pinned on micropillars with different cross-sections was investigated, and the overall ejection behavior from nozzle microarrays was characterized. The dissertation work therefore consists of three components: (1) design and fabrication of hollow micropillars and arrays of microscopic nozzles/orifices, (2) investigation of the shape evolution of pinned sessile microdroplets and free droplet clusters in sprays, and (3) characterization of both the heat transfer performance of pinned microdroplets and the overall ejection behavior. Results elucidate the complex physics governing two different droplet formation regimes, while also directly applying observations to two emerging implementations of microdroplets.

Chapter 1: Introduction

1.1 Background and Motivation

Microscale droplets have been widely used in many fields, including biology¹⁻⁴, manufacturing⁵,⁶, and thermodynamics⁷⁻¹¹. By separating bulk liquids into smaller droplets, larger surface area is created that facilitates the energy and mass transport across the droplets' surfaces and accelerates processes occurring at droplet surfaces like evaporation, chemical reaction, or combustion. In addition, the isolated microenvironment in each droplet enables the single cell analysis under precise spatial and temporal control.

Most microdroplets can be classified into two categories: sessile droplets states and free droplets, just like dew and rain. The sessile droplets are the droplets resting on a substrate or confined on microstructures, which are usually considered as a quasi-steady state. The free droplets usually have certain velocities and are in a dynamic state. Many industrial and academic research applications utilize one of these two droplet forms, such as sessile droplets for single-cell analysis and free droplets for aerosol synthesis, or sometimes both (spray coating and spray cooling).

For most of the droplet-based applications, the size of the droplets determines their efficiency. For example, the thermal resistance of a microdroplet increases as it grows in size, thus, larger droplets weaken the thermal performance of heat exchangers. While droplets shrink in sizes, they exhibit a larger ratio between the perimeter and interfacial solid-liquid area (A_{sl}), as shown in Figure 1.1. In addition, a larger average curvature, κ , can be achieved by tuning the droplet profile. A large curvature induces a higher vapor concentration gradient in the vicinity of the liquid-vapor interface, while a larger perimeter-to-surface area ratio allows for a greater fraction

of heat transport from the contact line region, both of which can lead to a higher evaporation rate.

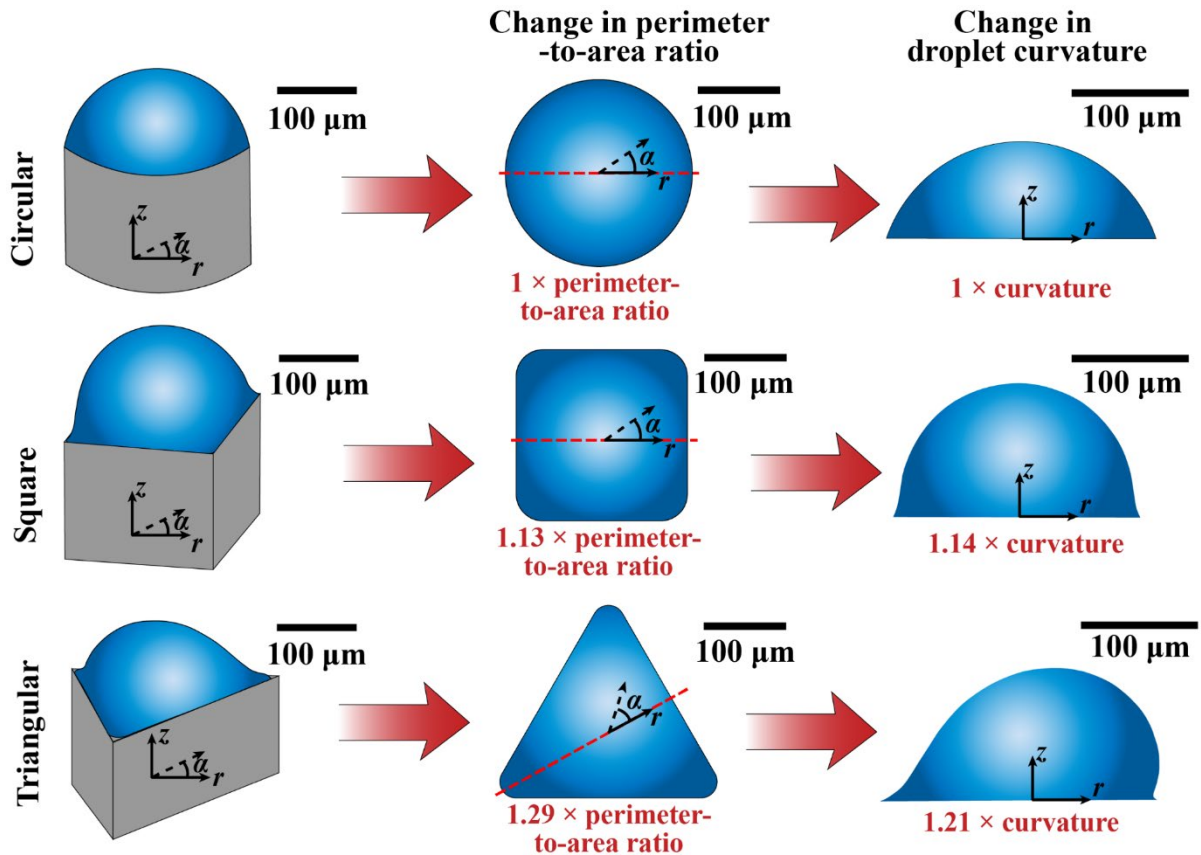


Figure 1. A schematic demonstration of the increased perimeter-to-area ratio and higher surface curvature as the solid-liquid contact area of the droplet changes from a circle to a square and triangle. The comparison is made with all three droplets sharing the same solid-liquid contact perimeter and liquid-vapor interfacial area. Changing the solid-liquid contact shape from a circle to a square and a triangle respectively results in 13% and 29% increases in the perimeter-to-area ratio as well as 14% and 21% enhancements in the surface curvature, κ .

For free droplets, the breakup of a bulk liquid into small droplets also creates a larger surface area to accelerate reactions with the surrounding environment and/or enhance heat and mass transfer. Traditional spray systems exploit a high relative velocity between the working liquid and surrounding gases to disrupt the liquid-gas interface. The resultant Plateau–Rayleigh instability causes the liquid to break up, creating a wide range of droplet sizes.¹² The increasing

demand for controllable, uniform droplets [e.g., for cell and biomaterial handling,^{2, 13-15} aerosol drug delivery,¹⁶⁻¹⁹ materials synthesis,^{6, 20} and three-dimensional (3-D) printing²¹⁻²⁵] has increased interest in discrete droplet [including so-called droplet-on-demand (DOD)] generators that offer exquisite control and precise droplet size. For example, aerosolized drug droplets with a diameters from 1–5 μm are required for effective delivery at different lung depths,¹⁶ therefore achieving improved treatment outcomes. Controllable microdroplet generation also enables additive manufacturing of materials with higher resolution.²¹

Thus, the droplet generation methods that provide the ability to control droplet sizes and produce uniform droplets will benefit these applications. In this study, the controllable droplet generation methods for sessile droplets and free droplets were investigated; the droplet profiles and the potential implementations in various applications were studied.

1.2 Objectives

The overall objective of this work is to investigate the generation, morphological evolution, and applications of droplets formed under quasi-steady (sessile) and dynamic (spray) states. Sessile droplet generation and retention will be realized by pumping water into hollow micropillar structures with different cross-section shapes. The sharp edges of the hollow micropillar structures create an energy barrier that hinders the further advance of the three-phase (liquid-solid-gas) contact line, accompanied by an increase in the contact angle²⁶⁻²⁹. This feature of hollow micropillar structures hinders the formation of flat liquid films on substrates, thus providing a longer triple phase contact line per unit area and potentially enabling the use of these structures in heat transfer devices³⁰⁻³². The shape evolutions and evaporation rates of microdroplets pinned on micropillars with circular, square, and triangular cross-sections will be

investigated. Sprays, high velocity microdroplet clusters, will be generated by an ultrasonic nozzle microarray that utilizes the high-frequency vibration of piezoelectric actuators to break the surface tension energy and create droplet clusters^{9, 33-36}. The dynamic evolution of the droplet shape profile, velocity, and flow rate will all be characterized to evaluate the atomization performance. Pinned sessile microdroplets and fine sprays with uniform droplet sizes can benefit different applications. For example, the steady droplet profile of pinned sessile microdroplets allows controllable evaporative cooling³⁰⁻³², while fine sprays are widely used for inkjet printing³⁷⁻³⁹, combustion, material synthesis⁴⁰⁻⁴², liquid-crystal display (LCD) fabrication⁴³⁻⁴⁵, and biochips⁴⁶⁻⁴⁸. In this project, the heat transfer performance of droplets pinned on micropillars with different cross-sections will be investigated and the macro ejection behavior of the nozzle microarrays will be studied. To sum up, the dissertation work consists of three parts: (1) fabricating hollow micropillars and nozzle microarrays, (2) investigating the shape evolution of pinned sessile microdroplets and droplets in sprays, and (3) characterizing both the heat transfer performance of pinned microdroplets and the potential materials synthesis behavior of sprays.

1.3 Outline

A brief summary of all chapters and their contents is given below:

The current chapter (Chapter 1) provides a background on the microdroplets classification, different droplet generation methods, and the droplet-based applications. In addition, an overview of the whole research was described in this chapter.

Chapter 2 describes the proposed two droplet generation methods, and production of sessile droplets or free droplets with uniform sizes, as well some other important parameters. The fabrication methods for both droplet generators are given. In addition, to characterize the droplet morphology of the generated sessile droplets and free droplets, a special sample for each droplet

generator was fabricated.

Chapter 3 describes the characterization of the behaviors and morphologies of generated sessile and free droplets. The hollow micropillar structures enable the confinement of sessile droplets on their top surfaces and the volume of the liquid supplied from the inner holes of the micropillars together with their cross-section shapes are able to tune the droplet morphology. The nozzle microarray system utilizes the acoustic energy to break liquid into small droplets. The microscopic ejection behavior of the microdroplets generated from a single orifice at different orifice sizes and operation frequencies was investigated. Five different ejection modes were studied, and a regime map obtained from experimental data was plotted to predict the ejection modes.

Chapter 4 describes the potential implementations of the pinned sessile droplets and free droplets in a heat-transfer and spray system. The thermal behavior of the sessile droplet pinned on heated hollow micropillars with different cross-section shapes was investigated. And the results showed that with the same liquid contact line and interfacial area, droplets pinned on triangular micropillars possessed a larger evaporation rate due to less confinement and smaller total thermal resistance. As for the spray generated from a nozzle microarray at longitudinal resonances, the pressure gradient in the liquid reservoir dominates the on/off mode. A higher pressure gradient at the center of the nozzle microarray resulted in an earlier ejection behavior, while the smaller pressure gradient at the periphery suggests a larger input power is required for those nozzles to eject.

Chapter 5 provides the direction of the future works for droplet generation and characterization under quasi-steady and dynamic states.

Chapter 2: Device concept, design and fabrication

2.1 Introduction

Precise droplet generation methods for both sessile and free droplets enable the higher efficiency and better performance for all droplet-based applications.

The desired attributes for sessile droplet generation techniques include the controllability over:

- **Droplet volume:** The volume of a sessile droplet is the most essential parameter for a sessile droplet.
- **Contact angle:** The contact angle determines the mobility and the morphology of the sessile droplet. A droplet with a smaller contact angle, resting on a hydrophilic surface, is flatter than it is with a larger contact angle, resting on a hydrophobic surface, thus leading to a smaller thermal resistance across the droplet. In addition, when the contact angle of a droplet is larger than 90° , the diffusion of the vapor molecules is hindered at the triple contact line, therefore, resulting in a smaller evaporation flux.
- **Liquid-vapor interfacial area:** The liquid-vapor interfacial area determines the heat and mass transfer rate at the droplets' surfaces. In addition, it also determines the reaction rate for the chemical reaction processes that occur at the droplets' surfaces. Thus, a larger liquid-vapor interfacial area benefits performance of the sessile-droplet-based applications.

In this study, the sessile droplet generation is realized by 1) confining a droplet on a micropillar structure, 2) changing the micropillar cross-section shape (circle, triangle, and square) to modify

the morphology and curvature of the pinned droplet, 3) continuously supplying the working liquid from a through hole at the center of the sessile droplet, and 4) controlling the volume, contact angle, and liquid-vapor interfacial area of the pinned sessile droplet by the inlet pressure. A schematic drawing of the studied sessile droplet generation method is shown in Figure 2.1.

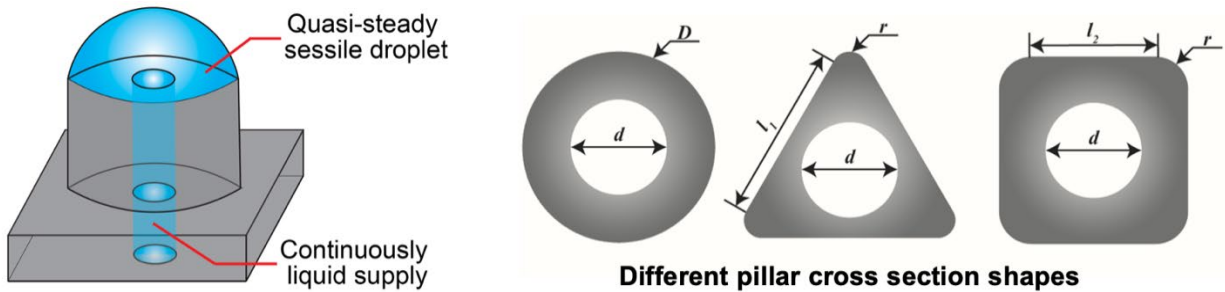


Figure 2.1 Sessile droplet generation methods: hollow micropillar with different cross-section shapes.

The desired attributes for free droplet generation techniques include the controllability over:

- **Droplet diameter:** The diameter of a free droplet determines the liquid vapor interfacial area and the liquid volume. The precise control over droplet diameter provides the accurate liquid delivery and controllable chemical reaction rate.
- **Velocity:** The droplet velocity determines the delivery rate of the working fluid. For certain applications, such as spray cooling, the velocity of the ejected droplets affects the impact behavior on the target substrate. Thus, a controllable droplet velocity is desired.
- **Mass flow rate:** A controllable mass flow rate is always desired for a free droplet generator and it is the most essential parameter.

In this study, the free droplet generation is realized by 1) generation of acoustic energy from a piezoelectric ceramic and then transferring energy to the liquid chamber where a large pressure gradient develops and forms near the nozzle exits, 2) nozzle size roughly determines the ejected

droplet diameter, while the working frequency of the piezoelectric ceramic is able to tune the droplet diameter, and 3) pressure contour pattern can be tuned by the operating frequency which will affect the fraction of ejecting nozzles and eventually change the mass flow rate.

2.2 Hollow micropillars for sessile droplet generation

2.2.1 Design of hollow micropillars

When a sessile droplet forms and grows on a hollow micropillar with a circular cross-section shape, the contact line of the droplet maintains a circle shape while growing in diameter. It will pin at the pillar edge perfectly when the contact line reaches the pillar edge. However, such criterion does not hold for an asymmetric droplet advancing atop a non-circular pillar. As shown in Figure 2.2, the liquid meniscus initially remains in capped spherical shape during expansion before the contact line touches the outer edge of the micropillar. During this stage, the droplet meniscus profile is solely dependent on the surface wettability, and the shape of the wetted area does not coincide with the shape of the micropillar tip. As the liquid volume keeps increasing, the contact line will pin at the midpoint of each line segment along the outer edge of the micropillar tip, leaving a considerable portion of top surface non-wetted near the corner locations. With further increase in liquid volume, the meniscus will wet along each side edge and move towards the corner regions. At this point, the morphology of the liquid droplet starts to deviate away from a capped spherical geometry, where the apparent contact angle, θ_a , increases faster near the midpoint of the side edge than near the corner region. Finally, as the liquid volume continues to increase, the liquid meniscus near the center of the side edge will eventually form a critical local apparent contact angle, θ^* , defined by Gibbs' inequality and start to burst along the side wall, while the liquid meniscus still advances towards the corner regions. In other words, for triangular and square micropillars there will always be a finite area near the corner

region of the micropillar substrate that remains unwetted regardless of the droplet volume. In addition, to fabricate hollow micropillars with very sharp corners is also challenging. Thus, a rounded corner with a small diameter was adopted and will not affect the pinning and burst behavior of the droplets.

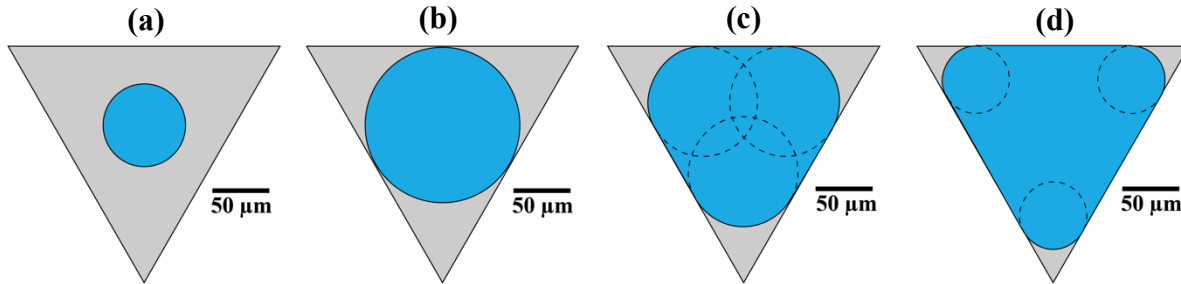


Figure 2.2 Top view schematic of the contact line evolution of a droplet meniscus confined on a triangular pillar structure at different stages: **(a)** the contact line is pinned along the pore in the center of the micropillar; **(b)** the contact line expands freely with a circular shape on the top surface and just comes in contact with the outer edge of the micropillar; **(c)** part of the contact line gets pinned along the outer edge while part of the contact line starts to protrude into the corner area of the micropillar; **(d)** further expansion of the contact line as it protrudes into the corner area of the micropillar.

The through-hole diameter that supplies the working fluid from the bottom of the pinned droplet does not affect the liquid morphology while the contact line detaches from the inner through-hole and advances on the pillar top surface. However, a smaller through-hole diameter results in a larger friction loss in the pressure, therefore, leading to a higher pumping pressure. Thus, the diameter of the inner through-hole is designed to be equal to one half of the circle pillar diameter. In addition, both the interfacial area and the contact line play important roles in evaporation. Therefore, the designed outer perimeters of all three micropillars are the same. In this study, two batches of the hollow micropillar samples are fabricated. One with a larger diameter, 500 μm , for the droplet morphology analysis and one with a smaller diameter, 100 μm , for the heat transfer experiments. The pinned sessile droplets on the micropillars from both batches have a very small Bond number, therefore, the effect of the gravitational force can be

neglected, and the droplet morphology follows a scaling law.

2.2.2 Fabrication of hollow micropillars

For both batches of the samples, the techniques used in micropillar fabrication are the same, however, the smaller micropillars for heat transfer experiments also include two patterned platinum thin films, one working as a heater and the other as a resistance temperature detector. The fabrication flow chart of the micropillar samples for pinning analysis (Batch 1) is shown Figure 2.3 (a). The geometric dimensions shown in the design are $d = 250 \mu\text{m}$, $D = 500 \mu\text{m}$, $r = 50 \mu\text{m}$, $l_1 = 314 \mu\text{m}$, and $l_2 = 419 \mu\text{m}$. At first, a double-sided polished wafer was cleaned using RCA-1 silicon wafer cleaning method. A thin oxide layer ($\sim 450 \text{ nm}$) was grown on both sides of the silicon wafer by heating the wafer in a tube furnace (Lindberg/Blue M) at $1100 \text{ }^\circ\text{C}$ for 14 hours. This oxide layer works as the hard mask for the DRIE process. Then photolithography and reactive-ion etching (RIE) were used to get a through-hole in the micropillar center. And then the micropillar patterns were fabricated using photolithography and RIE. At last, oxide layer on the frontside of the Si wafer and all the photoresist was removed. The photographs and the SEM images of the micropillars for the pinning analysis are shown in Figure 2.4.

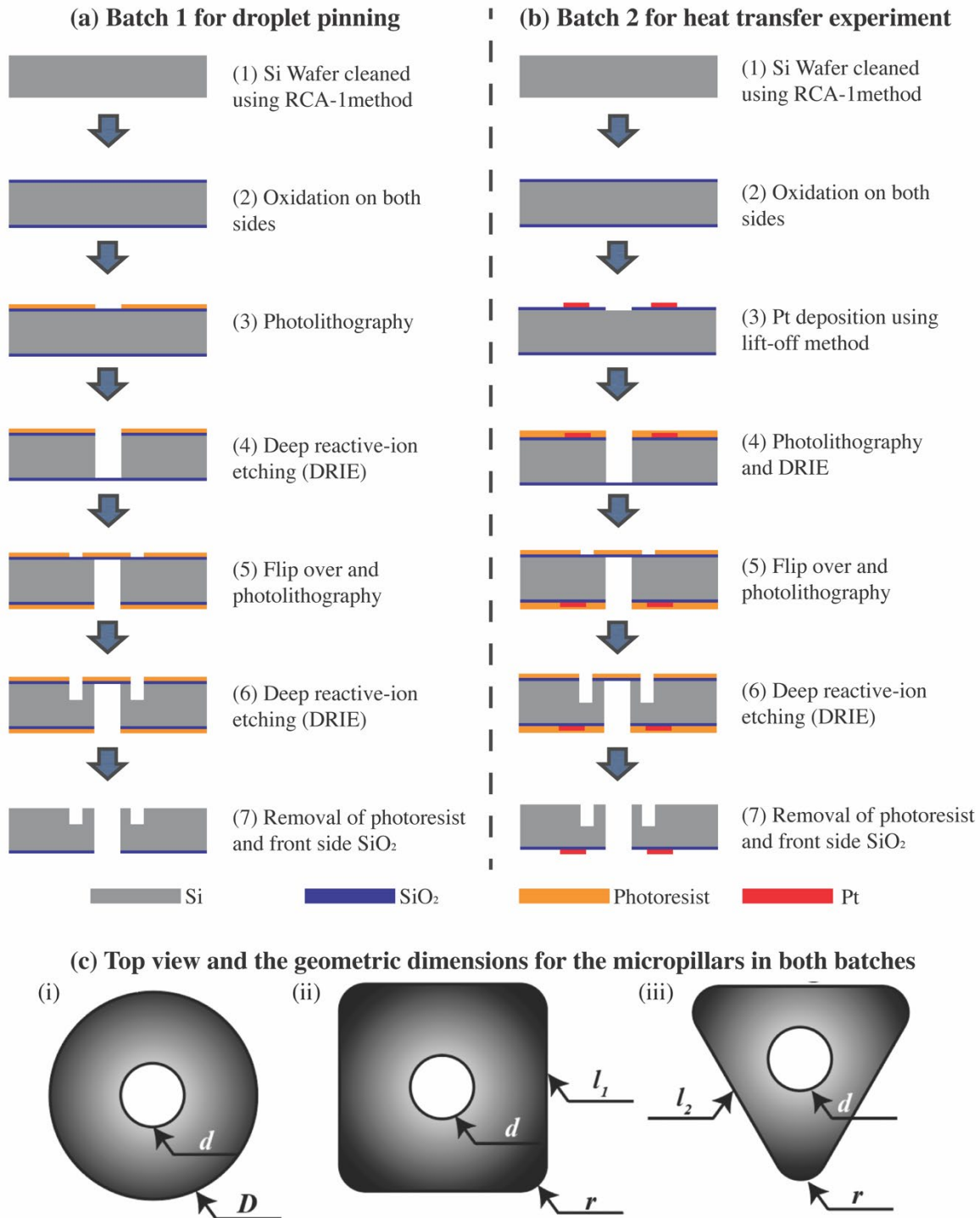
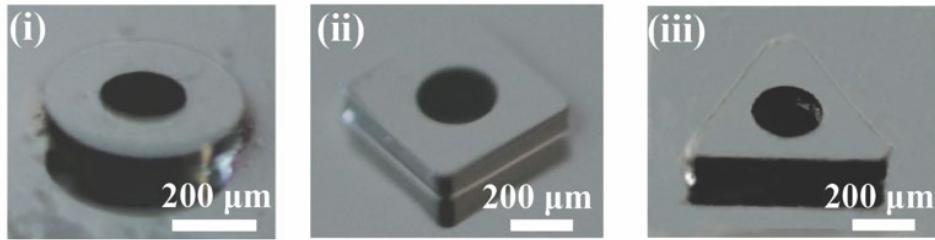


Figure 2.3 Fabrication flow charts of the samples for (a) pinning analysis and (b) heat transfer experiment. (c) The top view and the geometric dimensions for three micropillars: i) circular micropillar, (ii) square micropillar, and (iii) a triangular micropillar.

(a) Photographies of micropillars for Batch 1



(b) SEM images of micropillars for Batch 1

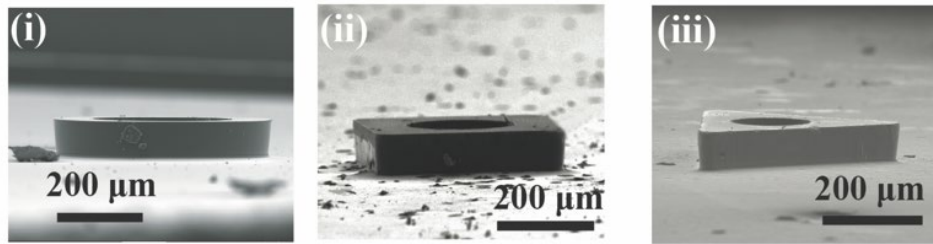
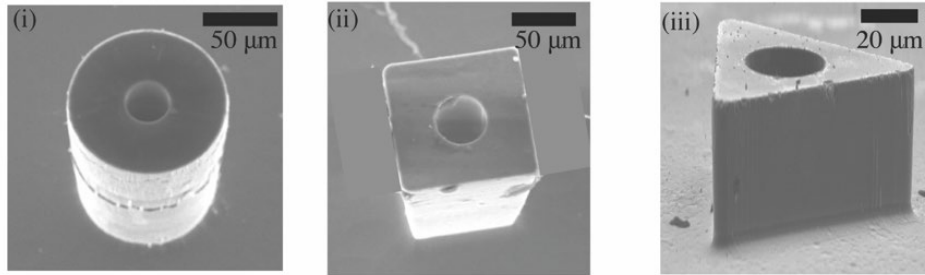


Figure 2.4 (a) Photographies of Batch 1 for (i) circular micropillar, (ii) square micropillar, and (iii) a triangular micropillar. (b) SEM images of Batch 1 for (i) circular micropillar, (ii) square micropillar, and (iii) a triangular micropillar.

The fabrication process for the samples used in heat transfer experiments (Batch 2) is shown in Figure 2.3 (b). The geometric dimensions shown in the design are $d = 50 \mu\text{m}$, $D = 100 \mu\text{m}$, $r = 10 \mu\text{m}$, $l_1 = 62.8 \mu\text{m}$, and $l_2 = 83.8 \mu\text{m}$. The first two steps are the same as Batch 1, however, the thin oxide layer also works as a passivation layer because it can prevent the potential current leakage from the heating and temperature sensor units during the heat transfer experiment. Subsequently, two 125 nm thick platinum resistance temperature detectors (RTD), which function as the heat source and temperature sensor separately, were deposited on the back side of the wafer by sputtering (Kurt J. Lesker, PVD 75) and lift-off. During this process the redundant metal layers were removed by submerging the wafers in Remover PG at 60 °C for 12 hours. A 25 nm thick chromium layer (Cr) was used as the adhesion layer to ensure strong bonding between the platinum and the silicon surface. As shown in Figure 2.5 (b)(i), the RTD patterns were designed to have a

relatively large width ($\sim 20 \mu\text{m}$) near the bonding pads shown as the four large squares on the four corners, but a much smaller width ($\sim 5 \mu\text{m}$) near the center of the sample. Such features cause the central section of the platinum RTD to contribute more than 95% of the total resistance ($\sim 380 \text{ ohm}$ for RTD sensors and $\sim 230 \text{ ohm}$ for RTD heaters), which therefore enables these RTD elements to measure the temperature and provide heat input at locations very close to the center of the sample. After the fabrication of the RTD elements, a deep hole was formed in the center of the silicon wafer by first removing the oxide layer with RIE and then removing the silicon with deep reactive ion etching (DRIE). Both processes were initiated from the backside of the wafer (i.e., the same side where RTD elements are deposited) and performed in the same RIE chamber (Oxford Instrument, Plasmalab System 100). It should be noted that during the DRIE process, the hole just reached the oxide layer on the front side of the sample but did not penetrate the entire wafer completely. This condition was ensured by illumination of the sample from the backside and observation of the bright light spot on the front side. Finally, three different micropillars with a circular, square, and triangular cross section were fabricated on the front side of the silicon wafer by photolithography, RIE, and DRIE. The final SEM images of the three micropillars are shown in Figure 2.5 (a). The optical images of the platinum RTD elements and the through hole on the backside of the sample are shown in Figure 2.5 (b).

(a) SEM isometri view images of micropillars for Batch 2



(b) Pt thin film heater and resistance temperature detector for Batch 2

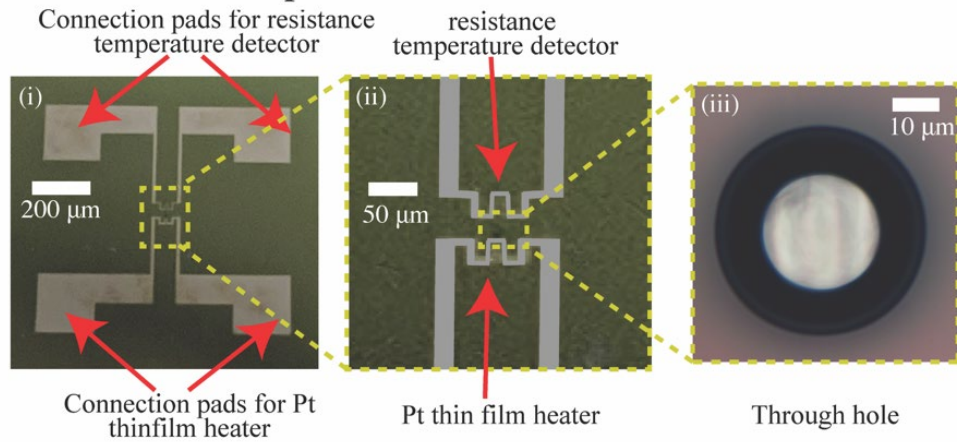


Figure 2.5 (a)SEM isometric view images of the fabricated (i) circular micropillar, (ii) square micropillar, and (iii) a triangular micropillar. (b) Pt thin film region and the resistance temperature detector on the back side of the sample. (i) There are two connection pads for the RTD detector and two connection pads for the RTD heater near the center of the samples. The resistance detector and Pt thin film heater pattern occupied the region around the center of the samples. The small wire width of the Pt thin film patterns shown in (ii) have ~95% of the total electrical resistance. (iii) For the through hole at the center of each sample, the distance from the RTD elements to the through hole is 25 μm. The image was taken on a Kimwipe® tissue with a backside LED light.

After finishing the fabrication of the hollow micropillar structures, the samples were first cleaned in an ultrasonicator (Branson, CPX-952-216R, USA) at a frequency of 40 kHz for 30 minutes to remove chemical residue. Afterwards, the Batch 2 samples were dried with compressed nitrogen and four copper wires (McMaster-Carr, 7304K21, UL Recognized, Flame Rated VW-1, gauge 29) were bonded to the four connection pads using silver paste (MG Chemicals, 473-1220-ND, USA).

As discussed previously, one RTD element is used to provide the heating power while the other RTD element is used to measure the sample temperature. Therefore, two copper wires were used to connect one RTD element to a DC power source and the other two copper wires were used to connect the other RTD element to the multimeter. Since the electrical resistance of the copper wire is very small (< 0.1 ohm), these copper wires have negligible effect on the resistance of the RTD element. After applying silver paste to the samples, they were then cured in an oven at 100 °C for 6 hours. Finally, after the ultrasonication cleaning of Batch 1 samples and the bonding process of copper wires for Batch 2 samples, NanoPort (IDEX Health and Science, N-333, USA) connectors were aligned with the through holes of the micropillars and bonded to the backside of the samples using J-B weld epoxy (J-B Weld, cold weld 8280, USA). The alignment between the center of the NanoPort and the center of the through hole was confirmed by illuminating the sample from the front side and observing the light coming out from the outlet of the NanoPort connector.

Before mounting the Batch 2 sample on the thermal test platform, two RTD elements fabricated on the back side of the samples were calibrated in an oven (Fisher, Isotemp 15-103-0503, USA) from 30 °C to 100 °C with intervals of 10 °C, and the temperature stability of this oven is ± 0.4 °C. The electrical resistance of both RTD elements were recorded by a multimeter (Keithley Instruments, DMM7510) during the calibration. The relationship between the temperature and electrical resistance was fitted by a linear curve with a coefficient of determination, $R^2 > 0.99$. This linear trend is consistent with past literature studies on the electrical characteristics of platinum^{49,50}. During the evaporation experiments, the substrate temperature is determined by the electrical resistance of one RTD element based on the calibration curve.

2.3 Nozzle microarray for free droplet generation

2.3.1 Design of nozzle microarray

In this study, the overall ejection behavior of the whole microarray and the dynamic droplet morphology of the liquid ejecting from one nozzle of the microarray are investigated. The ejection modes for different orifice diameters are investigated. It is easy to study the overall ejection behavior for a nozzle microarray that consists of 13×13 nozzles by taking macroscopic images using a commercial camera that focuses on the first row of the microarray. However, to study the droplet dynamics of the liquid ejecting from any target nozzle becomes difficult, such as the 7th nozzle on the 7th row, due to the interference of spraying from nearby nozzles. Therefore, two batches of the nozzle microarrays were fabricated, with one for the overall ejection behavior analysis and another one for the droplet dynamic morphology analysis. For the former batch of samples, all nozzles in the microarray have the same orifice size. As for the latter batch of samples, only the target nozzle that is going to be studied for microscopic droplet morphology has a predefined orifice size, and all other nozzles have a much smaller orifice ($\sim 1 \mu\text{m}$) to create a large energy barrier at nozzle tips and to suppress the liquid ejection while the trapped air bubbles in liquid chamber are able to escape from such small orifices during filling. In addition, to make a fair comparison between the images taken under macro- and microscales, the acoustic field for both samples should be the same while operating. From our previous research, a minor effect of the nozzle sizes on the overall acoustic field was found. Thus, the smaller orifices only hinder the ejection from the unwanted nozzles without affecting the overall acoustic field.

2.3.2 Fabrication of nozzle microarray

The fabrication processes for both batches of the samples are the same and the flow chart is shown in Figure 2.6. Nozzle microarrays with different diameters were fabricated from a double-

side polished silicon substrate [(100)-oriented, 100-mm diameter, 500- μm thick; University Wafer] precoated on both sides with a silicon nitride (Si_3N_4) masking layer [$\sim 650\text{-nm}$ thick, low pressure chemical vapor deposited (LPCVD); Georgia Institute of Technology Institute for Electronics and Nanotechnology]. Features were patterned using standard photolithography, reactive ion etching (RIE) of square windows in the nitride film, and anisotropic potassium hydroxide (KOH) wet etching of Si to form pyramidal nozzle structures. It should be noted that 10% w/w IPA solution was added to the KOH solution to reduce the fluid surface tension and enable the quick escape of H_2 bubbles from the Si surface. Then, back side alignment was used to locate orifices at the nozzle tips, and circular orifices were prescribed by deep reactive ion etching (DRIE). Each microarray comprised 13×13 nozzles, spaced $70 \mu\text{m}$ apart. After fabrication, the wafer was diced into individual microarrays measuring $25 \text{ mm} \times 25 \text{ mm}$.

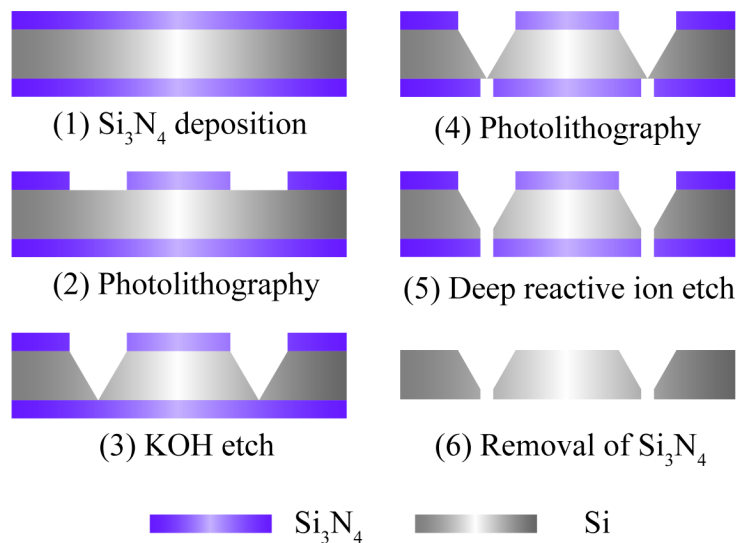


Figure 2.6 Fabrication flow chart of nozzle microarrays.

Chapter 3: Shape evolution of microdroplets in steady and dynamic states

3.1 Sessile microdroplets pinned on hollow micropillars

3.1.1 Experimental setup

In order to explore the pinning behavior of symmetric and asymmetric droplets, a series of hollow micropillar structures with different cross-sectional shapes was prepared on a silicon substrate following the microfabrication process described in Chapter 2.2.2.

Liquid pinning experiments were performed on circular, square, and triangular hollow micropillar structures using three different working fluids: deionized (DI) water, isopropyl alcohol (IPA) (Sigma–Aldrich, St. Louis, MO, USA, CAS Number: 67-63-0), and the dielectric liquid 3M™ Novec™ 7500 (ChemPoint, Rockford, IL, USA). A programmable syringe pump (Cole Parmer, syringe pump Touch Screen 100) was used to feed the working fluids to the top surface of each micropillar structure through a PEEK tube (IDEX) with an inner diameter of 0.5 mm. A NanoPort Assembly (IDEX) was used to connect the tube to the backside of the micropillar substrate, which was altogether mounted on a machined metal frame. During the experiment, liquid pressure was monitored by a microfluidic gauge pressure sensor (MPS0, Elveflow®) with a measuring range of 6894 Pa and collected using a microfluidic flow control system (OB1 MK3, Elveflow®). Simultaneously, the profiles of the droplets during the expansion were captured using a CMOS digital SLR camera (Canon, Rebel Ti6) and a microscopic objective lens (InfiniProbe™ TS-160, magnification = 0 – 16, working distance (WD) = 18mm, NA > 0.16). Figure 3.1 shows a schematic drawing and a photograph of the experimental setup. When doing the experiments, the pumping rate for syringe pump was set and the working liquids went through the particle filter, degasser and pressure transducer in serial, to remove

the insoluble particles, remove dissolved gases and measure the liquid pressure, respectively. When a flat meniscus formed at the micropillar tip, camera started to record the videos for pinning behavior and the DAQ started to collect the pressure data.

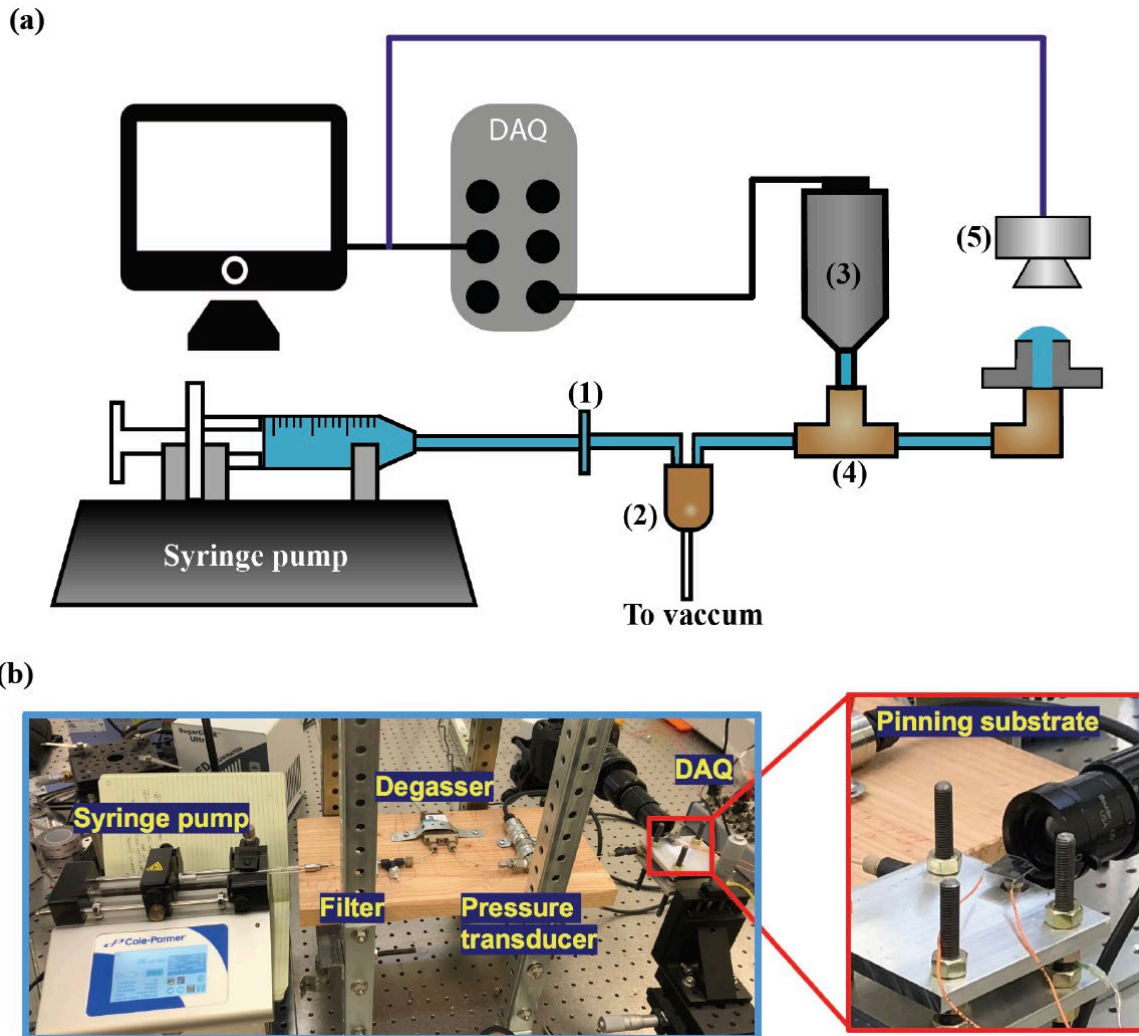


Figure 3.1 (a) Schematic representation of the experimental setup: (1) particle filter, (2) minichamber degasser, (3) Pressure transducer, (4) IDEX 3-way fitting, (5) camera. (b) Photograph of experimental platform setup for pinning experiments.

For each shape and working fluid combination, the pinning experiment was performed at a constant flow rate with three repeated runs as shown in Table 3.1. The thermophysical properties of each working fluid, the corresponding capillary numbers (Ca), and the Bond (Bo) numbers

associated with a droplet diameter of 500 μm are also listed in the table. The capillary number is given by

$$Ca = \frac{\mu v}{\gamma} \quad (3.1)$$

where, μ , v and γ are the dynamic viscosity, velocity, and surface tension of the working fluid, respectively. The Bond number is given by

$$Bo = \frac{\Delta\rho g L_c^2}{\gamma} \quad (3.2)$$

where $\Delta\rho$ is the density difference between the liquid and air, g is the gravitational acceleration, and L_c is the characteristic length (i.e. the radius) of the droplet. All the capillary numbers, Ca , are found to be less than or at the same order of magnitude of 10^{-5} . This suggests that any dynamic effects are negligible in this experiment. In addition, the Bond numbers (Bo) are found to be smaller than 0.1 for all cases which suggests gravitational effects are negligible.

Table 3.1 Working liquid properties and flow rates.

Liquid	DI water	70% v/v IPA solution	Novec™ 7500
Surface tension (N/m)	0.072	0.023	0.016
Dynamic viscosity (kg/m·s)	8.9×10^{-4}	2.44×10^{-3}	1.24×10^{-3}
Liquid density (kg/m ³)	1000	858	1600
Flow rate (uL/min)	1	1	1
Capillary number	4.1×10^{-6}	3.5×10^{-5}	2.6×10^{-5}
Bond number	8.5×10^{-3}	2.3×10^{-2}	6.1×10^{-2}

3.1.2 Morphology evolution of the droplets pinned on hollow micropillars

First, the morphology evolution of DI water pinned and grown on hollow micropillars with different cross-sections was captured. Figure 3.2 (a) shows the experimental visualization of a water droplet growing on a micropillar with a circular cross-sectional shape. The snapshots show

the following five moments: (i) the liquid meniscus becomes flat at the inner pore and begins to emerge on the top pillar surface; (ii) the contact line comes in contact with the outer edge of the micropillar structure; (iii) the liquid forms a hemispherical microdroplet where the radius of curvature is minimized; (iv) the microdroplet attains the maximum volume before bursting over the outer edge; and (v) the microdroplet spills over the outer edge of the micropillar and wets the surrounding substrate. The wicking and pivoting stages during the advancement of the liquid through the hollow micropillar cannot be visualized due to its opacity. After the liquid meniscus emerges on the top surface of the hollow micropillar structure, it first expands freely on the top surface until its contact line comes in contact with the outer edge of the micropillar structure. During this stage, the contact angle of the droplet remains constant. However, the growth of the droplet is found to be anisotropic on the top surface, where the right-side contact line comes in contact at the outer edge of the micropillar first. This anisotropy is most likely due to the non-uniform roughness of the top surface which causes the droplet to expand preferentially in one direction, which can be attributed to the variation in the free energy barrier required for the contact line to overcome the heterogeneous surface topography features at the microscale⁵¹⁻⁵³. As soon as the contact line comes in contact with the outer edge of the micropillar, the contact angle of the droplet starts to increase as the droplet grows further to cover the entire top surface. Since the intrinsic contact angle, θ_y , of the water droplet is less than 90° , the droplet forms a hemispherical shape during its expansion on the top surface (represented by point iii in Figure 3.2 (a)). Afterwards, the droplet continues to grow vertically on the micropillar structure in a capped spherical shape until the apparent contact angle, θ_a , exceeds the critical contact angle, θ^* , after which the droplet bursts over the outer edge of the micropillar structure.

Figure 3.2 (b) shows the change in liquid pressure during the growth of the water droplet on the circular micropillar structure. Two significant drops in pressure are observed at $t = 25$ s and $t = 254$ s, respectively. The first pressure drop ($t = 25$ s) occurs after the droplet gets pinned and expands beyond a hemisphere at the outer edge of the micropillar. This behavior is expected, since a hemispherical shape corresponds to a minimum radius of curvature during the entire expansion process. In other words, the droplet pressure reaches a maximum value, Δp_{max} , when its radius of curvature is minimized. The second distinct pressure drop ($t = 254$ s) occurs when the droplet spills over the outer edge of the hollow micropillar. This sudden drop is attributed to the fact that the pressure barrier associated with the change in total interfacial energy exerted by the sharp edge can no longer hold the liquid when the apparent contact angle, θ_a , exceeds the critical contact angle, θ^* . Therefore, the liquid droplet pinned on the micropillar structure collapses into a flat meniscus on the surrounding substrate ($t = 255$ s).

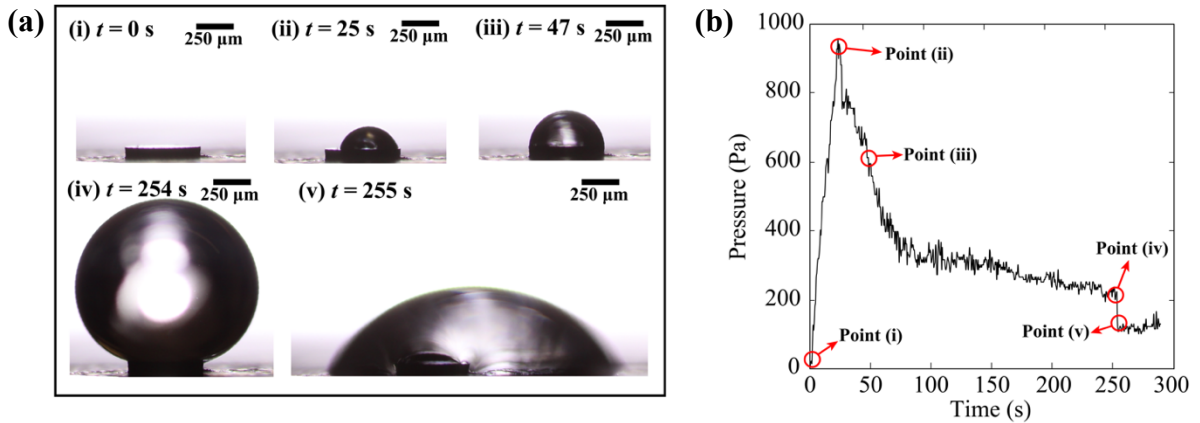


Figure 3.2 (a) Snapshots of a DI water droplet growing on a micropillar with a circular cross section taken at several time points. (b) Pressure curve during the growth of the DI water droplet on the circular micropillar.

Figure 3.3 shows the experimental visualization of a water droplet growing on a micropillar with a square cross-sectional shape and the corresponding change in the liquid pressure. The evolution of the meniscus profile and droplet pressure follow very similar trends with those of the circular

micropillar. Two sudden drops in pressure are observed which are associated with the maximum Laplace pressure and the burst pressure, respectively. In particular, the maximum pressure is reached before the droplet wets the entire top surface (represented by point ii in Figure 3.3a), because the liquid cannot penetrate completely to the corner regions on the top surface of a square micropillar. Therefore, once the contact line arrives at the outer edge of the micropillar structure, any further increase in droplet volume will result in a non-homogeneous expansion of the droplet profile along different radial directions. Specifically, the droplet starts to grow more near the center of the micropillar side edge, accompanied by a rapid increase in the local contact angle, θ_l . This growth results in a highly non-uniform contact angle along the contact line of the droplet as well as an asymmetric meniscus profile. Such an asymmetric profile causes the liquid-vapor interfacial area to increase faster than it would for a capped spherical droplet, since a spherical shape always possesses the minimum surface area under the same volume.

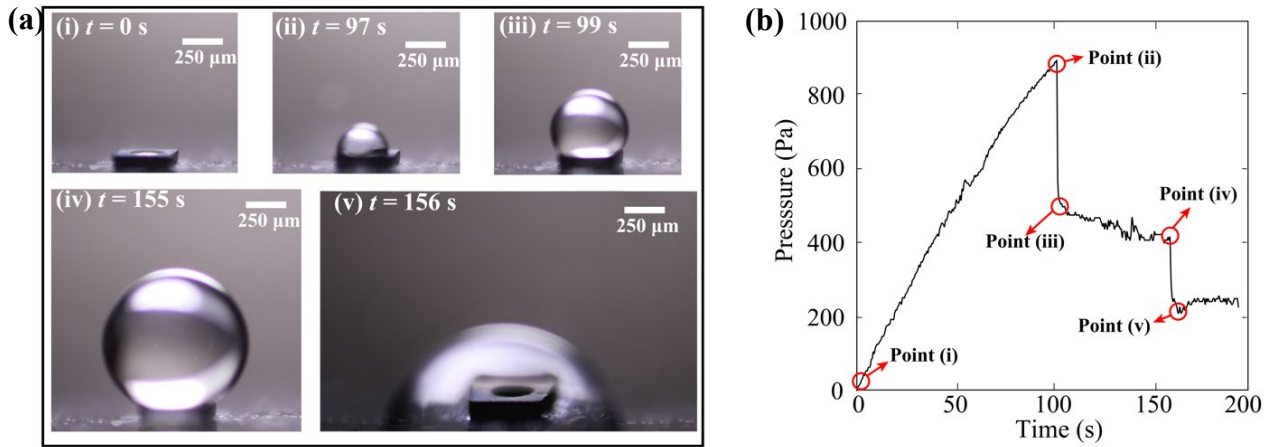


Figure 3.3 (a) Snapshots of a DI water droplet growing on a micropillar with a square cross section taken at several time points. (b) Pressure curve during the growth of the DI water droplet on the circular micropillar.

Figure 3.4 shows the experimental visualization of a water droplet growing on a micropillar with a triangular cross-sectional shape and the corresponding change in the liquid pressure. Table 3.2 summarizes the bursting volume and the bursting pressure for DI water droplets pinned on hollow micropillars with three cross-section shapes. In Figure 3.4 two substantial pressure drops associated with the maximum Laplace pressure and burst pressure are observed during the growth of the droplet. However, the time delay between these two pressure drops is reduced significantly for the water droplet expanding on the triangular micropillar, which is attributed to the smaller critical volume that can be retained by the triangular micropillar compared to a square (71% less) or circular micropillar (95% less). As a result, the droplet expanding on the triangular micropillar bursts earlier from the outer edge after it surpasses the maximum pressure point. In addition, the pressure trace shows that the droplet growing on a triangular micropillar exhibits the highest burst pressure. The higher burst pressure is caused by the smaller radius of curvature of the droplet advancing on the triangular micropillar. Therefore, a higher burst pressure represents a weaker liquid retention capability due to a smaller volume of liquid which can be supplied to the microdroplet.

Table. 3.2 Summary of the critical bursting pressures and bursting volumes of DI water droplets on the circular, square, and triangular micropillars.

Shape	CIR	SQU	TRI
Bursting volume (μL)	1.108	0.158	0.046
Bursting pressure (Pa)	225	430	652

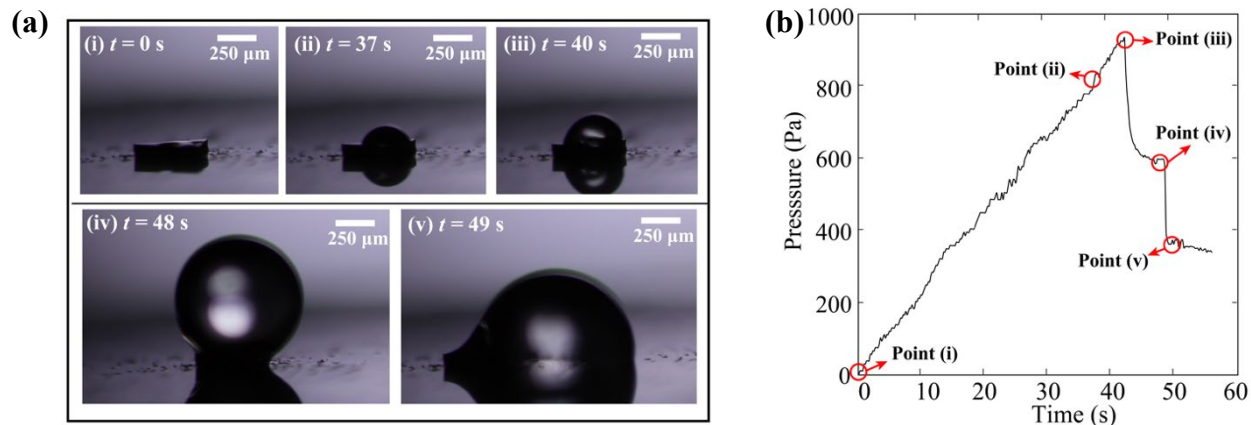


Figure 3.4 (a) Snapshots of a DI water droplet growing on a micropillar with a triangular cross section taken at several time points. **(b)** Pressure curve during the growth of the DI water droplet on the triangular micropillar.

In addition, the same experiments were performed with IPA solution (70% v/v) and Novec™ 7500. Table 3.3 summarizes the bursting volume and the bursting pressure for IPA solution (70% v/v) and Novec™ 7500 pinned on hollow micropillars with three cross-section shapes.

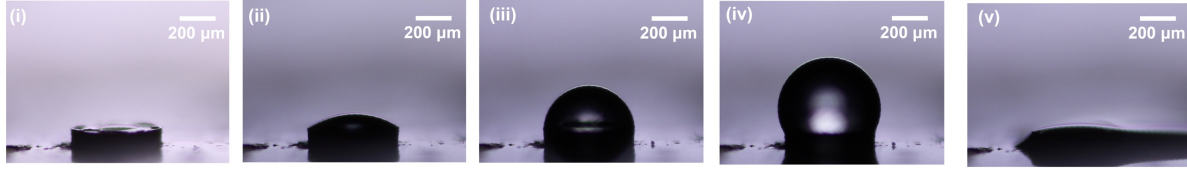
Table 3.3 Summary of the critical bursting pressures and bursting volumes of IPA and Novec™ 7500 droplets on the circular, square, and triangular micropillars.

Liquid	70% v/v IPA solution			Novec™ 7500		
	CIR	SQU	TRI	CIR	SQU	TRI
Bursting volume (μL)	0.063	0.017	0.011	0.041	0.014	0.010
Bursting pressure (Pa)	173	262	310	128	180	217

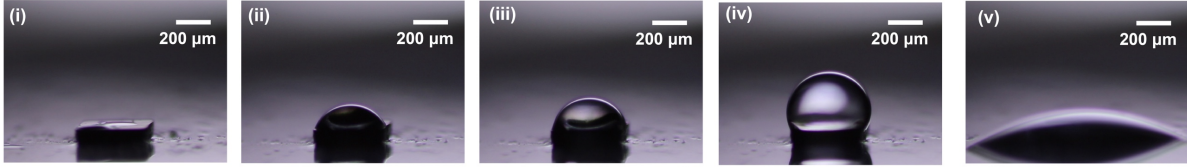
Figure 3.5 shows the snapshots of IPA solution (70% v/v) droplet growing on a circular, square, and triangular micropillar. For each shape, the first image (i) is taken when the liquid meniscus becomes flat at the inner pore, the second image (ii) is taken when the contact line just comes in contact with the outer edge of the micropillar, the third image (iii) is taken when the maximum

local contact angle reaches 90° , the fourth image (iv) is taken when the microdroplet attains the maximum volume before bursting over the outer edge, and the fifth image (v) is taken when the microdroplet spills over the outer edge of the micropillar and wets the surrounding substrate. The overall expansion behavior of an IPA droplet on the hollow micropillar structure is very similar to that of water, where the droplet first expands radially on the top surface until the contact line comes in contact with the outer edge of the micropillar structure. Afterwards, the droplet grows vertically, accompanied by an increase in the apparent contact angle, until it bursts over the micropillar structure. The critical burst volume of the IPA droplet on the square micropillar is 73% smaller than that on the circular micropillar, much like the behavior of a water droplet growing on the same micropillar structure. However, on all micropillars, the critical volume of the IPA droplet is found to be smaller than that of a water droplet, which is attributed to the lower surface tension of the IPA solution which yields a smaller critical contact angle at the bursting moment. Since the intrinsic contact angles of water and IPA solution are 67° and 20° , respectively, their critical bursting contact angles at the outer edge of the micropillar structure are 157° and 110° , respectively. Such results are consistent with the experimental visualization shown in Figure 3.3 and 3.5. Correspondingly, both the maximum and burst Laplace pressure of IPA droplets are therefore significantly smaller than those of water droplets.

(a) Circular micropillar



(b) Square micropillar



(c) Triangular micropillar

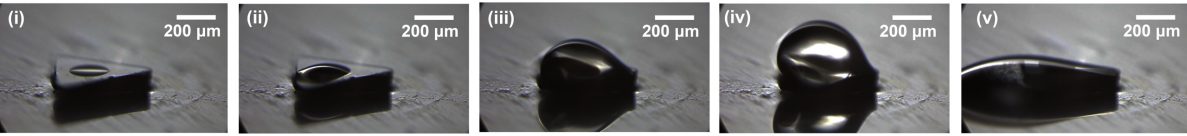
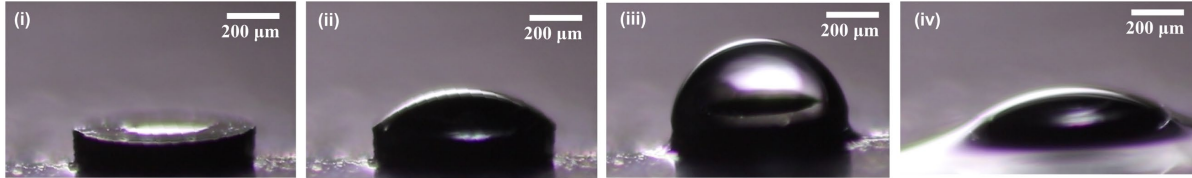


Figure 3.5 Snapshots of IPA solution (70% v/v) droplet growing on a **(a)** circular, **(b)** square, and **(c)** triangular micropillar.

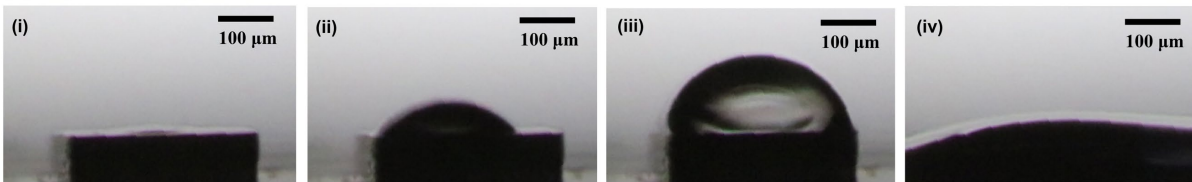
Figure 3.6 shows the snapshots of Novec™ 7500 growing on the circular, square, and triangular micropillar. For each shape, the first image (i) is taken when the liquid meniscus becomes flat at the inner pore, the second image (ii) is taken when the contact line just comes in contact with the outer edge of the micropillar structure, the third image (iii) is taken when the maximum local contact angle reaches 90° before bursting over the outer edge, and the fourth image (iv) is taken when the microdroplet spills over the outer edge of the micropillar and wets the surrounding substrate. The expansion of the droplet on all the micropillars follows the similar pattern with the tests using IPA solution. However, for expansion on both circular and square micropillars, the microdroplets were found to burst immediately when it approaches a hemispherical shape, i.e., the moment when the contact angle reaches 90° . Such behavior is attributed to an intrinsic contact angle, $\theta_y = 0$ for Novec™ 7500 resulted from its extremely low surface tension. As shown by equation 1, the critical burst contact angle of Novec™ 7500 on the outer edge of the micropillar structure is 90° irrespective of the cross-sectional shape of the micropillar.

Nevertheless, the non-uniform contact angle of Novec™ 7500 droplet on the square micropillar structure still yields a smaller critical volume and a larger burst Laplace pressure than that on the circular micropillar.

(a) Circular micropillar



(b) Square micropillar



(c) Triangular micropillar

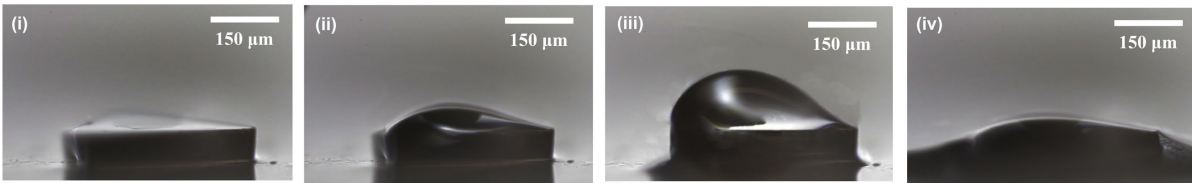


Figure 3.6 Snapshots of Novec™ 7500 growing on a **(a)** circular, **(b)** square, and **(c)** triangular micropillar.

3.1.3 Summary

A summary of droplet morphologies of different working fluids during the expansion on three different micropillar structures is shown in Figure 3.7. The photos were taken at three different stages: (1) transition from free expansion on the top surface to pinning along the outer edge; (2) forming a geometry close to a hemisphere with a maximum Laplace pressure; and (3) at the burst moment. For the same working fluid, the circular micropillar can retain the largest volume of droplet followed by the square and triangular micropillars. For the same micropillar, the DI water droplet always exhibits the largest critical volume at the bursting moment followed by IPA and Novec™ 7500. For Novec™ 7500, the shape of the droplet is identical at the maximum Laplace

pressure and the bursting moment since the Novec™ 7500 droplet bursts immediately at the maximum Laplace pressure moment. In general, for micropillars with the same cross-sectional shape, the critical contact angle of the water droplet at the bursting moment is the largest among the three working fluids, because the surface tension of water is much larger than that of the other two working fluids. The high surface tension enables the water droplets to form a larger contact angle and therefore a larger critical volume before bursting occurs. For Novec™ 7500, the extremely low surface tension hinders the expansion of droplets, and the critical contact angle was found to be the smallest among all three working fluids. Therefore, the maximum volume and height of Novec™ 7500 microdroplets is the smallest among all three working fluids.







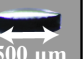











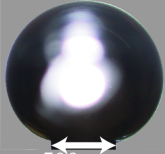
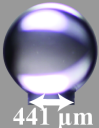

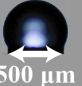
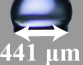

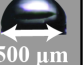


Working fluid Shape Stage	DI water			IPA			Novec™ 7500		
	CIR	SQU	TRI	CIR	SQU	TRI	CIR	SQU	TRI
(1)	 500 μm	 441 μm	 421 μm	 500 μm	 441 μm	 421 μm	 500 μm	 441 μm	 421 μm
(2)	 500 μm	 441 μm	 421 μm	 500 μm	 441 μm	 421 μm	 500 μm	 441 μm	 421 μm
(3)	 500 μm	 441 μm	 421 μm	 500 μm	 441 μm	 421 μm	 500 μm	 441 μm	 421 μm

Figure 3.7 Summary of DI water, IPA, and Novec™ 7500 microdroplets growing on a circular, square, and triangular micropillar structure at different stages.

3.2 Free microdroplets ejected from nozzle microarray

With the development of bioprinting⁵⁴⁻⁵⁷, material synthesis^{6, 20}, and droplet based additive material manufacturing⁵⁸⁻⁶⁰, the increasing demand for controllable droplet generation methods attracts more research. Uniform droplet clusters with controllable droplet sizes enhance the

performance of most droplet-based applications. For example, in a bioprinting setup, the generated droplet diameter determines the printing resolution⁵⁴. Therefore, the generators that yield a smaller droplet size have better control over the printed geometries. However, the printing time increases significantly with the decrease in ejected droplet diameter, therefore, a controllable ejection is desired for such applications.

Nozzle spray is a common way to generate discrete droplets where liquid is pushed out from a reservoir by a larger inlet pressure. When larger nozzle diameters operate at such high inlet pressure, the ejected liquid is torn apart by thermodynamic forces and converted into small droplets. This breakup behavior is chaotic and therefore leads to a droplet cluster with a random droplet size distribution⁶¹. However, when the nozzle orifice size is small or the inlet pressure is low, the liquid is gently pumped out of the reservoir in a continuously cylindrical form and breaks up downstream due to the combined effect of both surface tension, viscous forces, and aerodynamic forces⁶². The characterization of this ejection/breakup behavior has been investigated for over 100 years and based on the aerodynamic forces acting on the ejected liquid (or the ejected liquid velocity), the breakup of the liquid jet was characterized into five regions: (1) dripping mode as the droplet accumulates at the orifice until the liquid drips (2) Rayleigh breakup when surface tension causes the pinch-off of a liquid jet and form uniform droplet sizes⁶³⁻⁶⁵, (3) first wind induced breakup when the aerodynamic forces become important and act on the ejected liquid and bend the liquid jet against the surface tension force⁶⁶⁻⁷¹, (4) second wind breakup as the aerodynamic forces become even larger causing an unstable wavy jet followed by a conical spray due to the surface rupture⁷¹, and (5) atomization as the aerodynamic forces are strong enough to break up liquid into extremely fine droplets that are much smaller than the orifice size as liquid exits the nozzle^{72, 73}. In addition, Rayleigh connected the acoustic disturbance with ejected liquid by investigating the

instability due to disturbance on the ejected liquid and found that when the wavelength is smaller than the circumference of an undisturbed jet, the liquid jet tends to be in an unstable state⁶⁴. Nowadays, many ultrasonic droplet generation methods use this theory by applying an acoustic disturbance before the liquid is pumped out of the nozzle orifice by inlet pressure⁷⁴⁻⁷⁶.

In addition, if the acoustic energy itself is large enough to overcome the energy barrier at the nozzle orifice, a pressure inlet can be discarded which leads to a pure ultrasonic droplet generation. In these devices, acoustic energy is first generated by a piezoelectric actuator and then focused in a nozzle structure leading to the orifice. The large pressure gradient created by the acoustic force results in a larger inertia near the nozzle orifice and eventually overcomes the surface tension and ejects liquid from the orifice. Different nozzle structures were developed by researchers, such as straight channels^{77, 78}, conical tapers⁷⁹, and horn structures⁸⁰. Although many ultrasonic droplet generation methods have been proposed, investigated, and applied, the fundamental ejection behavior is not fully characterized, especially for the ejection and breakup phenomena at microscale and MHz frequencies of actuation.

In our previous studies, we reported the ultrasonic droplet generation using nozzles with an inverted pyramid shape that can be actuated from 500 kHz to 2.5 MHz^{8, 34, 35, 76}. We demonstrated the device can be used for many fluids with different surface tensions and viscosities^{8, 76, 81}. In addition, we developed a model that can be used to predict the operating resonances and the efficiency of the device⁸². Moreover, to gain insights into the ejection behavior near the nozzle orifices, we designed a micro-visualization system that was able to capture the microscopic ejection/breakup behavior. However, only a small number of operating conditions were investigated due to limitations of the experimental setup. Recently, an open-environment experimental platform that is able to adjust the operating frequency, input voltage, and liquid

reservoir height was designed and built. With this set up we realized the resonance operation at any given frequency, and macroscopic characterization of the ejection behavior was thoroughly investigated. Here, we incorporated the microscopic visualization system into this newly developed experimental platform to thoroughly investigate the microscopic ejection and break up behavior.

3.2.1 Experimental setup

The droplet morphology experimental setup consists of three parts: a sample mounting platform, a visualization system and signal generation system. For the sample mounting platform, all the components were mounted on an optical rail (XT95B-400, Thorlabs). A custom-machined support that mounted on a rail carriage (XT95RC4, Thorlabs) was used to fix the fabricated nozzle microarray. The piezoelectric actuator assembly that consists of a 1.5 mm thick lead zirconate titanate (PZT) ceramic (APC 880, American Piezo Ceramics) and 2 mm thick aluminum matching layer was affixed on a custom-machined hanger, which was then mounted on a translation stage (XRN25P and XT95RC4, Thorlabs) that attached to the optical rail via a rail carriage (XT95RC4, Thorlabs). The total travel length of the translation stages was 25 mm with a resolution of ± 25 μm . Thus, the liquid chamber height, i.e., the distance between the piezoelectric actuator assembly and the nozzle microarray, can be adjusted manually during the experiments.

In the microscopic visualization platform, an infinity corrected microscope lens (10 \times M Plan Apo, Excelitas Optem[®]) that provides a long working distance of 34 mm and numerical aperture of 0.30 was connected to an Optem[®] Fusion 12.5:1 optical zoom module (35-41-10-000, Excelitas), a 3 \times 600 FL mini camera tube (35-08-16-000, Excelitas), and a CCD camera (Infinity3-6UR, Teledyne Lumenera) in serial. The micro-visualization system provided a

magnification ranging from 8.4 to 104, a resolution ranging from 1.85 μm to 0.56 μm , and a numerical aperture ranging from 0.09 to 0.30. The system was then mounted on an optical rail (XT66-500, Thorlabs) and affixed to a rotation stage (XRR1, Thorlabs) to provide a precise angular control ($\pm 0.31^\circ$) with respect to the plane of the nozzle openings. At last, an XYZ three-axis translation stage (PT3A, Thorlabs) was used to support all the components described above and control the visualization location with a resolution of $\pm 25 \mu\text{m}$ in each direction.

When trying to capture the morphologies of the droplets ejected from a certain target nozzle, neither commercial or high-speed cameras would work, because the droplet ejection takes place in a very small period (ranging from 500 ns to 2000 ns), and an even smaller exposure time (1/10 of the ejection cycle) is required to study the evolution of droplet morphologies. In such a small exposure time, the camera sensors cannot acquire enough photons to capture an image with high resolution. However, since the events for droplet ejection are periodic, a long exposure time can be achieved if a synchronized square signal with 10% duty cycle at the same frequency as the signal used for piezoelectric actuation is applied at the illuminating LED light. Therefore, three synchronized signals are required for the signal generation system: (1) triggering camera, (2) illuminating LED light, and (3) driving piezoelectric actuator. A pulse signal with a voltage of 3.5 V and a width of 4 ms was used for the triggering of the camera. In addition, this signal was also used to trigger a function generator (33522A, Agilent), which generated two synchronized waveforms: one amplified sinusoidal signal (250L RF power amplifier, ENI) for the piezoelectric actuator, and the other a square wave with 10% duty cycle for the LED illumination. It should be noted that there is a delay of 150 ns between the camera trigger signal and function generator due to the interconnecting wires and device response. This delay was considered in the later analysis.

3.2.2 Simulation Methodology

To gain insight into the ejection performance of the open reservoir system, the commercial software COMSOL Multiphysics[®] was used to model the system harmonic response and acoustic wave behavior within the liquid domain. Due to the complexity of the physical system and limited computational resources, a fully three-dimensional (3-D) simulation was not feasible. Therefore, a simplified two-dimensional (2-D) planar domain with a symmetry boundary condition was used to achieve a reasonable computation time. Figure 3.8 (a) and (b) shows the assembly configuration and model geometry of the spraying system. The model comprised four domains (a piezoelectric element, aluminum coupling layer, liquid reservoir, and silicon nozzle microarray), representing the four components of the assembled experimental system. The thicknesses of the piezoelectric ($t_{PZT} = 1.5$ mm), aluminum layer ($t_{Al} = 2$ mm), and silicon microarray ($t_{Si} = 0.5$ mm), and the width of the microarray ($w_{Si} = 25$ mm) were fixed at values corresponding to the real components. The width of the piezoelectric was set to the average of its two lateral dimensions, i.e., $w_{PZT} = 30$ mm. The widths of the aluminum layer and liquid reservoir were set equal to that of the microarray to simplify the geometry, i.e., $w_{Al} = w_{res} = 25$ mm. The liquid reservoir height t_{res} and the orifice diameter d_o were variables. For each simulation case, the drive frequency was swept from 500 kHz to 2.5 MHz at an increment of 5 kHz. Table 3.4 summarizes the material properties used in the simulation. Thermal effects were neglected, and all materials were assumed to be at 23°C.

Table 3.4 Model material properties.

Symbol	Quantity	Value
ρ_{water}	density, water	997 kg/m ³
c_{water}	speed of sound, water	1481 m/s
ρ_{Al}	density, aluminum	2734 kg/m ³
E_{Al}	elastic modulus, aluminum	76.5 GPa
ν_{Al}	Poisson's ratio, aluminum	0.324
ρ_{Si}	density, silicon	2331 kg/m ³
E_{Si}	elastic modulus, silicon	150 GPa
ν_{Si}	Poisson's ratio, silicon	0.21
ρ_{PZT}	density, piezoelectric	7600 kg/m ³
E_{PZT}	elastic modulus, piezo., unpolarized direction	79.4 GPa
$E_{\text{p, PZT}}$	elastic modulus, piezo., polarized direction	54.7 GPa
d_{13}		-9.7×10^{-11} m/V
d_{33}	coupling matrix entries, piezo.	2.25×10^{-10} m/V
d_{42}		3.3×10^{-10} m/V
$\varepsilon_{\text{T},11}$	permittivity matrix entries, piezo.	735
$\varepsilon_{\text{T},33}$		510

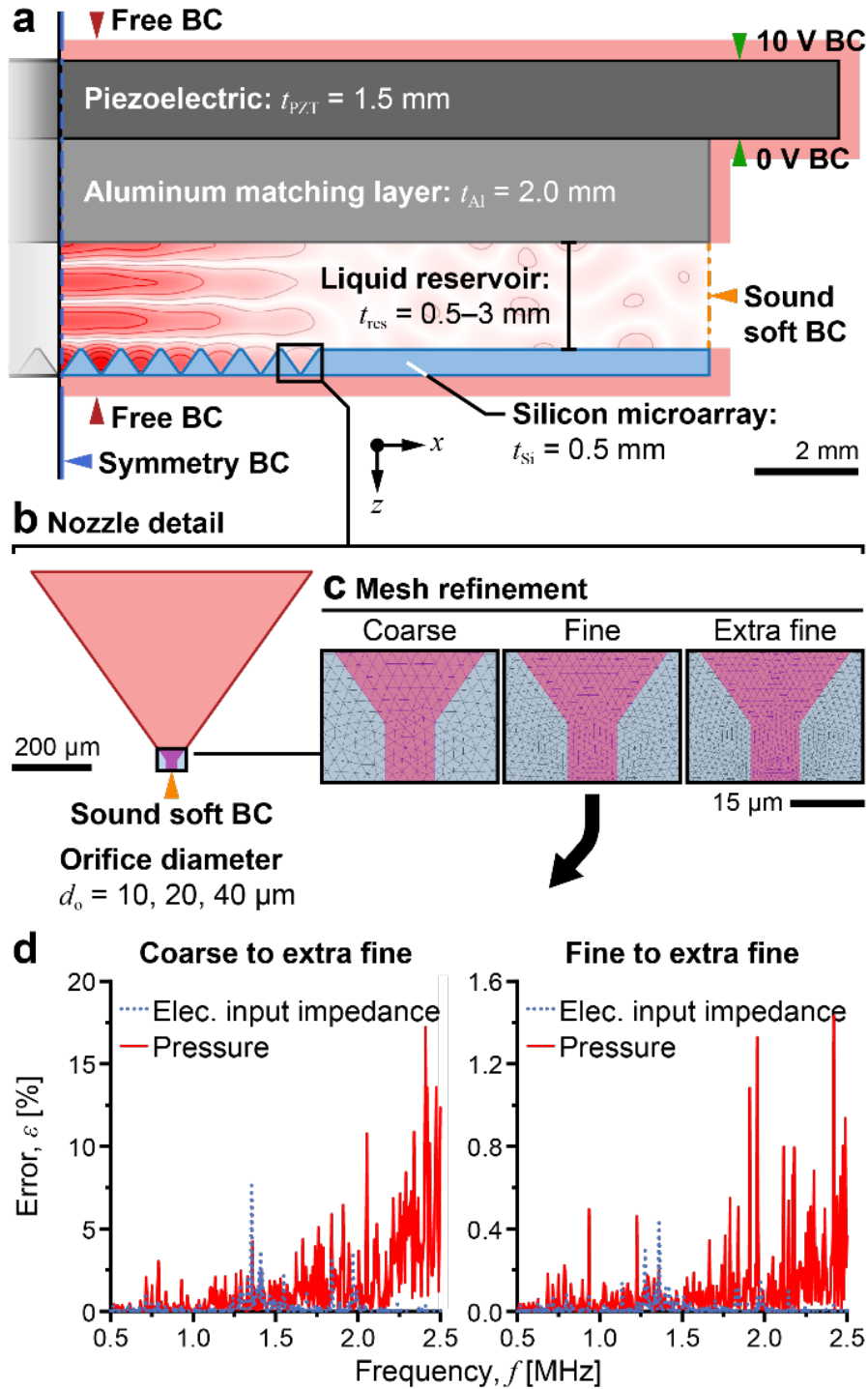


Figure 3.8 Computational modeling approach: (a) finite element analysis (FEA) domain including component geometry and applied boundary conditions (BC), (b) detail of the nozzle geometry and tip BC, (c) representative meshes used for mesh refinement and solution convergence, and (d) comparison of the electrical input impedance and pressure errors for coarse and fine meshes.

When a voltage was applied to the top and bottom of the piezoelectric transducer, the charge displacement within the transducer deformed the structure. Elastic vibrations propagated through the solid materials, inducing an acoustic wave in the liquid reservoir. A frequency-domain analysis provided the desired steady-state time-harmonic pressure field in the liquid domain. A strain-charge form of the piezoelectric constitutive equations was used to describe the relationships among the mechanical stress \mathbf{T} , the strain \mathbf{S} , the current displacement \mathbf{D} , and the applied electric field \mathbf{E} in the transducer:

$$\mathbf{S} = s_E \cdot \mathbf{T} + d^T \cdot \mathbf{E} \quad (3.3)$$

$$\mathbf{D} = d \cdot \mathbf{T} + \varepsilon_T \cdot \mathbf{E}, \quad (3.4)$$

where s_E is the piezoelectric compliance matrix measured under a constant electric field, d is the piezoelectric coupling matrix, and ε_T is the electric permittivity under uniform stress. A linear elastic material model was used for the aluminum and silicon such that the relationship between the stress and strain was described by Hooke's law:

$$\mathbf{S} = s \cdot \mathbf{T}, \quad (3.5)$$

where s is the compliance matrix defined by the Poisson's ratio ν and elastic modulus E of the material. In the liquid domain, the inviscid wave equation was solved to determine the acoustic pressure p :

$$\nabla^2 p - \left(\frac{\omega}{c}\right)^2 p = 0, \quad (3.6)$$

where ω is the circular frequency, and c is the speed of sound.

Figure 3.8 (a) and (b) also includes the boundary conditions used for the simulation. A symmetric boundary condition was applied at the midline of the assembly. Voltage amplitudes of 10 V and 0 V were applied to the top and bottom of the piezoelectric transducer, respectively. To

simplify the problem, perfect bonding was assumed at the piezoelectric-aluminum interface. Acoustic-structure boundary coupling was applied at the aluminum-liquid and liquid-silicon interfaces. A free boundary condition was implemented for all other edges of the solid domains, while a sound soft boundary condition ($p = 0$) was applied at the orifices and the liquid side wall representing the liquid-air interface of the open reservoir. Aluminum, silicon, and water were assigned COMSOL-provided material models at the assumed temperature of 23°C. Nominal APC 880 properties were supplied by the vendor, with slight adjustments made to the input material properties to improve the match between predicted behavior and experimental validation measurements (see below). Adjusted properties are listed in Table 3.4.

A mesh-independence study was conducted to investigate the influence of mesh density on the electrical input impedance and pressure field in the liquid domain. As shown in Figure 3.8 (c), free triangular meshes with three levels of mesh refinement (coarse, fine, and extra fine) were generated with different minimum element sizes (2.5 μm , 1.2 μm , and 0.8 μm , respectively) and element counts ($\sim 189,000$, $\sim 212,000$, and $\sim 248,000$, respectively). The input impedance and the average pressure along the pyramidal horn inlet were used to assess solution independence as a function of mesh density [Figure 3.8 (d)]. The approximate error was calculated using the normalized absolute difference between the solution quantity of the mesh being evaluated (S_j) and that of the reference mesh (S_{ref} , which is equivalent to the extra fine mesh):

$$\text{error} = \left| \frac{S_j - S_{\text{ref}}}{S_{\text{ref}}} \right|. \quad (3.7)$$

The electrical input impedance and pressure errors between the coarse mesh and extra fine mesh were significant, reaching a maximum of 7.6% and 17.2%, respectively [Fig. 3.8 (d)], but the errors between the fine mesh and extra fine mesh fell to less than 1.5% throughout the frequency range studied. Therefore, the fine mesh was used for all simulations.

The computational model was validated first by comparing the predicted electrical input impedance response of the unloaded PZT/Al actuator to that determined experimentally using a PC oscilloscope (PicoScope 2205A, Pico Technology) that measured the applied voltage waveform (i.e., an amplified sinusoidal signal corresponding to a 30 mV_{pp} signal input to the amplifier), the current waveform, and phase difference over the frequency range of interest (Figure 3.9). Model results were found to qualitatively match the overall trend of the experimental measurements; however, it was not possible to correlate minor resonances using the impedance response. Further model validation was performed using visual observation of robust spraying at predicted frequencies of operation (see Section 3.2.3 Results and discussion). With few exceptions, droplet ejection occurred at frequencies where the mode shape exhibited longitudinal (*z*-direction) stratification indicative of an ejection mode.

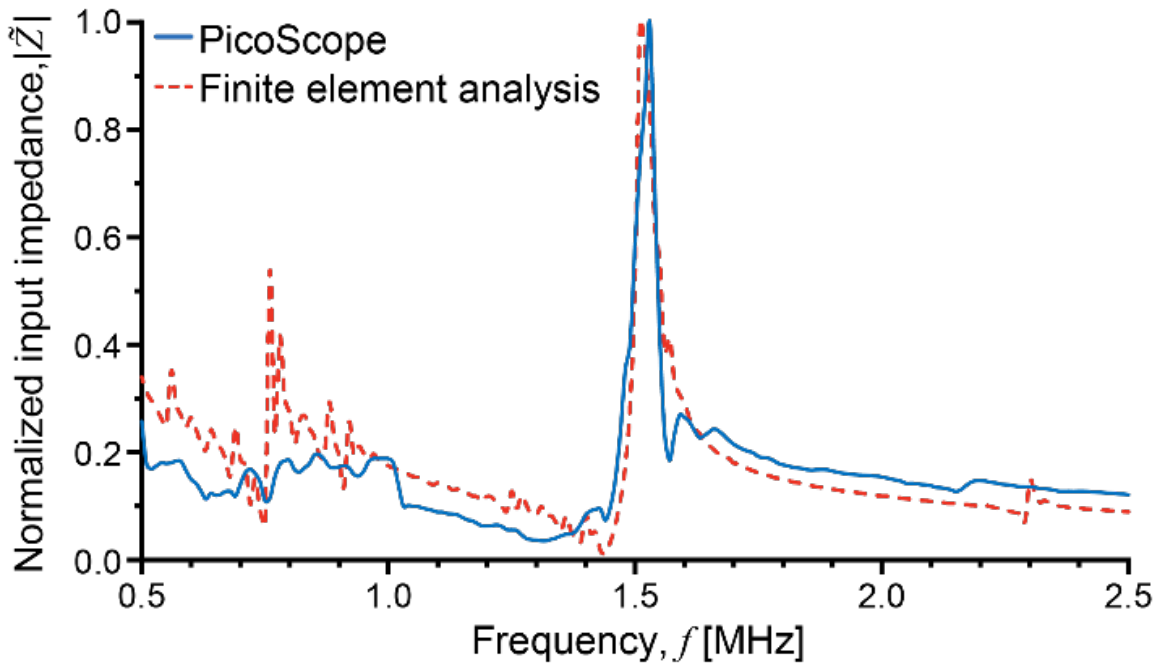


Figure 3.9 Comparison of model (finite element analysis) and experimentally measured (Picoscope) normalized electrical input impedances for the unloaded PZT/Al actuator over the frequency range 500 kHz to 2.5 MHz.

3.2.3 Results and discussion

A. Overview of the ejection modes

The morphologies of droplets ejected from a nozzle microarray with an orifice diameter of 5 μm , 10 μm and 15 μm were investigated. For each nozzle microarray sample, only the nozzle at the center (7th nozzle in the 7th row of a 13 \times 13 microarray) had the target orifice diameter and the orifice diameter for all other orifices was $\sim 1 \mu\text{m}$ (see Section 2.3 for details). First, simulations were performed to predict the liquid reservoir height for longitudinal resonances at the frequencies of 0.5 MHz, 1 MHz, 1.5 MHz, and 2 MHz. As shown in Figure 3.10, the predicted liquid reservoir heights for the first longitudinal resonance at 0.5 MHz and 1 MHz were found to be 1.56 mm and 0.56 mm, respectively. In addition, the predicted liquid reservoir heights for the second longitudinal resonance at 1.5 MHz and 2 MHz were found to be 0.47 mm and 0.29 mm, respectively.

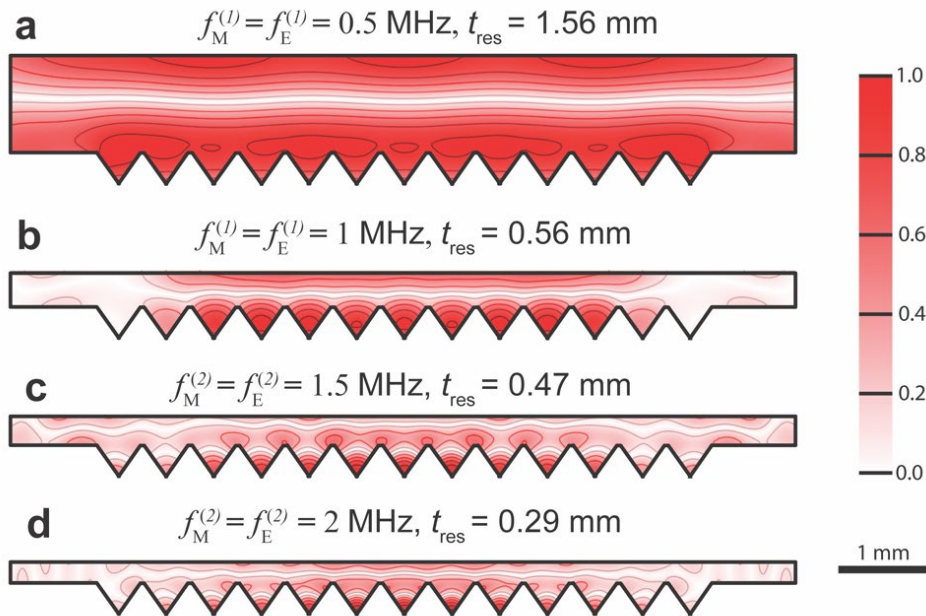


Figure 3.10 Normalized pressure contours in the liquid reservoir at the first resonance of (a) $f^{(1)} = 0.5 \text{ MHz}$, $t_{\text{res}} = 1.56 \text{ mm}$, (b) $f^{(1)} = 1 \text{ MHz}$, $t_{\text{res}} = 0.56 \text{ mm}$, and the second resonance of (c) $f^{(2)} = 1.5 \text{ MHz}$, $t_{\text{res}} = 0.47 \text{ mm}$, and (d) $f^{(2)} = 2 \text{ MHz}$, $t_{\text{res}} = 0.29 \text{ mm}$.

B. Overall ejection behavior

Experiments were then performed at the model-predicted conditions while increasing the drive voltage. The snapshots in Figure 3.11 show the following five moments: (a) a cluster of small droplets escaped from the orifice but with random sizes, velocities and paths, (b) jets or discrete droplets ejected from the orifice following a very straight path and the ejection was periodic (at the same frequency as the actuated signal), (c) screw-symmetric liquid path formed near the exit of the orifices, however, the ejection event was still periodic and followed the actuation signal, (d) extremely small droplets ejected from the nozzles with a conical plume, and (e) a large droplet blocked the orifice and grew in size as more liquid was pumped from the orifice, while the top part of the droplet was distorted by the high inertia of the newly pumped liquid.

When the input voltage at the piezoelectric assembly is low, the created pressure contour in the liquid reservoir is too small to result in a large enough inertia for ejection near the nozzle tips. Thus, the surface tension holds the liquid and hinders the bulk liquid ejection from nozzle orifices. However, the acoustic energy is still transferred to the liquid-gas interface at the orifice and leads to a periodically oscillating liquid surface. Some small droplets created by weak and random breakup at liquid surface are able to escape from the orifice in this mode of ejection, but these droplets created by random breakup have less inertia and uncertain trajectories. Thus, a chaotic ejection phenomenon results, as shown in Figure 3.11 (a). As the input voltage increases and exceeds a threshold, surface tension no longer holds the bulk liquid together due to the high inertia created by larger pressure gradient. At this moment, liquid is periodically pumped by the acoustic waves and ejects from the orifice. Because the device is operated at its longitudinal resonance, the direction of the pressure gradient in the liquid reservoir points to the orifice. Liquid in the reservoir moves toward the orifice with a high inertia and ejection follows the direction of the pressure gradient; thus, a straight jet is formed when exiting the orifice, as shown

in Figure 3.11 (b). When the input voltage continues to increase, the velocity of the ejected liquid increases and leads to a screw-symmetric shape, as shown in Figure 3.11 (c). This phenomenon has been widely observed and studied by other researchers, and it is caused by the asymmetric disturbances introduced by the aerodynamic forces due to the high relative velocity between the liquid and surrounding environment acting on the ejected jet⁸³⁻⁸⁶. As the input voltage further increases, the relative velocity between the ejected liquid and surrounding gases becomes larger. Higher aerodynamic forces act on the ejected liquid and break the liquid into extremely fine droplets forming a conical spray shape (or plume), as shown in Figure 3.11 (d). This type of ejection resembles what is called atomization. This is also a random breakup; thus, the generated droplets have diameters with a wide size distribution. At last, if the input voltage becomes high enough, the large pressure gradient near the orifice appears to directly pump liquid out and form a larger drop at the orifice exit. As shown in Figure 3.11 (e), the droplet blocks the orifice while it is distorted by the acoustic waves. For all regimes described above, only the straight jet/droplet or screw-symmetric jet/droplet have a periodic ejection event, which suggests that nozzle microarrays working in these two regimes are able to generate uniform and controllable droplets. As for all other regimes, random breakup introduced by the oscillating liquid surface or strong aerodynamic forces leads to unpreferable droplet size control. Thus, for these studies, we only investigated ejection behavior at straight jet/droplet or screw-symmetric jet/droplet regimes.

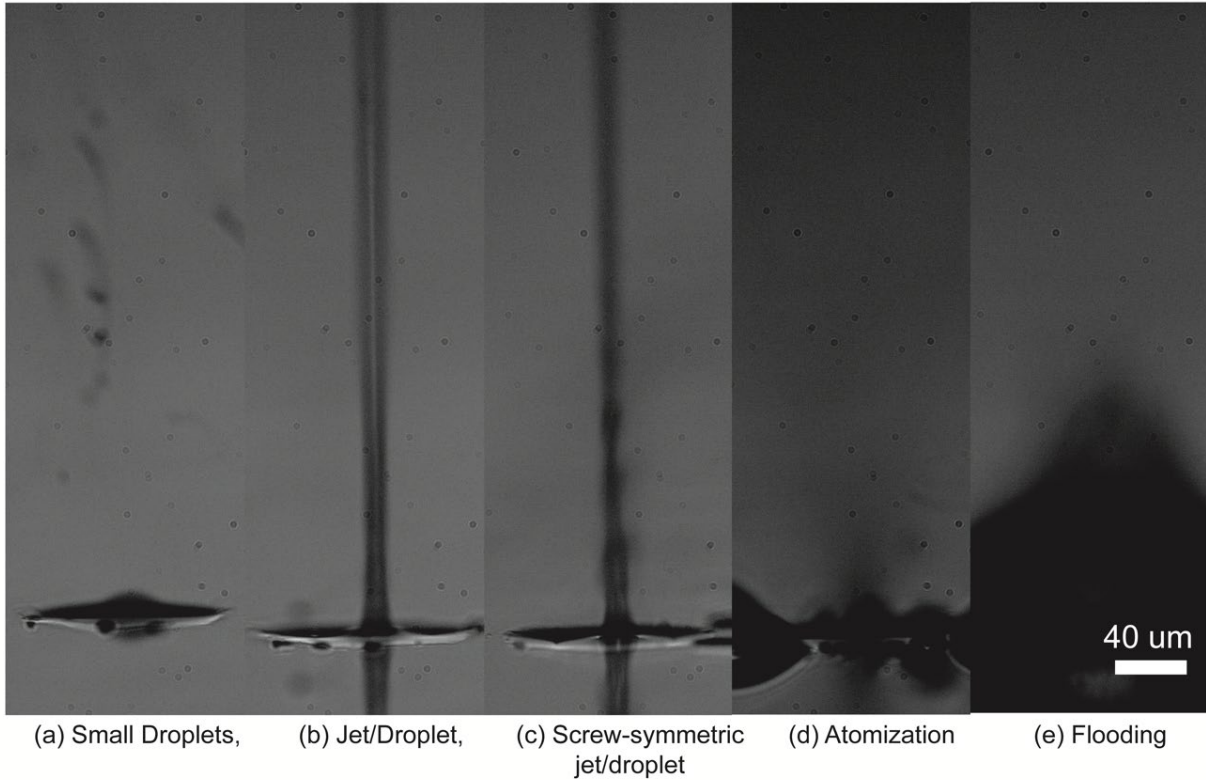


Figure 3.11 Five different liquid ejection moments observed in the experiments that were performed with an increasing input voltage and operated at the 2 MHz and 0.29 mm liquid reservoir height (2nd longitudinal resonance) with an orifice size of 15 μm : (a) small and random droplets escaped from orifice, (b) straight jet or discrete droplet periodically ejected from orifice, (c) the liquid that just exited the orifice shows a screw-symmetric shape, (d) liquid is atomized by acoustic energy to form a cluster of small droplets, and (e) a large drop blocks the orifice.

C. Liquid morphologies after ejection from orifices with different sizes

Figure 3.12 (a) shows the microscopic images of the liquid ejected from a 15 μm orifice with an increasing input voltage at a frequency of 0.5 MHz and a liquid reservoir height of 1.56 mm (1st longitudinal resonance). When the input voltage is very low (~ 30 mV), the ejected liquid jet is straight but with a wavy surface due to the periodic actuation single. The breakup of the liquid jet is not in the field of view. However, as the input voltage increases to ~ 40 mV [as shown in Figure 3.12 (b)(ii)], the first wind type breakup is observed, and the generated discrete droplets are close to each other due to the relatively low liquid velocity. As the input voltage, as well as

the ejected liquid velocity, continues to increase [as shown in Figure 3.12 (a) (ii)-(iv)], the jet length before the breakup occurs (or breakup length) decreases and the discrete droplets become further and further apart. The increased distance between droplets is attributed to the large inertia created by the larger pressure gradient and stronger oscillation of piezoelectric actuator. The phenomenon of a shrinking breakup length with an increasing liquid velocity has also been observed by other researchers. This phenomenon is a result of the larger aerodynamic forces acting on the ejected liquid. As the input voltage continuously increases to ~ 80 mV, a screw symmetric jet is observed, as shown in Figure 3.12 (a) (v), because the even larger aerodynamic forces bend the fluid jet shape against surface tension. When the ultrasonic droplet generator was operated at higher frequencies [1 MHz, 1.5 MHz, and 2 MHz, as shown in Figure 3.12 (b) – (d)], ejected liquid only shows a transition from straight jet to screw-symmetric shape as the input voltage increases, and the breakup of the liquid jet is not observed in the field of view.

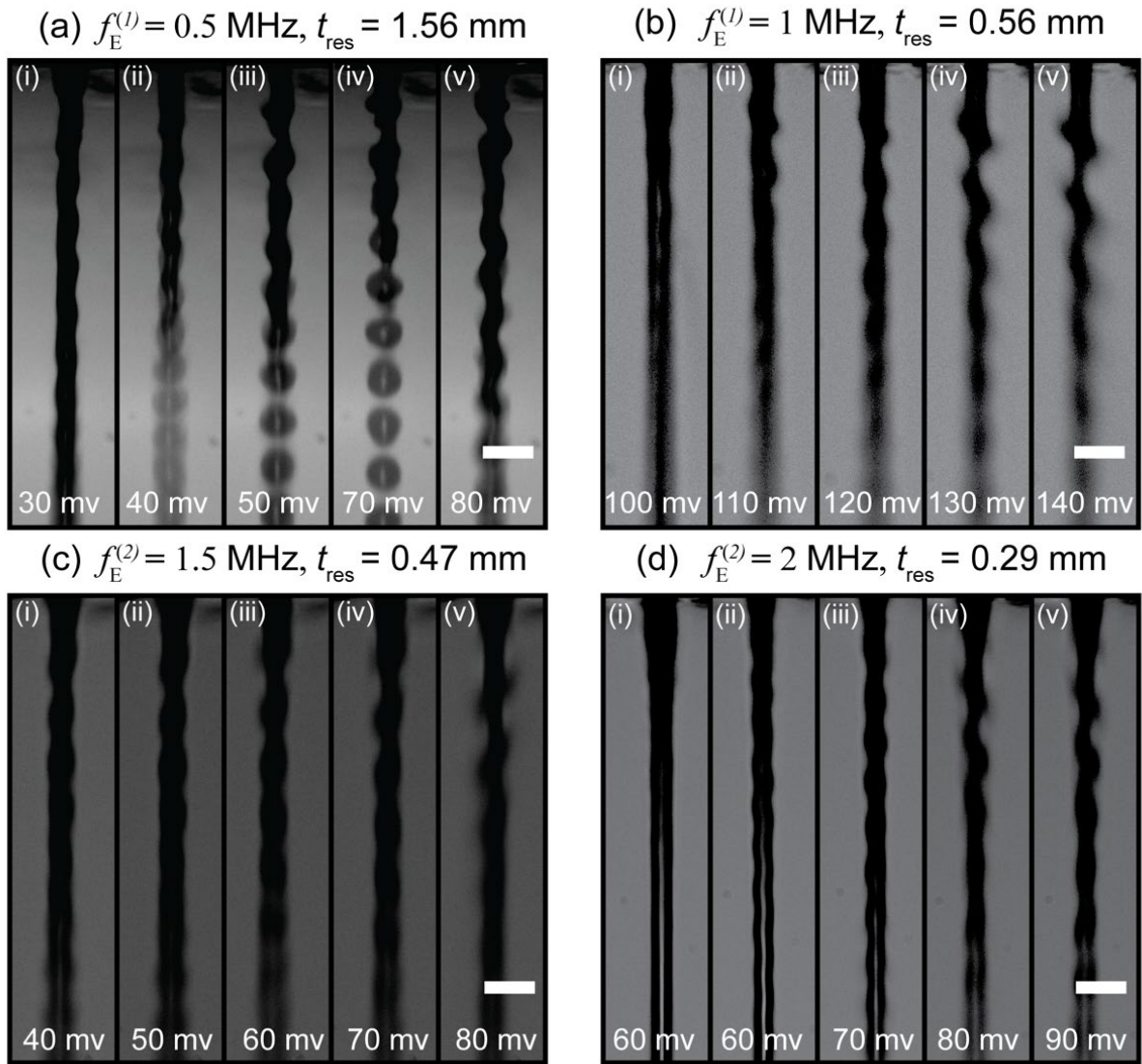


Figure 3.12 The microscopic images of the liquid ejected from a 15 μm orifice with an increasing input voltage at a frequency of (a) 0.5 MHz and a liquid reservoir height of 1.56 mm, (b) 1 MHz and a liquid reservoir height of 0.56 mm, (c) 1.5 MHz and a liquid reservoir height of 0.47 mm, and (d) 2 MHz and a liquid reservoir height of 0.29 mm.

As shown in Figure 3.13, similar behavior is observed when using a nozzle microarray with an orifice size of 10 μm operated at 0.5 MHz and 1 MHz. Long breakup lengths are observed when the liquid velocities are low (i.e., at low input voltages). The breakup length decreases as the liquid velocities increase. However, once the liquid jet enters the screw-symmetric regime, both profiles

of the liquid jet and droplets generated after the breakup become blurry due to very fast droplet velocities caused by the large input voltages. In addition, similar to the 15 μm orifice ejection behavior, when the 10 μm orifice operates at 1.5 MHz and larger, the breakup is not captured in the field of view, as shown in Figure 3.13 (c) and (d).

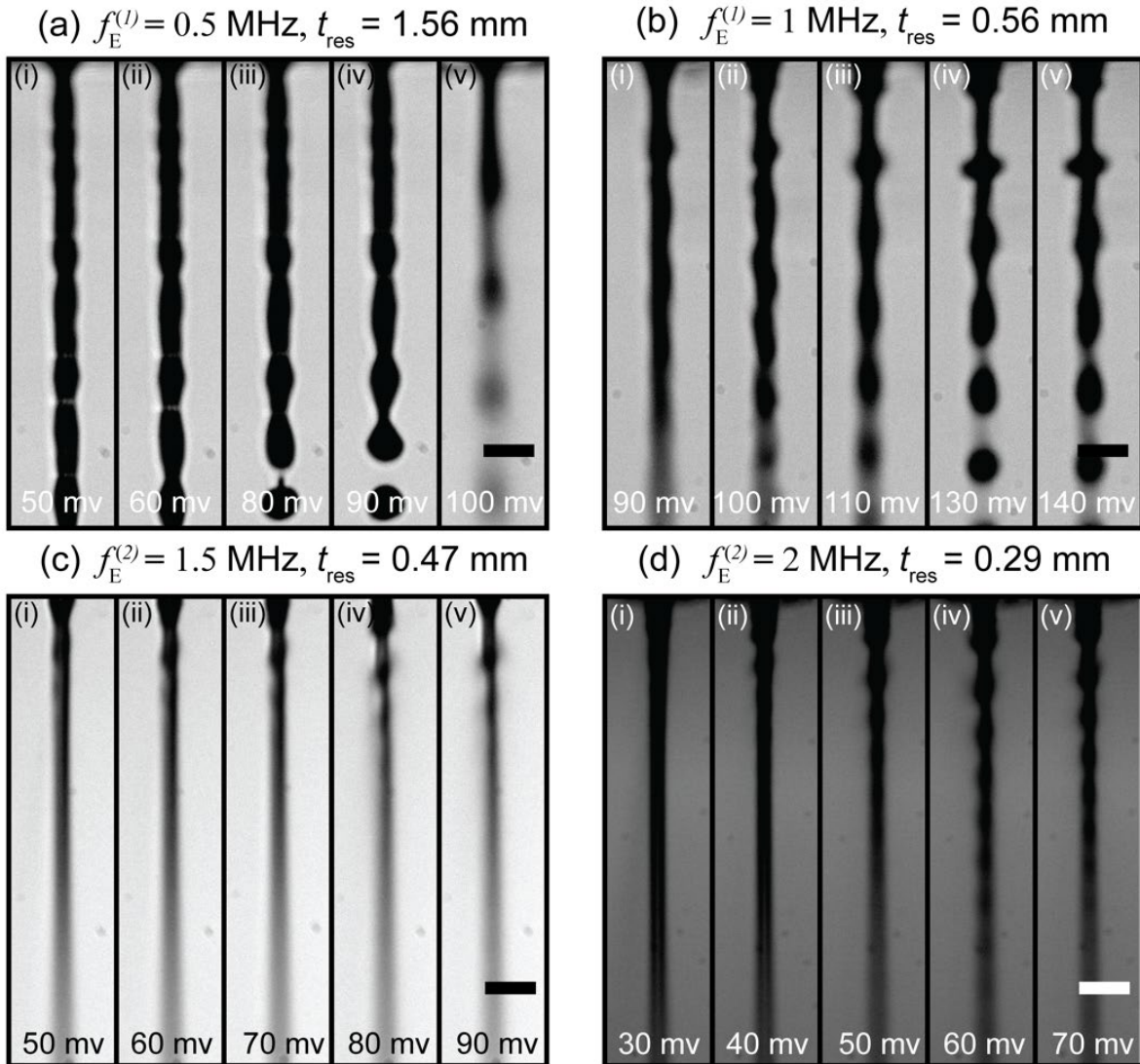


Figure 3.13 The microscopic images of the liquid ejected from a 10 μm orifice with an increasing input voltage at a frequency of (a) 0.5 MHz and a liquid reservoir height of 1.56 mm, (b) 1 MHz and a liquid reservoir height of 0.56 mm, (c) 1.5 MHz and a liquid reservoir height of 0.47 mm, and (d) 2 MHz and a liquid reservoir height of 0.29 mm.

As the orifice size is reduced to 5 μm , another ejection behavior is observed. When the nozzle microarray is operated at 0.5 MHz, discrete droplets immediately form as the liquid ejects from the orifice because the half-cycle of the negative pressure pulls liquid back into the reservoir and results in a tail connected to the main droplet formed at the half-cycle of positive pressure. For these conditions, surface tension has enough time to act and break the thin tail to form discrete droplets. As the liquid velocities increase with input voltage, longer tails are observed, as shown in Figure 3.14 (a). However, when the tail becomes long enough with large input voltage, the aerodynamic forces act on the liquid and the surface tension force further narrows the tail; eventually, the tail breaks up and forms satellite droplets in between the main droplets. The satellite droplets have a different velocity compared to the main droplets due to differences in liquid inertia over one ejection cycle, which is dominated by the oscillating pressure gradient in the liquid reservoir. Therefore, either rear merging [as shown in Figure 3.14 (a) (iii) and (iv)] or forward merging [as shown in Figure 3.14 (b) (iii) and (iv)] occur. In addition, larger satellite droplets become larger at higher liquid velocities, mainly due to the formation of a longer tail as described above. Both the satellite droplet size and the main droplet size were measured, as reported in Table 3.5. It is clear that even though the main droplet sizes decrease with increasing voltage, the total volume of the liquid ejected from each cycle appears to become larger. However, the total liquid volume per cycle decreases as the operating frequency increases because the period over which liquid ejects is reduced.

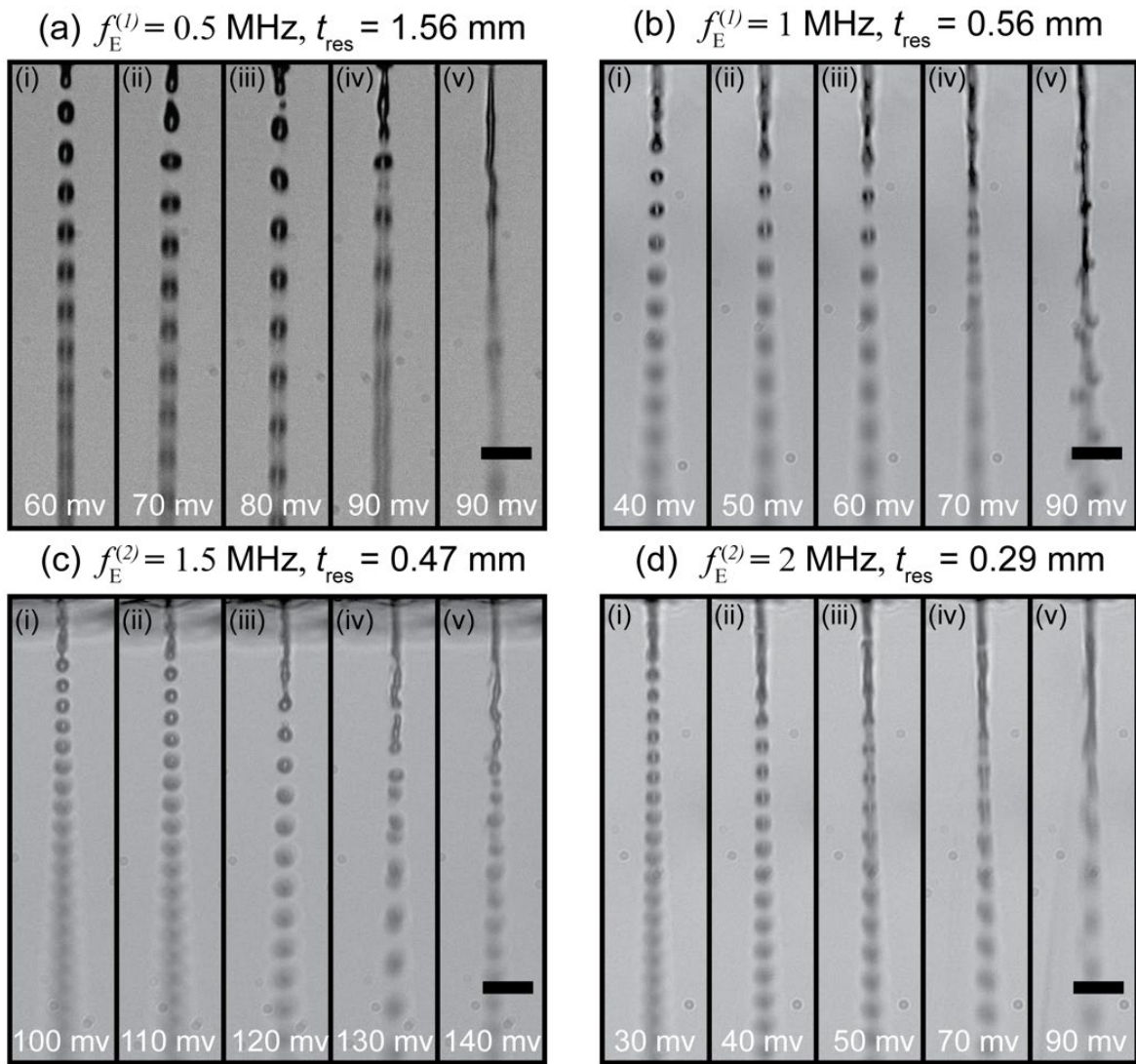


Figure 3.14 The microscopic images of the liquid ejected from a 5 μm orifice with an increasing input voltage at a frequency of (a) 0.5 MHz and a liquid reservoir height of 1.56 mm, (b) 1 MHz and a liquid reservoir height of 0.56 mm, (c) 1.5 MHz and a liquid reservoir height of 0.47 mm, and (d) 2 MHz and a liquid reservoir height of 0.29 mm.

Table 3.5 Summary of droplet sizes and the volume of liquid ejected from each cycle.

Orifice Dia (μm)	Frequency	Input voltage (mV)	Main Droplet Dia (μm)	Satellite droplet Dia (μm)	Main droplet volume (pL)	Satellite droplet volume (pL)	Total Volume (pL)
5	0.5 MHz	60	6.77	N/A	162.47	N/A	162.47
5	0.5 MHz	70	7.12	N/A	188.99	N/A	188.99
5	0.5 MHz	80	6.89	3.34	171.26	19.51	190.77
5	0.5 MHz	90	6.62	4.35	151.91	43.10	195.00
5	0.5 MHz	100	6.30	5.32	130.92	78.84	209.76
5	1 MHz	40	5.87	N/A	106.08	N/A	106.08
5	1 MHz	50	5.53	3.46	88.39	21.69	110.08
5	1 MHz	60	5.70	3.55	96.97	23.33	120.29
5	1 MHz	70	5.19	4.51	73.06	48.14	121.20
5	1.5 MHz	40	5.31	N/A	78.39	N/A	78.39
5	1.5 MHz	50	5.49	N/A	86.64	N/A	86.64
5	1.5 MHz	60	5.33	2.57	79.28	8.89	88.17
5	1.5 MHz	70	4.84	4.10	59.37	36.09	95.45
5	1.5 MHz	80	4.76	4.88	56.47	60.85	117.32
5	2 MHz	100	4.96	N/A	64.02	N/A	64.02
5	2 MHz	110	5.28	N/A	77.07	N/A	77.07
5	2 MHz	120	5.11	3.24	69.87	17.75	87.62
5	2 MHz	130	4.70	4.06	54.36	35.04	89.40
5	2 MHz	140	4.34	4.47	42.90	46.66	89.56

D. Physics of the ejection process

Figure 3.15 shows the physical interpretation of observed ejection processes. When the nozzle microarray has a large orifice, operated at high frequencies, or at low input voltages (i.e., low liquid velocities), the wavy shape with small intervals shows up as a wavy liquid jet, and the peaks formed at each ejection cycle are close to each other. Therefore, the ejected liquid jet is less affected by the aerodynamic forces and the natural breakup occurs a long distance away from the orifices, as shown in Figure 3.15 (a). However, when the input voltage increases or the operating frequency decreases, the interval between peaks will move farther apart which leads to a smaller neck connecting the liquid ejected each cycle. Due to the larger relative velocities between the ejected liquid and surrounding gases, larger aerodynamic forces act on the liquid

jet. As the neck become smaller and smaller, the surface tension force increases and eventually breaks the liquid jet. As the orifice sizes decrease, even the same form of the jet leads to a smaller neck compared to the larger orifices, as shown in Figure 3.15 (c). Therefore, earlier breakup (i.e., a smaller breakup length) is observed for liquid ejected from the 10 μm orifices at a given frequency. As the orifice size is further reduced (e.g., for 5 μm orifices), the breakup occurs at the orifice exit, as shown in Figure 3.15 (d) and (e). However, when liquid that is ejected from such a small orifice has a larger velocity, a longer tail forms when the pressure oscillates from positive to negative, and eventually a satellite droplet forms below the main droplet, as shown in Figure 3.15 (e). As the liquid velocities continue to increase, liquid ejected from two cycles will be connected by a thin liquid neck. The neck breaks up after several ejection cycles and forms a satellite droplet(s), as shown in Figure 3.15 (f). Eventually, all satellite droplets will merge into large droplets due to the velocity difference, but this process may be less controlled than the main droplet formation event.

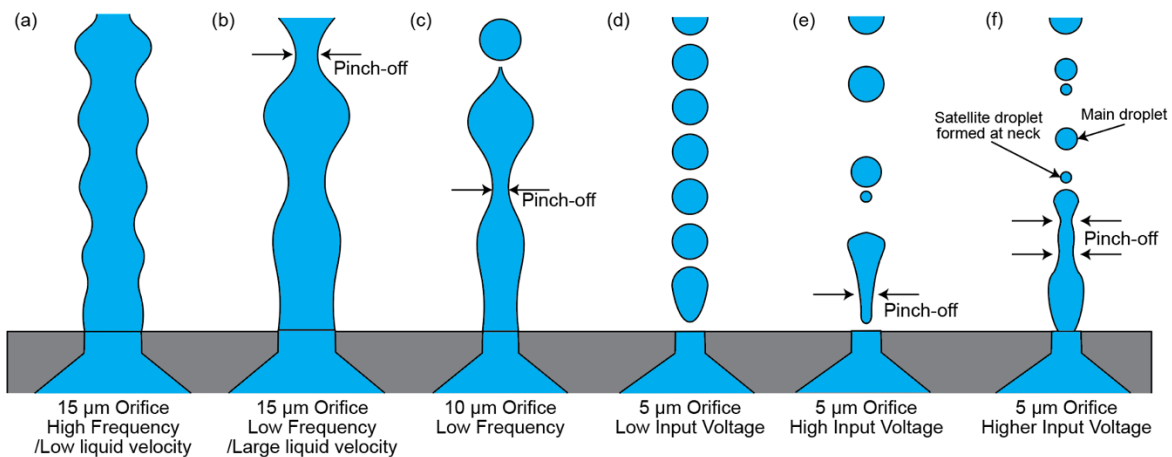


Figure 3.15 Physical interpretation of the ejection process. Three orifices with different operating conditions are illustrated.

A scaling analysis was performed to investigate the relative importance of operating frequency, inertia, surface tension, and viscosity on the ejection behavior. The time scales for these processes are:

$$t_f = \frac{1}{f} \quad (1)$$

$$t_U = \frac{r_o}{U} \quad (2)$$

$$t_\sigma = \sqrt{\frac{\rho r_o^3}{\sigma}} \quad (3)$$

$$t_\mu = \frac{\rho r_o^2}{\mu} \quad (4)$$

where t_f , t_U , t_σ , and t_μ are the process time scale, inertia time scale, capillary time scale, and viscosity time scale, respectively; f is the operation frequency, U is the ejected liquid velocity, r_o is the radius of orifice, σ is the fluid surface tension, ρ is the liquid density, and μ is the liquid dynamic viscosity.

These four times scales stand for the action time of certain physics, and a smaller value denotes a smaller time of action, thus having a more significant effect on the ejection behavior compared to other effects. Table 3.6 summarizes these four times scales for various ejection cases. For all cases, the viscous time scale, t_μ , is significantly higher than the other three time scales, which suggests that the relaxation of the liquid profile from viscous forces takes longer than the other three events. When the process time scale, t_f , is larger than the capillary time scale, t_σ , the surface tension acts fast enough to bring the liquid toward the spherical shape, which has the minimum energy within one cycle. This results in the formation of discrete droplets while liquid exits the orifice (DoD mode). If the process time scale is much smaller than the capillary time scale, the surface tension takes a longer time to act, and therefore, only a wavy profile forms on the ejected liquid jet, which will not breakup until the aerodynamic forces become significant.

This corresponds to the straight jet observed in the experiments, where the breakup phenomenon is not in the field of view (jet mode). In between these modes, there is another ejection mode observed when the capillary and process time scales are close to each other ($t_f \sim t_\sigma$), where the breakup of the liquid jet is observed and close to the orifice (transition mode). In addition, while the inertia time scale is about one order of magnitude smaller than the capillary or process time scales, the liquid inertia dominates the ejection process and the huge difference in velocities between the liquid jet and surrounding gases can bend the liquid jet, resulting in a screw-symmetric form for some cases.

Dimensionless numbers can also be used to characterize the ejection behavior. In our previous work, we demonstrated that the Strouhal number ($St = f/r_o U$) and Weber number ($We = \rho U^2 r_o / \sigma$) can be used to predict the transition between DoD and Jet mode. The transition was found to occur when the $We * St^2 (\rho f^2 / r_o \sigma)$ is between 0.4 to 2.5. In the current study, the Reynolds number ($Re = \rho U D / \mu$) is used to take the effect of velocity into account, and all five ejection regimes mentioned above are included in the regime plot shown in Figure 3.16.

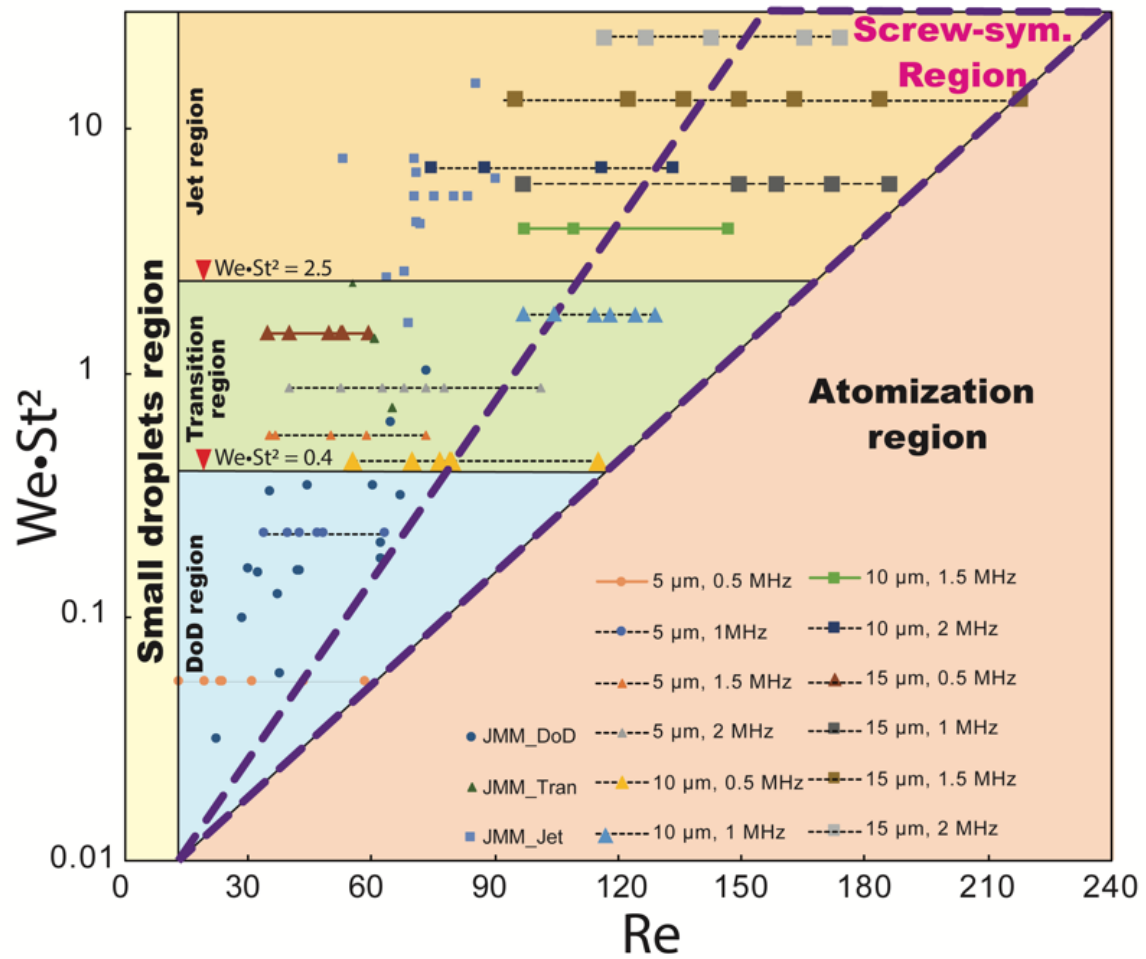


Figure 3.16 A regime map showing the five different ejection regimes including the small droplets region, droplet-on-demand region, transition region, jet region, and atomization region. The cases shown on the map also include our previous experimental data.

Table 3.6 Summary of the time scales for the process (t_f), inertia (t_U), surface tension (t_σ), and viscosity (t_μ) for some ejection cases.

Orifice Size (O_d , μm)	Frequency (f)	Ejection Mode	Velocity (U , m/s)	t_f (μs)	t_U (μs)	t_σ (μs)	t_μ (μs)
5	0.5 MHz	DoD	4.42	2.00	0.57	0.47	7.01
5	0.5 MHz	DoD	6.12	2.00	0.41	0.47	7.01
5	0.5 MHz	DoD	8.53	2.00	0.29	0.47	7.01
5	0.5 MHz	DoD	11.17	2.00	0.22	0.47	7.01
5	0.5 MHz	Screw	30.76	2.00	0.08	0.47	7.01
5	1.5 MHz	DoD	12.56	0.63	0.20	0.47	7.01
5	1.5 MHz	DoD	13.14	0.63	0.19	0.47	7.01
5	1.5 MHz	DoD	17.93	0.63	0.14	0.47	7.01
5	1.5 MHz	DoD	21.14	0.63	0.12	0.47	7.01
5	1.5 MHz	Screw	34.39	0.63	0.07	0.47	7.01
10	0.5 MHz	Jet	14.10	2.00	0.85	1.32	28.03
10	0.5 MHz	Tran	17.69	2.00	0.68	1.32	28.03
10	0.5 MHz	Tran	19.41	2.00	0.62	1.32	28.03
10	0.5 MHz	Tran	20.21	2.00	0.59	1.32	28.03
10	0.5 MHz	Screw	29.18	2.00	0.41	1.32	28.03
10	1 MHz	Jet	24.54	1.00	0.49	1.32	28.03
10	1 MHz	Tran	26.52	1.00	0.45	1.32	28.03
10	1 MHz	Tran	29.54	1.00	0.41	1.32	28.03
10	1 MHz	Tran	29.35	1.00	0.41	1.32	28.03
10	1 MHz	Screw	32.87	1.00	0.37	1.32	28.03
15	0.5 MHz	Jet	7.19	2.00	1.04	2.42	63.08
15	0.5 MHz	Tran	8.31	2.00	0.90	2.42	63.08
15	0.5 MHz	Tran	10.23	2.00	0.73	2.42	63.08
15	0.5 MHz	Tran	10.94	2.00	0.69	2.42	63.08
15	0.5 MHz	Screw	12.23	2.00	0.61	2.42	63.08

3.2.4 Conclusion

In this study, we investigated the microscopic behavior of the droplets ejected from ultrasonic droplet generators with a nozzle diameter of 5 μm to 15 μm . Five different ejection modes were identified, three of which can periodically generate discrete droplets. In addition, a physical interpretation of the ejection behaviors was concluded, and a time scale analysis was performed to summarize the ejection at different operation conditions. At last, a regime map was created to predict the ejection behavior at different operating conditions. The thorough study of the

microscopic ejection behavior of this work provides guidance on the design of ultrasonic droplet generators to produce more uniform droplets over an entire nozzle array.

Chapter 4: Implementations for sessile and free microdroplets

4.1 Introduction

4.1.1 Thin-film evaporation of pinned sessile droplets

Evaporation from droplets is a natural phenomenon driven primarily by the concentration gradient between the surface of the droplet and the ambient environment. Neglecting disjoining pressure^{87,88}, at the liquid-vapor interface the local liquid-vapor equilibrium yields a saturated vapor pressure. Therefore, vapor molecules spontaneously diffuse into the surrounding environment so long as the atmosphere is not saturated with the vapor. This diffusion-controlled evaporation model has been well developed since Maxwell first proposed that the evaporation rate is dominated by the diffusion rate of vapor into the ambient air⁸⁹. While new mechanisms of evaporation have been proposed, such as Marangoni flow⁹⁰⁻⁹², self-cooling^{93,94}, and gas kinetic theory⁹⁵, the diffusion model, with minor modifications⁹⁶⁻⁹⁸, has nevertheless been used successfully to give reasonable prediction of evaporation transport from suspended and sessile droplets. For example, for a droplet evaporating on a flat substrate, the downward diffusion of vapor is hampered⁹⁹⁻¹⁰². Therefore, an additional factor, usually described as a function of the contact angle, must be incorporated in the diffusion model to account for the diffusion confinement. Based on a modified diffusion model, for droplets with an apparent contact angle, θ_a , less than 90° , the local evaporation rate is maximized at the contact line and vice versa. For a droplet evaporating on a heated substrate, however, the evaporation transport behavior becomes more complex because the conduction resistance through the droplet creates a non-uniform temperature distribution and therefore a non-homogeneous concentration boundary at the droplet interface^{93,94}. In this case, for a droplet with diameter, D , larger than $100\ \mu\text{m}$, evaporation from

the bulk region of the droplet is dominated by the conduction resistance through the liquid. Consequently, at the contact line region, the evaporation rate can be an order of magnitude ($> 10 \times$) higher than that from the bulk region of the droplet.

Considerable experimental works have been performed on droplet evaporation; however, the most recent studies have focused on evaporation from axisymmetric droplets (i.e., droplets with spherical-capped geometry) which possess uniform geometric (e.g., uniform curvature, κ) features along the circumferential direction. The evaporative behavior of asymmetric droplets has started to attract greater interest only in recent years¹⁰³⁻¹⁰⁵. These droplets, compared to the capped spherical droplets, exhibit larger average curvatures, κ , and a larger ratio between the perimeter and interfacial solid-liquid area (A_{sl}). A large curvature induces a higher vapor concentration gradient in the vicinity of the liquid-vapor interface, while a larger perimeter-to-surface area ratio allows for a greater fraction of heat transport from the contact line region, both of which can lead to a higher evaporation rate. Saenz et al.¹⁰³ performed evaporation experiments on non-heated substrates and concluded that droplets with higher average curvature, κ_{avg} , will evaporate at a faster rate. Their work was further extended by Shuai et al.¹⁰⁵, who numerically analyzed the distribution of the local evaporation rate and local heat transfer coefficient of droplets pinned on square and triangular micropillars under adiabatic and heated conditions. Specifically, they found that microdroplets evaporating on a triangular substrate possess a 12.8% smaller effective film thickness than a droplet pinned on a circular substrate, due to a larger contact line perimeter. In addition, the effect of the droplet shape becomes less significant with increasing heat flux because the diffusion resistance becomes dominated by the liquid-vapor interfacial temperature, T_{lv} , instead of the meniscus curvature, κ . Beyond these findings, the heat transfer mechanism for asymmetric droplets evaporating on a heated substrate

has not been explored in detail. Thus, in this work, the heat transfer behavior of the microdroplets pinned on hollow micropillar structures with different cross-section shapes were investigated and will be further discussed in section 4.2.

4.1.2 The ejection behavior of the microdroplets ejected from an array of micronozzles

The breakup of a bulk liquid into small droplets creates a larger surface area to accelerate reactions with the surrounding environment and/or enhance heat and mass transfer. Traditional spray systems exploit a high relative velocity between the working liquid and surrounding gases to disrupt the liquid-gas interface. The resultant Plateau-Rayleigh instability causes the liquid to break up, creating a wide range of droplet sizes¹². The increasing demand for controllable, uniform droplets [e.g., for cell and biomaterial handling^{2, 13-15}, aerosol drug delivery¹⁶⁻¹⁹, materials synthesis^{6, 20}, and three-dimensional (3-D) printing^{21-25, 106}] has increased interest in discrete droplet [including so-called droplet-on-demand (DOD)] generators that offer exquisite control and precise droplet size. For example, aerosolized drug droplets with a diameters from 1–5 μm are required for effective delivery at different lung depths¹⁶, therefore achieving improved treatment outcomes. Controllable microdroplet generation also enables additive manufacturing of materials with higher resolution²¹.

Ultrasonic waves are commonly used for discrete droplet generation, transferring acoustic energy into a bulk liquid to break the liquid surface into extremely fine droplets⁷⁴⁻⁷⁶. In such devices, the amplitude and frequency of the ultrasonic waves are easily tuned to adjust the generated droplet size and velocity^{35, 74, 107}. Both surface acoustic waves (SAW) and bulk acoustic waves (BAW) have been investigated for microdroplet generation where liquid is placed directly on piezoelectric actuators, and acoustic waves (SAW or BAW) disrupt the free surface of the liquid^{74, 75, 108}. Random breakup phenomena can result in a wide droplet size distribution;

however, various approaches are implemented to improve uniformity. Tsai et al.^{109, 110} utilized a piezoelectrically-actuated multiple-Fourier horn structure to realize liquid atomization for drug delivery with a narrow droplet size distribution (3.5–4.4 μm) at low input power. Ultrasonic excitation also enables generation of a single droplet with a predefined diameter using either SAW or BAW by adjusting the device geometry and/or operating parameters. Connacher et al.¹⁰⁷ demonstrated droplet ejection using focused SAW with dissimilar parameters driven in opposite directions and converging at a sessile droplet. The commercial Echo[®] technology based on BAW has been widely applied to chemical and biomaterial liquid dispensing¹³⁻¹⁵. Although single droplet ejection using SAW or BAW achieves excellent precision, mass flow rate is inadequate for inhalation therapy or materials synthesis applications due to the limitations of a single ejection source.

To obtain uniform droplet sizes at larger mass flow rates, researchers assemble multilayered devices with a bulk liquid held between a piezoelectric actuator and an orifice plate containing an array of nozzles. The orifice size roughly dictates the ejected droplet diameter, and drive frequency provides finer control over droplet size and the mass flow rate. With many nozzles ejecting at the same time, larger mass flow rates are possible. Percin et al.¹¹¹⁻¹¹³ investigated droplet generation from an array of flextensional plates with a single orifice per plate. A circular actuation element was microfabricated around each nozzle exit to generate the energy required for liquid ejection. Demirci et al.¹¹⁴ simplified this configuration by fabricating straight nozzles in a silicon substrate as the nozzle plate for material printing applications. Orifice plates have been created with a variety of nozzle profiles including straight channels, conical tapers, and horn structures. For example, Jeng et al.¹¹⁵ designed and characterized the behavior of an atomizer consisting of a piezoelectric bimorph and a trumpet-shaped nozzle array with an

operating frequency of up to 25 kHz. Pan et al.⁸⁰ also fabricated a horn-shaped nozzle plate using microinjection molding. Nozzle plates were actuated by a piezoelectric transducer at frequencies from 2 kHz to 60 kHz, and droplets as small as 6.1 μm were produced. Such small droplets have a relatively larger specific surface area for chemical reactions or heat and mass transport.

Although various nozzle geometries have been realized, the pyramidal structure has been widely adopted due to ease of fabrication in silicon using anisotropic wet etchants. Diepold et al.¹¹⁶ reported one of the first uses of the pyramidal nozzle shape in a continuous inkjet printhead operating at a frequency of ~ 800 kHz. A similar single-nozzle system was used by Palm et al.¹¹⁷ to improve the flight stability of a train of droplets produced from $10 \mu\text{m} \times 10 \mu\text{m}$ square orifices excited at ~ 1 MHz. In these applications, acoustic excitation was used to achieve consistency by controlling breakup of a continuous jet at frequencies above the theoretical natural droplet formation frequency.

Ultrasonic standing waves can also be used to directly drive the ejection process, influencing the mode of ejection (continuous jetting or discrete droplets) and generated droplet size by adjusting the actuation frequency.^{8, 118} We have previously reported use of a micromachined ultrasonic droplet generator comprising a bulk piezoelectric actuator and pyramidal nozzle microarray that can operate at any (fixed) frequency from ~ 500 kHz to >2.5 MHz^{8, 34, 35, 76}. The liquid horn structure, sample reservoir height, and speed of sound of the ejection fluid dictate system resonances that create a favorable pressure gradient at the nozzle tips. Resonance matching of the actuator and reservoir geometry achieves efficient transfer of vibrational to acoustic energy⁸².

Uniform distributions of ~ 3 – $50 \mu\text{m}$ droplets have been generated from arrays with orifices spanning roughly the same size range^{4, 8, 35}. The device has been demonstrated with a variety of working liquids from low surface tension fuels to viscous polymers^{8, 76, 81}.

4.2 Evaporation from microdroplets confined on heated micropillar structures with different cross-section shapes

4.2.1 Experimental apparatus

The sample fabrication was already discussed in chapter 2.

In order to evaluate and compare the evaporation heat transfer performance between microdroplets with different shapes under the same conditions, the evaporation experiments were performed under steady-state conditions during which the shapes of the droplets were maintained constant by feeding the working fluid to the droplet continuously. However, supplying the droplet with exactly the same amount of liquid as the amount of water that evaporates with time while maintaining a desired droplet shape can be very challenging for a traditional syringe pump system. In this case, the droplet shape must be recorded and analyzed instantaneously by a customized algorithm to provide feedback information to the syringe pump to determine the required flow rate. Considering that the Laplace pressure of the microdroplet is determined by its radius of curvature, which is a strong function of the droplet shape, supplying the working fluid with a constant pressure head can ensure the droplet to maintain a stable geometry regardless of the evaporation rate when the viscous pressure is sufficiently small compared to the Laplace pressure. Such a condition is satisfied in this study for evaporation of a microdroplet with a diameter, $D = 100 \mu\text{m}$.

Therefore, a pressure-driven liquid feed system was installed in our experimental platform. As shown in Figure 4.1, the evaporation experimental setup consists of a working fluid routing system, shown in Figure 4.1 (e), and a sample mounting platform, which is shown in Figure 4.1 (d), and a data acquisition system (National Instrument, USB-6363, USA). The working liquid (DI water) is stored in a reservoir and pumped to the hollow micropillar by a nitrogen gas flow. The head

pressure of the working fluid is controlled by a pressure regulator (Elveflow, OB1 MK3, France) which connects to a compressed nitrogen tank (outlet pressure = 280 kPa) and enables gas outflow with a stable pressure ranging from 0 Pa – 2000 kPa. The flow rate and downstream flow pressure are monitored by a microfluidic flow sensor (Elveflow, MFS, range = 0 – 7 $\mu\text{L}/\text{min}$, resolution = 0.01 $\mu\text{L}/\text{min}$, France) and pressure sensor (Elveflow, MPS, range: 0 – 6894.76 Pa, resolution: 1 Pa, France). The mass flow rate measured by the flow sensor provides the instantaneous evaporation rate of the droplet. The porous micropillar sample assembly is mounted on an XYZ three-axis translation stage (Thorlabs, T12XYZ, USA). A DC power supply (Keithley Instruments, 2231A-30-3, USA) and a multimeter (Keithley Instruments, DMM7510, USA) are connected to the copper wires bonded to the RTD elements on the sample. The shape of the microdroplets during the evaporation process is captured by a CMOS DSLR camera (Canon, Rebel Ti6, Japan) using a 20 \times microscope objective lens (Olympus, #86-814, Japan) with a numerical aperture (NA) of 0.4.

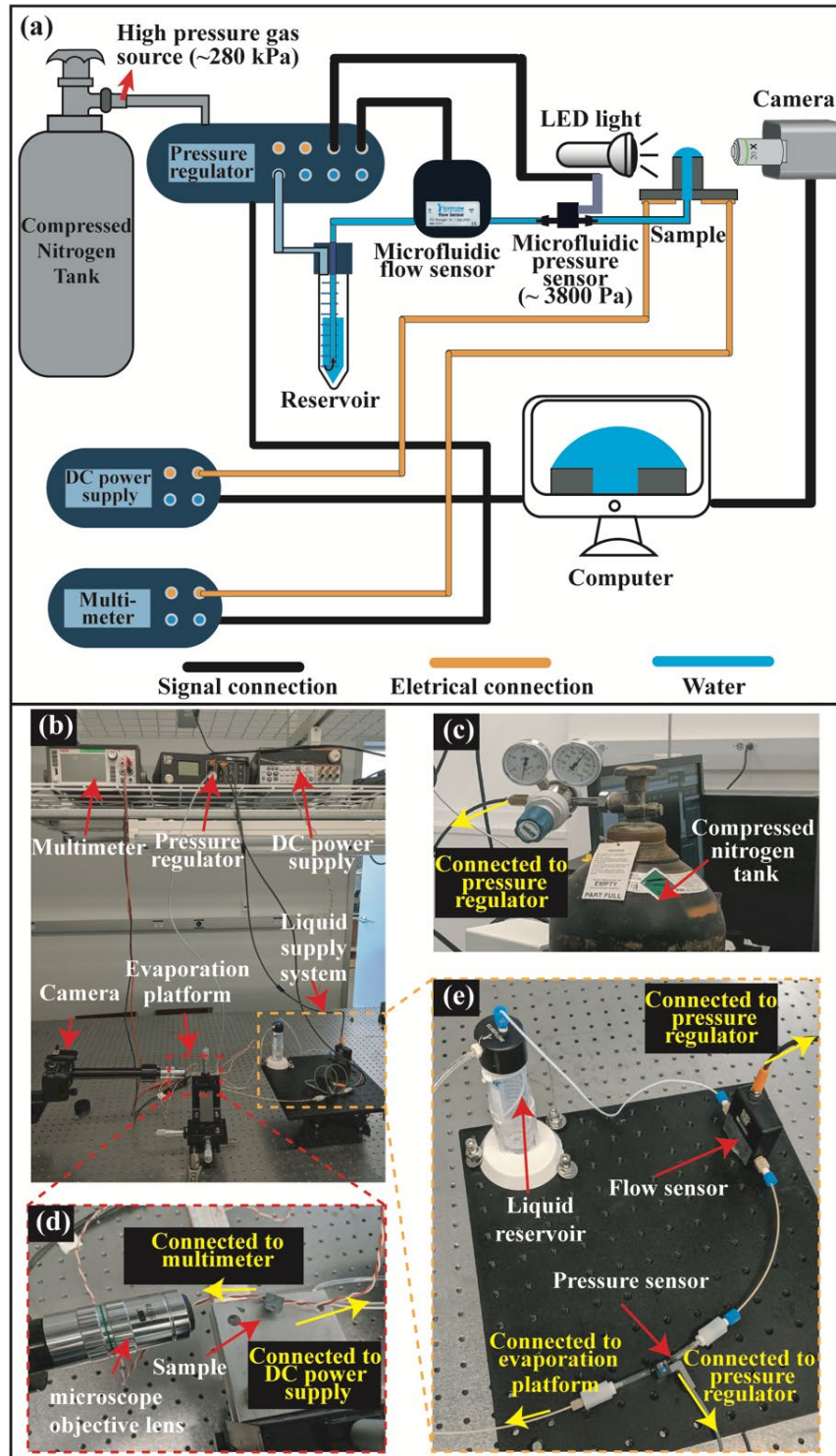


Figure 4.1 (a) Schematic drawing of the experimental setup. (b) – (e) Photographs of the experimental setup. (b) and (e) show the expanded views of the evaporation platform and the fluid routing system, respectively.

4.2.2 Liquid vapor interface of pinned sessile droplet

Before the evaporation experiment, deionized (DI) water was pumped to the porous micropillar structure to form a stable microdroplet with the desired geometry. In order to make a fair comparison between droplets evaporating on different micropillar samples, all the microdroplets were controlled to possess the same solid-liquid contact perimeter (314 μm) and liquid-vapor interfacial area (1200 μm^2). In order to determine the target droplet shape exhibiting these geometric features on a triangular and square micropillar structure, the open-source software Surface Evolver¹¹⁹, developed by Brakke, was used to find the equilibrium droplet morphology with different liquid volumes in the absence of any external force and dynamic effects. These two presumptions can be validated according to the capillary numbers (Ca) and the Bond (Bo) numbers associated with the evaporating droplet explored in this study. The capillary number is given by

$$Ca = \frac{\mu v}{\sigma} \quad (4.1)$$

where, μ , v and γ are the dynamic viscosity, velocity, and surface tension of the working fluid, respectively. The Bond number is given by

$$Bo = \frac{\Delta\rho g L_c^2}{\sigma} \quad (4.2)$$

where $\Delta\rho$ is the density difference between the liquid and air, g is the gravitational acceleration, and L_c is the characteristic length (i.e. the radius) of the droplet. For the maximum heat flux condition explored in this study, both Ca and Bo are found to be less than 10^{-4} as shown in Table 4.1. These results demonstrate that any dynamic and gravitational effects are negligible.

Table 4.1 The thermophysical properties, Capillary number, and Bond number of the water microdroplet explored in this study.

σ [N/m]	μ [kg/m·s]	ρ [kg/m ³]	v_{max} [m/s]*	Ca	Bo
0.072	8.9×10^{-4}	1000	2.58×10^{-3}	3.19×10^{-5}	3.40×10^{-4}

* The maximum flow velocity is determined based from the experimental measurements

To predict how the interfacial surface areas change as a function of droplet volume during the expansion on the asymmetric pillar structure, Surface Evolver, developed by Brakke¹¹⁹, was used to find the equilibrium droplet morphology with different liquid volumes. The algorithm embedded in Surface Evolver allows the surface to evolve towards a minimum energy state by the gradient descent method, during which each vertex is shifted in the desired direction within preset constraints. In this way, the final equilibrium shape can be obtained by iterating the successive energy minimization processes for many steps. In this study, we constrained the bottom surface of the microdroplets in a circular, a square, and a triangular shape with a perimeter of 314 μm . The desired droplet shapes were then obtained by increasing the volume of the microdroplets in Surface Evolver until the liquid-vapor interfacial area, A_h , of the equilibrated microdroplets reached 1200 μm^2 . Fig. 4.2 shows the evolution of the equilibrium morphologies of microdroplets on a triangular substrate generated in Surface Evolver before the final desired droplet geometries were obtained. In Surface Evolver, all geometric parameters are unitless. During the modeling in Surface Evolver, the interfacial solid-liquid area was set as 1 for all three cases. After the droplet reached its equilibrium shape, the liquid-vapor interfacial area was then measured by scaling up the geometric parameters to match the real solid-liquid contact area. Figure 4.3 shows the equilibrium droplet shapes obtained from Surface Evolver which were used as a reference for controlling the droplet geometries during the evaporation experiment.

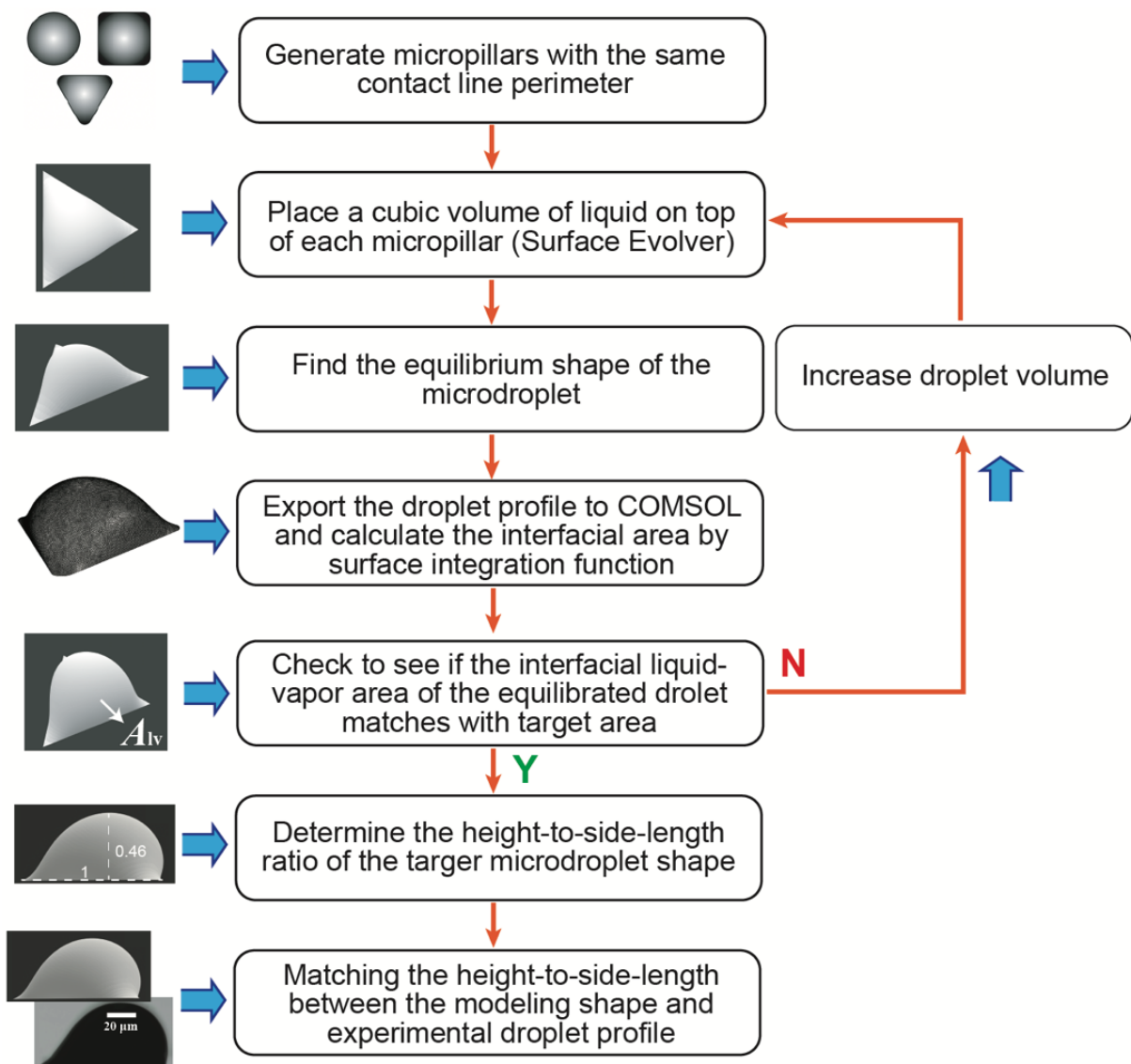


Figure 4.2 Flow chart for determining the desired microdroplet geometries with the same liquid-vapor interfacial area and solid-liquid perimeter for droplets on circular, square, and triangular micropillars.

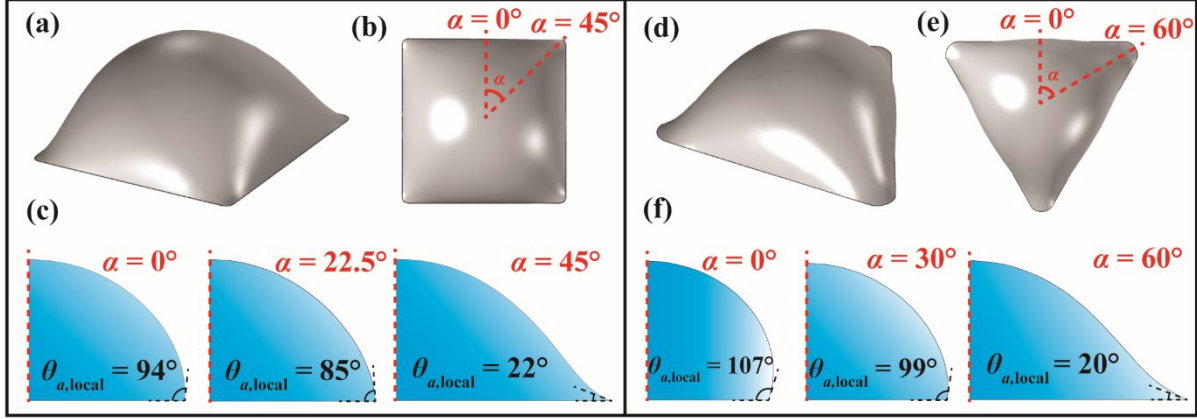


Figure 4.3 (a) – (c) shows an isometric view, top view, and cross section view of the equilibrium droplet profile on a square micropillar structure. (d) – (f) show an isometric view, top view, and cross section view of the equilibrium droplet profile on a triangular micropillar structure. The cross-section view shown in (c) and (f) are taken at three different azimuthal angles, α . The definition of the azimuthal angle is given in (b) and (e). The minimum and maximum local apparent contact angle, $\theta_{a,local}$, are found at the directions with the smallest and largest azimuthal angles, respectively.

As shown in Figure 4.3, the equilibrium droplet profile on a square and triangular micropillar is thicker near the center of the side edge (i.e., locations with a small azimuthal angle, α) and much thinner near the corner regions (i.e., locations with a large azimuthal angle, α). In other words, the local contact angle, θ_{local} , decreases monotonically with increasing α . This unique characteristic is attributed to a uniform Laplace pressure over the entire droplet under equilibrium conditions which is determined by the two principal radii of curvature at the droplet surface as

$$\Delta p = \sigma_{H_2O} \left(\frac{1}{R_1} + \frac{1}{R_2} \right), \quad (4.3)$$

where R_1 and R_2 are the two principal radii of curvature and σ_{H_2O} is the surface tension of water. If R_1 and R_2 are defined on the planes parallel and perpendicular to the top surface of the micropillar, respectively, as shown in Figure 4.4, then R_1 equals the local radius of the curved contact line at the corner region. At the center of the side edge however, the magnitude of R_1 goes to infinity,

since the edge is a straight line. Therefore, to ensure that $1/R_1 + 1/R_2$ are the same at these two different locations, the magnitude of R_2 at the corner region must be much larger than that at the center of the side edge. In other words, the meniscus is much thinner at the corner region, measured in the direction normal to the top surface of the micropillar. Thus, the local apparent contact angle is the smallest at the corner region.

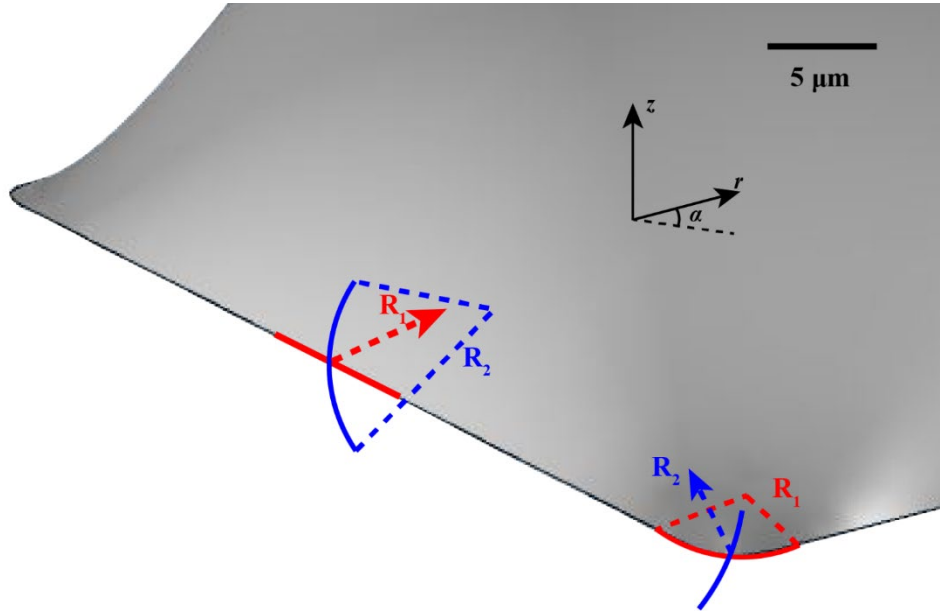


Figure 4.4 Schematic representation of the two principal radii of curvature at the center of the side edge and at the corner for a droplet on a square micropillar.

4.2.3 Experimental methods

To gain more insight into the evaporation transport of microdroplets on different micropillar structures and validate the experimental measurements, a Multiphysics simulation model was developed using COMSOL to predict the evaporation rate from axisymmetric and asymmetric microdroplets under different substrate temperature conditions. The pressure regulator and the compressed nitrogen tank were first turned on to pump the working fluid from the liquid reservoir to the porous micropillar sample. The pumping pressure of the working fluid was controlled by a program on a computer. During the pumping stage, DI water first flowed through

a mass flow sensor and then pinned atop the porous micropillar structure. When the liquid first emerges from the through hole, a convex meniscus is formed along the center pore of the micropillar, yielding a Laplace pressure of 2.72 kPa, 3.30 kPa, and 3.87 kPa for droplets on circular, square and triangular micropillars, respectively. The Laplace pressure formed at the inner pore is far greater than the viscous pressure loss across the tubing (3.34 Pa at 60 °C and 96.74 Pa at 98 °C). This pressure barrier prevents further growth of the microdroplet. With further increase in the pumping pressure, the liquid would quickly wet the pillar top surface and form a large microdroplet along the outer edge of the micropillar. The drastic increase in the droplet radius results in a sudden drop in the Laplace pressure. Therefore, the pumping pressure must be reduced quickly during the expansion of the droplet from the inner pore to the outer micropillar edge in order to prevent the bursting of the microdroplet. After this stage, the shape of the microdroplet can be controlled by the pressure regulator.

In order to match the droplet shape captured during the evaporation experiments with the desired droplet geometry obtained by Surface Evolver, the ratio between the maximum droplet height and the diameter (for a circular pillar) or the ratio between the maximum droplet height and the side length (for square and triangular pillars) is calculated from the droplet images taken during the experiment and compared with the target value calculated based on Surface Evolver results. If the value calculated from the experimental image is smaller than that obtained from the Surface Evolver result, then the head pressure of the working fluid controlled by the pressure regulator is increased slightly to allow a minor increase in the microdroplet height until the height-to-side-length ratio reaches the target value. Based on the equilibrium droplet geometries given by Surface Evolver, the maximum height-to-diameter ratio for the circular microdroplet is 0.35 and the maximum height-to-side-length ratios of the square and triangular microdroplets are

0.51 and 0.46, respectively.

After attaining the desired droplet geometries, the DC power source was turned on and the DC current supplied to the heater was increased slowly until the substrate temperature reached the target temperatures (60°C, 70°C, 80°C, 90°C, and 98°C). The reason for selecting 98°C instead of 100°C as the target substrate temperature is that any overshoot of temperature beyond 100°C would likely induce boiling of water. During the experiment, the substrate temperature was measured based on the electrical resistance reading of the RTD element collected by the multimeter. The evaporation rate of microdroplets was monitored by the mass flow sensor. A steady state was confirmed once the change in the time-averaged (calculated based on 30 sec time interval) pressure reading, temperature reading, and the flow rate reading became less than 1% over 30 minutes. These quantitative assessments were strengthened by visual observation of the microdroplet shape that demonstrated no variation of the droplet height greater than 5 μm for 30 mins. Afterwards, the mass flow rate and the RTD resistance were recorded for 30 secs for data reduction. The uncertainty for the heat transfer experiments includes the uncertainty for droplet morphology, Pt heater and RTD resistance, evaporation rate, and heat transfer coefficient. The uncertainty analysis is shown in Appendix 2.

4.2.4 Results and discussion

A. Evaporation rate from three different microdroplets

To gain more insight into the evaporation transport of microdroplets on different micropillar structures and validate the experimental measurements, a Multiphysics simulation model was developed by Dr. Binjian Ma and Junhui Li using COMSOL to predict the evaporation rate from axisymmetric and asymmetric microdroplets under different substrate temperature conditions.

See Appendix 3 for details. Both the simulation results and the experimental data are used for the explanation of the mass and heat transfer behavior of the pinned sessile droplets.

The evaporation experiments are performed in an ambient environment at a temperature of $22 \pm 1^\circ\text{C}$ and a relative humidity of $25 \pm 3\%$. Figures 4.5 – 4.7 (a) and (b) show snapshots of the microdroplet profile, the equilibrium droplet geometry given by Surface Evolver, and the evaporative flux of microdroplets on a circular, square and triangular micropillar under substrate temperatures ranging from $60^\circ\text{C} - 98^\circ\text{C}$. The evaporative flux is the evaporation rate per unit solid liquid interfacial area and is expressed as

$$J = \dot{m}/A_{sl} \quad (4.4)$$

where \dot{m} is the total evaporation rate from the droplet and A_{sl} is the solid-liquid contact area. A very close match in the droplet profile between the experimental and simulation results are found for all three shapes, where the difference in height-to-bottom-length ratio is less than 3%. The consistency confirms that the geometric parameters (i.e., solid-liquid contact perimeter and liquid-vapor interfacial area) of the evaporating droplets during the experiments closely follow the design values. With increasing temperature, the evaporation flux increases monotonically. When the substrate temperature is relatively low ($60^\circ\text{C} - 80^\circ\text{C}$), the evaporative flux increases at a smaller rate. As the substrate temperature gets higher ($>80^\circ\text{C}$), the evaporative flux increases at a much faster rate. This nonlinear increase in the rate is due to the nonlinear relationship between the equilibrium pressure and the liquid-vapor interfacial temperature. When T_{lv} is small, the saturated vapor concentration increases slowly. However, as T_{lv} increases, the saturated vapor concentration increases at a faster rate which facilitates a stronger concentration gradient in the vapor domain near the liquid-vapor interface. In addition, the vapor concentration in the far-field (ambient) is constant, and the vapor diffusion coefficient is not strongly

dependent on temperature. Therefore, the evaporation rate from the droplet surface increases with the vapor concentration gradient ($J_{evap} = D_{diff} \nabla C_v$). When the substrate temperature is approximately 60°C, the difference in evaporation rates among circular, square, and triangular microdroplets is only 6%. However, when the substrate temperature approaches 98°C, the total evaporation rate of a square microdroplet is 21% larger than that of a droplet on a circular micropillar. The total evaporation rate of a droplet on triangular micropillar is 23% larger than that of a droplet on a circular micropillar. The different enhancements of the evaporation rates for the three microdroplets at different temperatures result from the varied meniscus shapes of the microdroplets at the contact line region. Triangular and square microdroplets are deformed on micropillar tips due to the confinement at the micropillar outer edge. This deformation of menisci results in thinner liquid layers near the corner regions, as shown in Figs. 4.6(a) and 4.7(a), and leads to a larger effective thin-film region for triangular and square microdroplets¹⁰⁵. In addition, the large fraction of effective thin-film region results in a smaller conduction and vapor diffusion resistance for droplets confined on micropillars with asymmetric cross-sectional areas. As the substrate temperature increases, the conduction resistance for all three microdroplets nearly remains the same, but the vapor diffusion resistance decreases significantly. This decrease is more evident for microdroplets evaporating on square and triangular micropillars due to the asymmetric geometry of these droplets where a higher local evaporation rate is observed near the locations where the meniscus has high curvature. This phenomenon is attributed to a higher local vapor concentration gradient that drives faster vapor diffusion at more curved regions, similar to a lightning rod exhibiting a strong electric field along a highly curved surface¹⁰³.

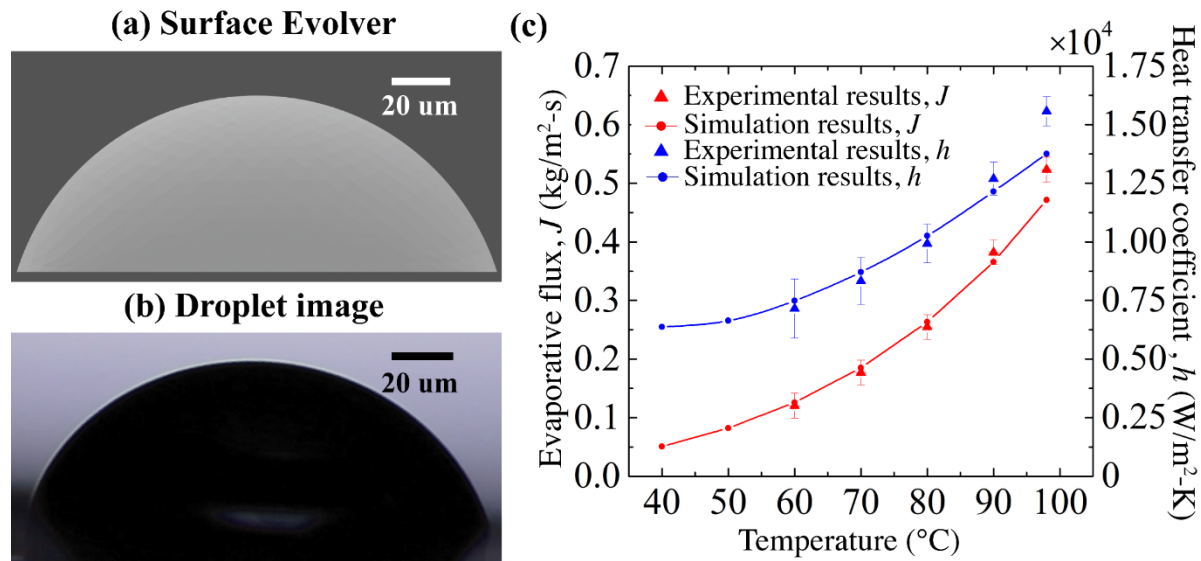


Figure 4.5 (a) Profile of microdroplet on a circular micropillar from Surface Evolver. (b) Image of a droplet confined on a circular micropillar captured from experiments. The apparent contact angle, θ_a , of this capped sphere microdroplet is 72° . (c) Evaporative flux and the heat transfer coefficient for circular microdroplets at substrate temperatures ranging from $40^\circ\text{C} - 98^\circ\text{C}$.

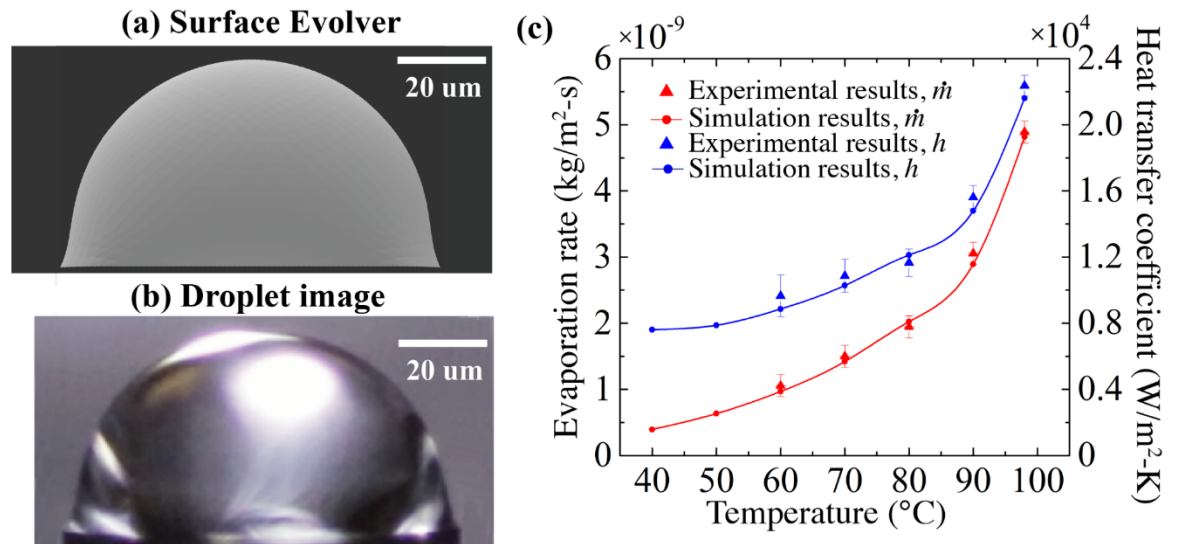


Figure 4.6 (a) Profile of microdroplet confined on a square micropillar from Surface Evolver. (b) Image of a microdroplet confined on a square micropillar captured from experiments. Both (a) and (b) are the microdroplet meniscus profile along the diagonal direction. (c) Evaporative flux and heat transfer coefficient for square microdroplets at substrate temperatures ranging from $40^\circ\text{C} - 98^\circ\text{C}$.

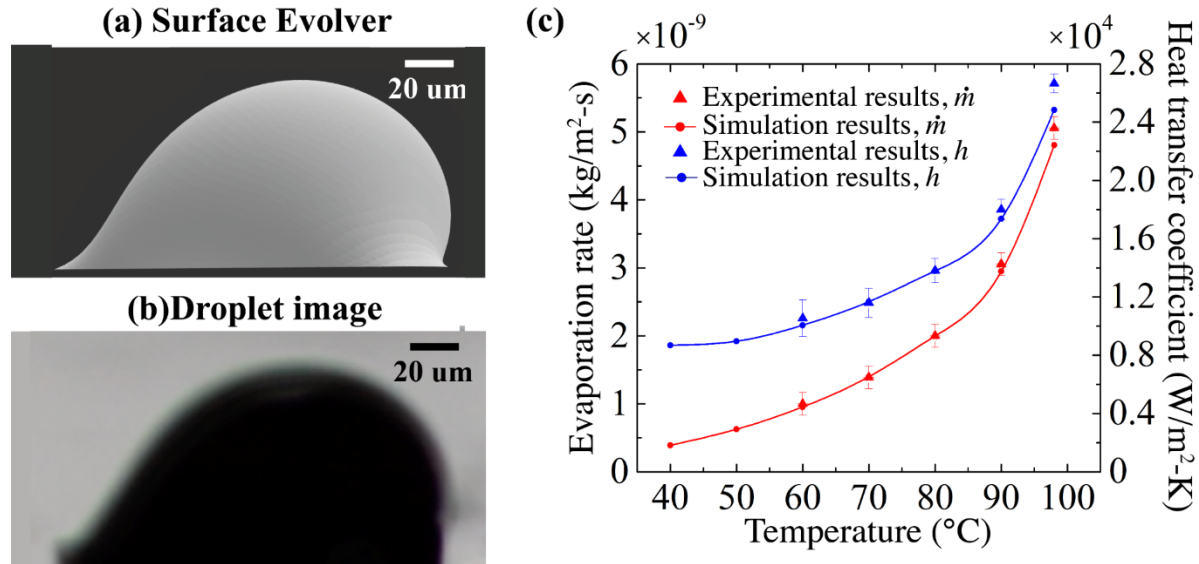


Figure 4.7 (a) Profile of microdroplet on a triangular micropillar from Surface Evolver. (b) Image of a microdroplet confined on a triangular micropillar captured from experiments. Both (a) and (b) are the cross-sectional profile taken along the centerline of the micropillar top surface. (c) Evaporative flux and heat transfer coefficient for microdroplets on triangular micropillars with temperatures from 40°C – 98°C.

Based on our measurements of evaporation rate and substrate temperature, the calculated heat transfer coefficients for the three evaporating droplets at five different temperatures are shown on the secondary y-axis in Figures 4.5 – 4.7. The variation in the heat transfer coefficient increases with temperature, which follows a similar trend to the evaporation rate. As discussed previously, the saturated vapor pressure increases at an exponential rate with increasing temperature. Therefore, the enhancement in the evaporation rate is much faster than the increase in temperature. The heat transfer coefficient, h , becomes increasingly larger at higher temperature. Specifically, as the substrate temperature is increased from 40°C – 98°C, the heat transfer coefficient increases by 117%, 131%, and 154% for microdroplets evaporating on a circular, square, and triangular micropillar, respectively.

The evaporative heat transfer performance of microdroplets evaporating on circular, square, and triangular micropillars is summarized in Table 4.2 and plotted in Figure 4.8. As shown in the

table, the heat transfer coefficients of microdroplets atop triangular micropillars are 8% and 45% larger than those of droplets on square micropillars at 60°C and 98°C, respectively, and 46% and 71% larger than those of droplets pinned on circular micropillars. This enhancement is attributed to the smaller solid-liquid area for triangular microdroplets. Since all three microdroplets evaporate from micropillars with the same contact line perimeter, the solid-liquid area for the microdroplet on the triangular micropillar is the smallest (4683.5 μm^2) among all cases, followed by the square micropillar (6162.3 μm^2), and the circular micropillar (7854.0 μm^2). In other words, a microdroplet evaporating on a triangular micropillar exhibits the longest contact line per solid-liquid area. Given that the evaporation heat transfer is most efficient at the contact line region, the overall heat transfer coefficient is highest for microdroplets evaporating on triangular micropillar structures.

Table 4.2 Experimentally measured evaporative flux and calculated heat transfer coefficients of the circular, square, and triangular microdroplets at different temperatures.

T_{sub} (°C)	J (kg/m ² s)			h (10 ⁴ W/m ² -K)		
	Circular	Square	Triangular	Circular	Square	Triangular
60	0.12	0.16	0.18	0.72	0.97	1.05
70	0.18	0.23	0.25	0.83	1.09	1.16
80	0.25	0.30	0.35	0.99	1.17	1.38
90	0.38	0.47	0.54	1.27	1.56	1.80
98	0.52	0.75	0.90	1.56	2.24	2.67

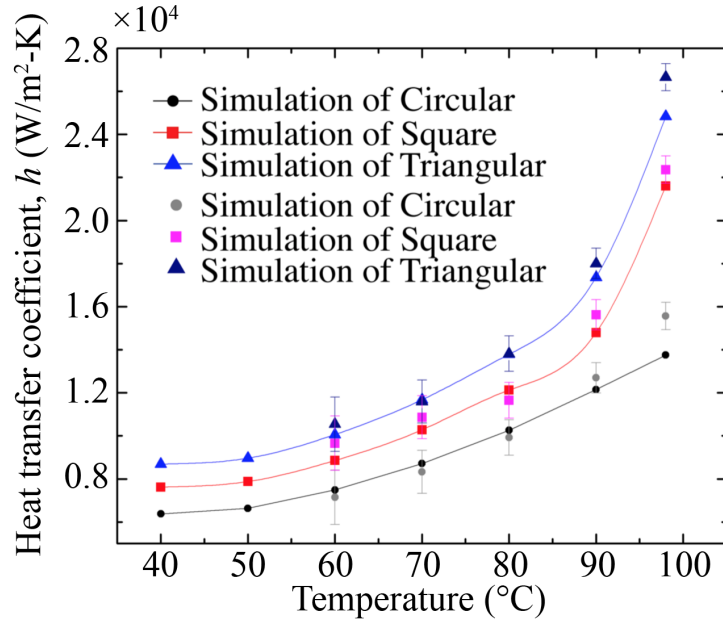


Figure 4.8 Heat transfer coefficients for three shapes of microdroplets from experiments and simulations. At all temperatures (from 40°C to 98°C), the heat transfer coefficient for triangular microdroplets is always the highest, 44.4% larger than that of a circular microdroplet at 60°C, and 71.2% larger than that of a circular microdroplet at 98°C. The difference is due to the slightly higher evaporation rate and the significantly smaller solid-liquid area (40% smaller than a circular micropillar top surface).

B. Characteristics of the local evaporation heat transfer and temperature distribution

Experiments provide only the relation between the microdroplet's total evaporation rate and its substrate temperature. To gain more insight into the evaporation heat transfer characteristics of three evaporating microdroplets at different temperatures, the local heat transfer performance and temperature distribution within the microdroplets, as well as the concentration distribution in the vapor domain are derived from the simulation results. In general, the numerical simulation yields a highly consistent results with the experimental findings: the differences between the experimental and numerical evaporative fluxes are only 4.7%, 8.4%, and 3.3 % for circular, square, and triangular microdroplets at 60°C, and 11%, 1.4%, and 7.4% at 98°C. The larger mismatch between the experimental and numerical results is possibly caused by a stronger thermocapillary flow generated under higher temperature conditions. While the Marangoni

number is found to be very small in this study, the magnitude of the Marangoni number is still increased by 3 times as the substrate temperature is raised from 60°C to 98°C. Therefore, the thermocapillary flow, which is neglected in the numerical model, may contribute slightly to the heat transfer inside the droplet under higher temperature conditions. Figure 4.9 (a) and (b) show three microdroplets' temperature distributions in the solid and liquid domains. For each microdroplet shape at the same temperature, the maximum temperature within three microdroplets is always observed at the liquid-solid contact line, where the local liquid film and the conduction resistance are minimized. Conversely, the minimum temperature for all three microdroplets is always observed at the center of the microdroplet, where the local liquid film and the conduction resistance are maximized. Moreover, at the same substrate temperature, the temperature at the center of a triangular microdroplet is smaller than that of a circular microdroplet, due to the larger height of triangular microdroplets. However, near the solid-liquid-vapor contact lines, a triangular microdroplet has a higher temperature result due to the thinner liquid-film. Figure 4.9 (c) and (d) show the vapor concentration distribution in the vapor domain for three shapes of microdroplets. When the substrate temperature is 98°C, the highest vapor concentration is observed near the solid-liquid-vapor contact line, which results from the higher liquid-vapor temperature. The higher vapor concentration near the contact region results in the higher evaporation rate near the contact region. When the substrate temperature is 40°C, the vapor concentrations along the liquid-vapor interface are close, due to the small temperature difference from the centers of microdroplets to the edges ($\sim 3^\circ\text{C}$).

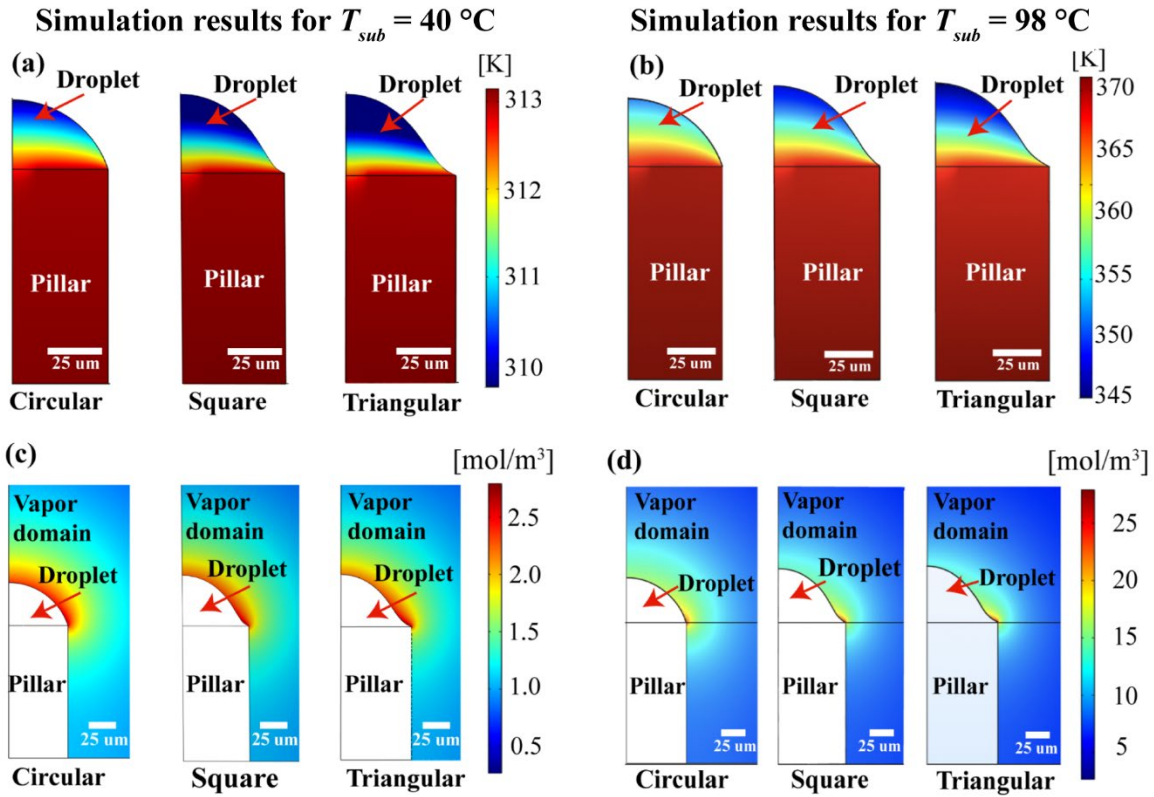


Figure 4.9 (a) and (b) are temperature contours for droplets on circular, square and triangular micropillars at substrate temperatures of 40 °C and 98 °C, respectively. (c) and (d) are the vapor concentration profiles near the liquid-vapor interface at substrate temperatures of 40 °C and 98 °C, respectively.

C. Thermal resistance analysis for evaporation of non-axisymmetric microdroplet

To better understand the dominating mode of heat transfer from asymmetric microdroplets during the evaporation process, the conduction and diffusion thermal resistances are analyzed based on the equilibrium geometries of these droplets. Specifically, the local distribution of these two resistances at different radial distances and different azimuthal angles are calculated and compared based on a COMSOL evaporation model. The evaporation resistance at the liquid-vapor interface, estimated based on gas kinetic theory, is approximately 10^{-10} Km²/W. Therefore, the evaporative resistance is much smaller than the conduction and diffusion resistances and therefore neglected in the analysis.

Heat is transferred from the top surface of the micropillar to the liquid-vapor interface through the path with the smallest conduction resistance across the droplet. The conduction resistance associated with each location on the droplet surface can be obtained based on the local liquid thickness inside the droplet by

$$R_{cond} = \frac{t}{k} \quad (4.5)$$

Figure 4.10 shows the distribution of the local conduction resistance along the radial direction taken at different azimuthal angles along with the corresponding cross-section profiles of the droplet on the square and triangular micropillars. The radial distance is normalized with respect to the maximum radial distance measured from the center of the droplet to the contact line region. It should be noted that for droplet cross-section profiles taken with an azimuthal angle $\alpha > 15^\circ$, the local contact angle of the droplet exceeds 90° and therefore the conduction resistance is not calculated all the way up to the contact line region. The results showed that the conduction resistance in both droplets decreases from a maximum value of around $7 \times 10^{-5} \text{ K}\cdot\text{m}^2/\text{W}$ at the center of the droplet to around $1 \times 10^{-6} \text{ K}\cdot\text{m}^2/\text{W}$ very close to the contact line region. This behavior is expected since the local thickness of the droplet decreases monotonically with increasing radial distance from the center of the droplet. In addition, at the same normalized radial distance, the conduction resistance is found to increase with increasing azimuthal angle which results in a less efficient heat transfer performance across the droplet. This characteristic is caused by the non-axisymmetric geometric feature of droplets pinned on micropillar structures with non-circular shapes. For droplets on triangular or square micropillars, the longer edge-to-center distance at directions with larger azimuthal angle causes the meniscus to spread out into a thinner film with a smaller local apparent contact angle, $\theta_{a,local}$, at these locations. On the contrary, the local liquid body is significantly thicker at locations with a smaller azimuthal angle,

since the spreading of the contact line is stopped by the outer edge of the micropillar with a shorter edge-to-center distance. Thus, the local conduction resistance is decreased by as large as 10 times at the same radial location when α is increased from $0^\circ - 45^\circ$ and $0^\circ - 60^\circ$ for droplets on square and triangular micropillars, respectively. This trend represents a distinctive feature from the evaporation behavior of capped spherical droplets. Comparing the results between the square and triangular case, it is found that the maximum local conduction thermal resistance in a triangular droplet is slightly smaller than that in the square droplet, since the triangular droplet exhibits a greater level of asymmetry and therefore a larger range of thickness distribution. Integrating the local thermal resistances in the cross-section plane at $\alpha = 0^\circ$ by assuming a parallel thermal resistance network shows that the average thermal resistance in this cross-section plane for the square and triangular droplet are approximately $1.14 \times 10^{-5} \text{ K} \cdot \text{m}^2/\text{W}$ and $1.18 \times 10^{-5} \text{ K} \cdot \text{m}^2/\text{W}$, respectively. The same calculation performed on the cross-section plane at $\alpha = 45^\circ$ for the square case and at $\alpha = 60^\circ$ for the triangular case yields an average thermal resistance of $5.90 \times 10^{-5} \text{ K} \cdot \text{m}^2/\text{W}$ and $5.25 \times 10^{-5} \text{ K} \cdot \text{m}^2/\text{W}$, respectively.

In the air domain, the heat is transported by diffusion of saturated vapor molecules into the surrounding ambient. The thermal diffusion resistance associated with each location on the droplet surface can be obtained by:

$$R_{diff} = \frac{(T_{lv} - T_\infty)}{\dot{m}_{local} \cdot h_{fg}} \quad (4.6)$$

where T_{lv} is the local temperature at the liquid-vapor interface and \dot{m}_{local} is the local evaporation rate which equals to the local diffusion rate. Both these two parameters can be extracted from the COMSOL evaporation model. Figure 4.11 shows the radial distribution of the local diffusion thermal resistance taken at different azimuthal angles under different substrate temperature

conditions. The thermal resistance associated with the diffusion mass transport is also found to decrease sharply from $\sim 3.0 \times 10^{-4} \text{ K} \cdot \text{m}^2/\text{W}$ at the center of the droplet to as small as $3.3 \times 10^{-5} \text{ K} \cdot \text{m}^2/\text{W}$ near the contact line of the droplet.

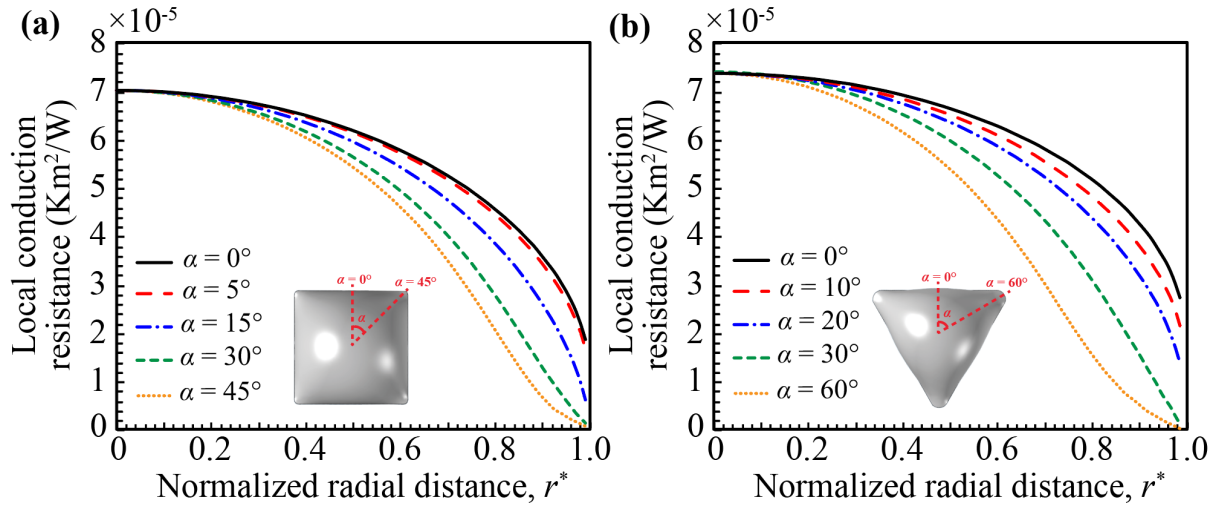


Figure 4.10 The distribution of the local conduction resistance along the radial direction taken at cross section planes with different azimuthal angles in an evaporating droplet on a (a) square and (b) triangular micropillar structure. With increasing normalized radial distance, the conduction resistance decreases sharply to zero due to the reduction in liquid thickness. At the same normalized radial distance, the conduction resistance decreases slightly with increasing azimuthal angle which represents an increase in the local liquid thickness when moving from the corner region to the center of the side edge of the asymmetric droplet.

The decrease in diffusion resistance is closely related to the decreasing conduction resistance near the contact line which results in a higher surface temperature and therefore a higher saturated vapor pressure at the liquid-vapor interface. The higher saturated vapor pressure gives rise to a larger vapor concentration and therefore, a larger diffusion mass transport rate. However, the change in the diffusion resistance along the radial direction becomes less significant with increasing α where the local liquid body becomes thinner. In addition, decreasing α also yields a higher diffusion resistance at the same radial distance which leads to a poorer heat transfer performance.

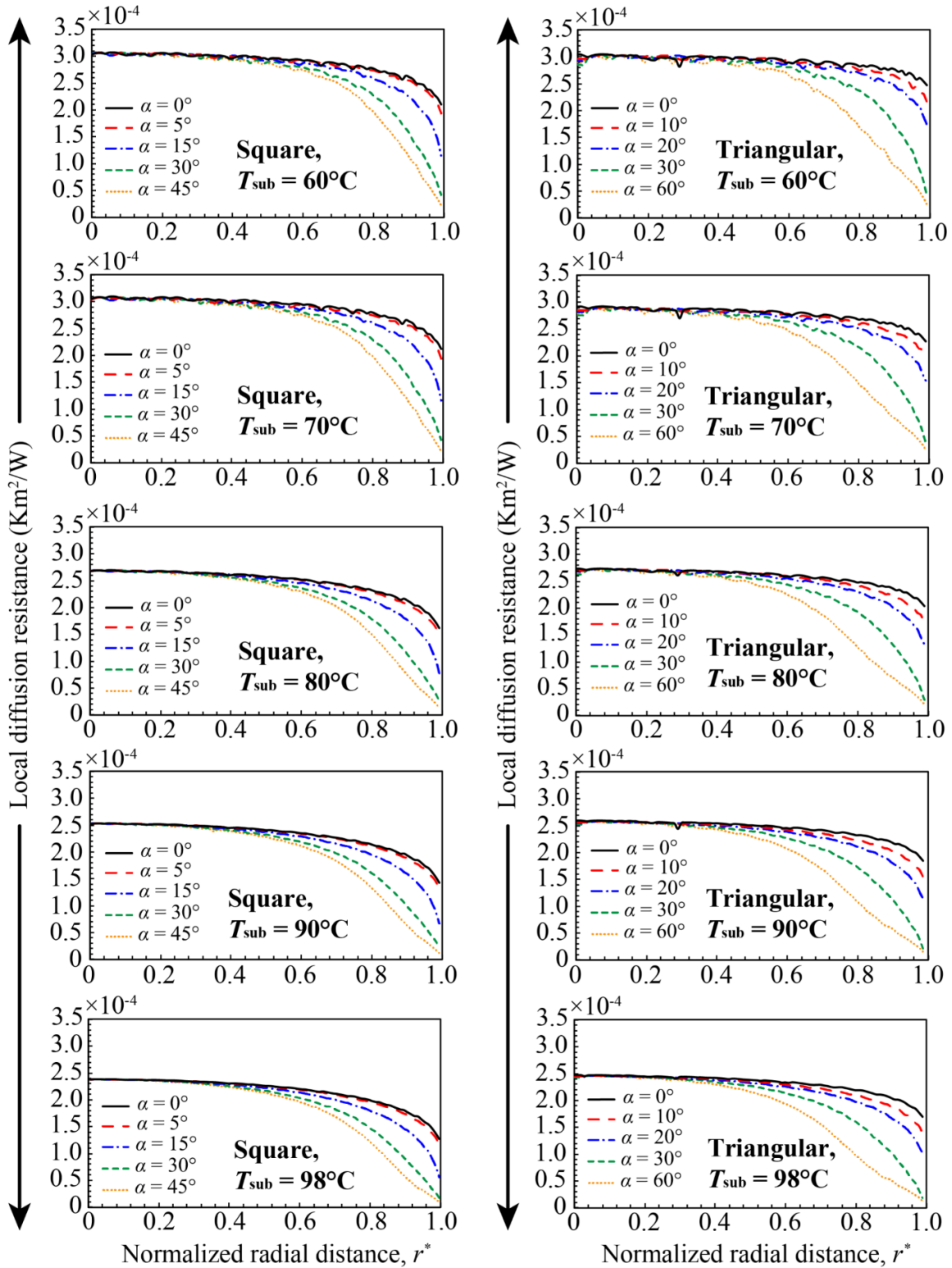


Figure 4.11 The radial distribution of the local diffusion resistance taken at cross-section planes with different azimuthal angles in an evaporating droplet on a square and triangular micropillar under different substrate temperatures.

Different from the conduction resistance which remains relatively constant at different temperature conditions, the diffusion thermal resistance is highly dependent on the substrate temperature of the evaporating droplet. As shown in Figure 4.11, for both triangular and square pillar microdroplets, raising the substrate temperature from 60°C to 98°C results in a 19% and 67% reduction in the maximum and minimum local diffusion resistances at the top center and contact line region, respectively. The larger decrease in the diffusion resistance at the contact line is attributed to a higher local liquid-vapor interfacial temperature as shown in Figure 4.9. Nevertheless, comparing Figure 4.10 and Figure 4.11, it is evident that the diffusion resistance, which ranges from 10^{-5} ~ 10^{-4} K·m²/W for the droplets on both the square and triangular micropillars, is almost an order of magnitude greater than the conduction resistance (ranges from 10^{-6} ~ 10^{-5} K·m²/W) at the same location under different substrate temperature conditions. Taking the droplet evaporating on the triangular micropillar at 98°C for example, the diffusion thermal resistance at the top center of the droplet is 2.43×10^{-4} K·m²/W, which is more than 3 times the local conduction resistance of 7.34×10^{-4} K·m²/W. Such ratio keeps increasing monotonically with increasing radial distance where the conduction resistance gradually approaches zero at the contact line region. These results demonstrate that the overall evaporation heat transfer performance from these non-axisymmetric droplets is primarily affected by the diffusion rate of the molecules from the surface of the droplet to the ambient environment under all temperature conditions.

As shown in Figure 4.10 and Figure 4.11, both the minimum conduction and diffusion resistances are located at the contact line region. Because the square and triangular micropillars exhibit a larger perimeter-to-area ratio than the circular micropillar, droplets on square and triangular micropillars exhibit a larger fraction of evaporating area in the contact line region

which yields smaller average conduction and diffusion resistances over the entire droplet. A comparison of the resistances for each droplet case is performed by calculating the average conduction and diffusion resistance using the following equations:

$$R_{cond,avg} = \frac{T_{sub,avg} - T_{lv,avg}}{J \cdot h_{fg}} \quad (4.7)$$

$$R_{diff,avg} = \frac{T_{lv,avg} - T_{\infty}}{J \cdot h_{fg}} \quad (4.8)$$

where, $T_{sub,avg}$ and $T_{lv,avg}$ are the average temperatures of the substrate and liquid-vapor interface, respectively; and J is the evaporative flux. The results are shown in Figure 4.12 and Table 4.3.

As shown in the figure, the average diffusion resistance of droplets evaporating on a triangular micropillar is around 56% and 21% smaller than those on a circular and square micropillar, respectively, at a substrate temperature of 60°C. These ratios increase slightly to 68% and 28%, respectively, as the substrate temperature rises to 98°C. In other words, the difference in the diffusion resistance becomes smaller between droplets with different shapes at higher temperature conditions. More importantly, the magnitude of the average diffusion resistance becomes closer to the conduction resistance for all droplets with increasing temperature.

Therefore, while diffusion transport is still the primary mode of heat transfer during evaporation, the role of thermal conduction inside the droplet becomes increasingly important at higher temperature. For example, the fraction of conduction resistance in the total thermal resistance increases from 19.1% to 27.0% for a droplet evaporating on a triangular micropillar as the substrate temperature increases from 60 to 98°C, as shown in Table 4.3. Nevertheless, it is noticed that the total thermal resistance for a droplet evaporating on a circular micropillar is always more than 2 times that on a triangular micropillar and this ratio increases slightly when the temperature approaches the boiling point. This finding is consistent with the evaporation flux

results shown in Table 4.3, where the percentage difference between droplets evaporating on three different micropillars remains relatively constant with increasing temperature. In other words, the impact of droplet shape on the evaporation heat transfer performance is significant under different temperature conditions.

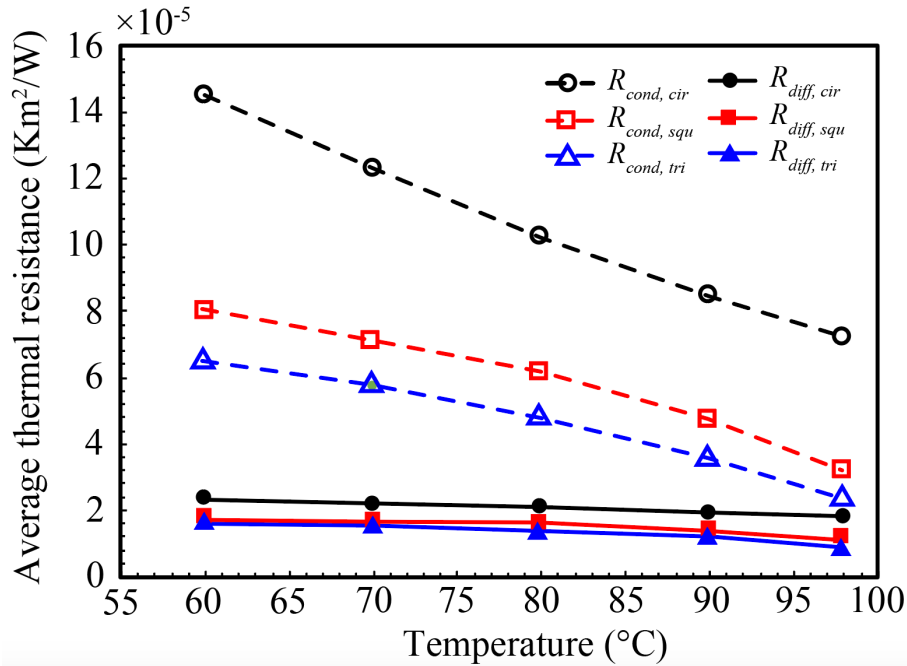


Figure 4.12 The change in the average conduction and diffusion thermal resistances for droplets evaporating on circular, square, and triangular micropillars at five different temperatures.

Table 4.3. The change in the conduction and diffusion resistances for droplets with different shapes evaporating at different substrate temperature conditions.

Temp (°C)	$R_{cond,avg}$ ($\times 10^{-5}$ K·m ² /W)			$R_{diff,avg}$ ($\times 10^{-5}$ K·m ² /W)			R_{tot} ($\times 10^{-5}$ K·m ² /W)			$\frac{R_{cond,avg}}{R_{tot}}$		
	Cir.	Squ.	Tri.	Cir.	Squ.	Tri.	Cir.	Squ.	Tri.	Cir.	Squ.	Tri.
60	2.26	1.66	1.50	14.49	7.99	6.37	16.75	9.65	7.87	13.5%	17.2%	19.1%
70	2.14	1.56	1.47	12.29	7.05	5.69	14.43	8.61	7.16	14.8%	18.1%	20.5%
80	2.01	1.63	1.33	10.21	6.09	4.68	12.22	7.73	6.01	16.4%	21.2%	22.2%
90	1.88	1.33	1.12	8.45	4.65	3.49	10.33	5.98	4.61	18.2%	22.2%	24.3%
98	1.76	1.04	0.84	7.19	3.15	2.27	8.96	4.18	3.11	19.7%	24.8%	27.0%

4.2.5 Summary

In this section, a comprehensive analysis of evaporation heat transfer performance from asymmetric microdroplets pinned on the edge of microfabricated pillar structures was performed. Surface evolver simulations were used to predict the volume and maximum height of three shapes of microdroplets. A constant pressure drive system was used to replenish the evaporated water and maintain a stable evaporating droplet under different substrate temperature conditions. Our experimental data demonstrate that for microdroplets evaporating on a substrate at 60°C, the evaporation flux of microdroplets on a triangular micropillar is 8% larger than that on a square micropillar and 45% larger than that of a circular pillar microdroplet. When the substrate temperature was raised to 98°C, the enhancement in the heat transfer coefficient for the microdroplet evaporating on a triangular micropillar is 46% and 71% larger than that on a square and circular micropillar. Under all temperature conditions, the highest vapor concentration is observed near the solid-liquid-vapor contact line which results from the higher liquid-vapor temperature. Since the droplets deposited on square and triangular micropillars exhibit a larger perimeter-to-area ratio, a greater percentage of evaporation occurs in the contact line region for droplets on the triangular and square micropillar, which results in a higher evaporation heat transfer performance. In addition, the asymmetric geometric feature yields a larger surface curvature for droplets on the square and triangular micropillars, which also contributes to a larger vapor diffusion rate from the droplet surface. Finally, the thermal resistance analysis demonstrates that the overall heat transfer performance of an evaporating droplet on a heated substrate is dominated by the vapor diffusion rate from the saturated liquid-vapor interface. Future experimental and numerical evaporation studies with a greater variety of droplet geometries and ambient conditions will be required to obtain more quantitative relationships between the evaporation thermal transport behavior and the geometric parameters.

4.3 Spray ejection from an array of micronozzles

In this section, an open experimental platform with a continuously variable liquid reservoir height was used to enable dynamic adjustment of operating parameters and investigate the overall spray behavior of the ultrasonic droplet generation using bulk acoustic waves (BAW). Not only does the experimental platform allow for real-time spray optimization, but reservoir height(s) can be predetermined to achieve operation at alternating drive frequencies (e.g., to tune the droplet size). Computational modeling is used to predict the harmonic response and to assess performance regarding the uniformity of the reservoir pressure distribution and tip pressure gradient. Model and experimental results are compared for microarrays with three orifice sizes (10 μm , 20 μm , and 40 μm), reservoirs with heights from 0.5 mm to 3 mm, and a range of operating frequencies from \sim 600 kHz to 2.20 MHz. Finally, a practical improvement to the platform is introduced by incorporating a thin film separator into the liquid reservoir. The polyethylene plastic film isolates the sample from the actuator assembly using a buffer liquid, which can benefit applications involving corrosive working liquids or sensitive biological samples.

4.3.1 Experimental apparatus

The primary advance of the present work is implementation of an open experimental platform that enables a continuously variable liquid reservoir height (and thus operating frequency). The nozzle microarray was affixed to a custom-machined arm that was permanently mounted to a 95 mm optical rail (XT95RC4 and XT95B-400, Thorlabs) [Figure 4.13(a), red dotted outline]. The actuator comprised an 18 mm \times 18 mm \times 2-mm thick aluminum matching layer glued to a 28 mm \times 32 mm \times 1.5-mm thick lead zirconate titanate (PZT) piezoelectric transducer (APC 880, American Piezo Ceramics) using an epoxy adhesive (Epoxy Instant Mix, Loctite). The

actuator assembly was also affixed to a custom-machined arm that was mounted on a z-axis translation stage (XRN25P and XT95RC4, Thorlabs) [Figure 4.13 (a), yellow dashed outline] so that the PZT/Al actuator stack was centered above the nozzle array. The translation stage provided a total travel distance of 25 mm with a resolution of $\pm 25 \mu\text{m}$. The PZT transducer was held by a thin line of glue near its periphery, and a pocket in the mounting arm allowed for unconstrained motion in the thickness mode of vibration. Finally, an optional polyethylene thin film (Saran Wrap, Dow Chemical) was adhered to a swivel arm that could be inserted between the actuator assembly and the nozzle microarray as needed. The swivel arm was also mounted on a z-axis translation stage [Figure 4.13 (a), green outline]. The translation stages provided fine control of the relative positions of the actuator, polyethylene film, and nozzle microarray to prescribe the total liquid reservoir height (actuator-microarray offset) and the fraction of the liquid column above (buffer liquid) and below (sample) the film separator. A digital single-lens reflex (DSLR) camera (300 DS, Nikon) was mounted on a three-axis translation stage to capture images of the sample spraying illuminated from below by a light emitting diode (LED) panel. Mounting arms were designed with cutouts to provide unimpeded visual access to the reservoir and spray exiting the microarray.

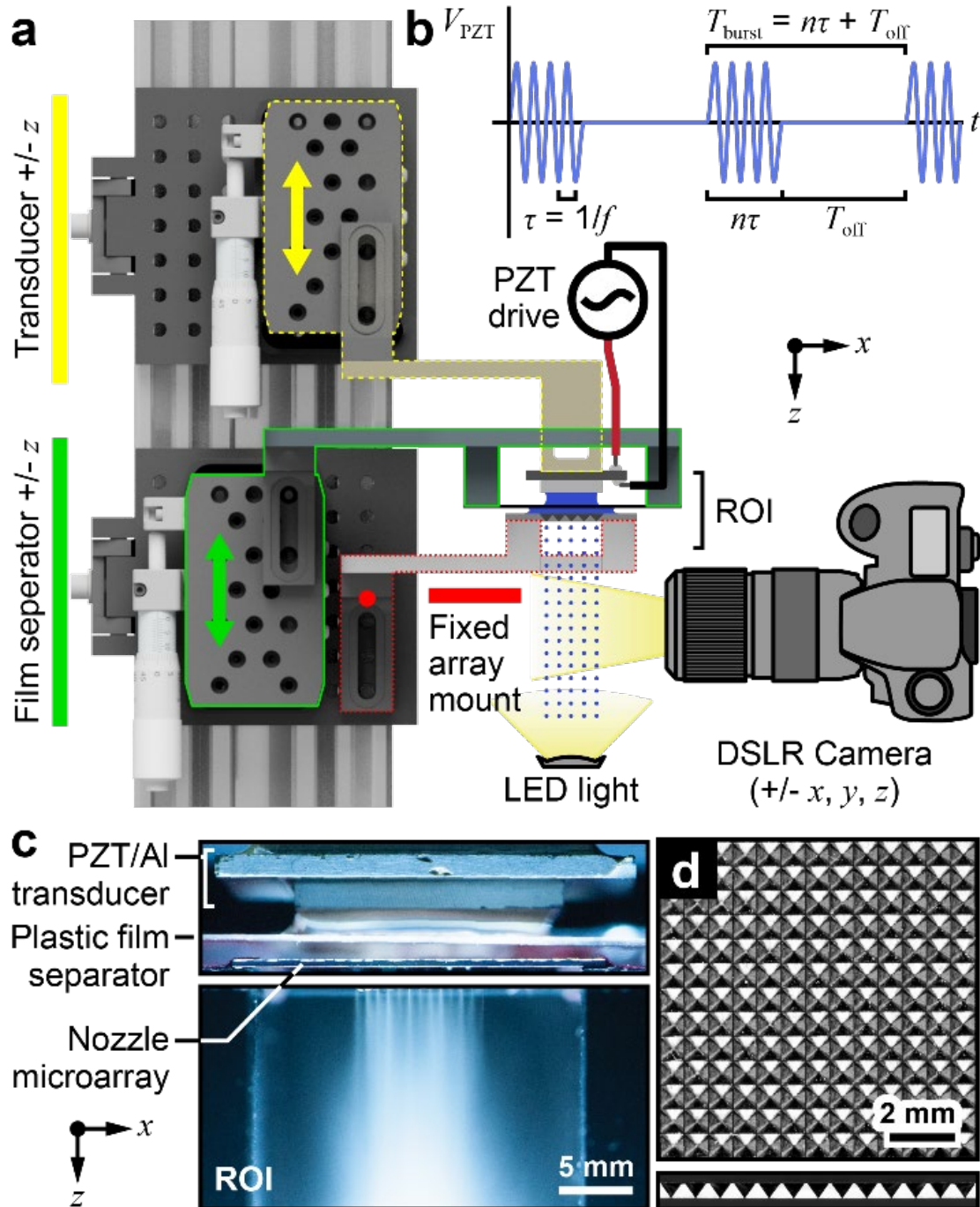


Figure 4.13 Experimental setup: (a) schematic illustrating assembly of the PZT piezoelectric/aluminum actuator, fixed nozzle microarray, and optional polyethylene thin film separator, (b) piezoelectric drive waveform V_{PZT} with burst period T_{burst} where signal is on for a period $n\tau$ and off for a period T_{off} (n is the number of cycles on; τ is the inverse of drive frequency f), (c) photograph of spraying experiment with labeled assembly components, and (d) top and side view images of the 13×13 nozzle silicon microarray.

The piezoelectric transducer was driven by an amplified sinusoidal signal (33522A, Agilent; 250L RF power amplifier, ENI), using a burst mode at 50% duty cycle to prevent excessive heating and to minimize flooding at the nozzle orifices [Figure 4.13 (b)].^{4, 76} Initially, the resonant frequencies at different liquid reservoir heights were determined by sweeping the frequency from 500 kHz to 2.5 MHz with a large input voltage of 500 mV_{pp} (amplified to between 30 V_{pp} and 150 V_{pp}) and noting frequencies at which strong ejection was observed from all the nozzles of the microarray. Then, for each reservoir height and identified resonant frequency, drive voltage was gradually increased from a subthreshold operating condition (i.e., a relatively low voltage where no ejection was observed) to a saturation condition where all the nozzles were ejecting as well-defined jets or plumes. The flexibility of the open system was demonstrated by continuously decreasing the liquid reservoir height from 3 mm to 0.5 mm at a fixed operating frequency and input voltage, again noting heights at which strong ejection was observed. Finally, the effect of incorporating a thin film separator was investigated by inserting the polyethylene film into the liquid column at different positions (i.e., to achieve different buffer liquid/sample fractions) and noting any changes in ejection quality.

In addition, COMSOL simulations were performed to get insight into the overall ejection behavior of the nozzle microarrays. The simulation methodology is the same as the one used for dynamic droplet morphology analysis in Chapter 3.2.2.

4.3.3 Results and discussion

A. Effect of orifice size on sample spraying

Three orifice diameters (10 μm , 20 μm , and 40 μm) were used to characterize the effect of orifice size on the ejection behavior. Computational modeling was used to predict the first longitudinal

resonant frequency for liquid reservoirs with height $t_{\text{res}} = 0.50$ mm and each of the three orifice diameters [Figure 4.14 (a)]. The model pressure distribution and predicted resonant frequency [$f_{\text{M}}^{(1)} = 1.06$ MHz] for each case were almost identical, confirming that the longitudinal resonance was dominated by the height of the liquid reservoir (i.e., the difference in orifice size was too small to influence the system harmonic response). The droplet generator displayed strong and stable ejection when driven at an experimental operating frequency $f_{\text{E}}^{(1)} = 1.06$ MHz and voltage $V_{\text{pp,E}} = 200$ mV [Figure 4.14 (b)]. As described earlier, the correspondence of the model-predicted resonance mode shapes and experimental droplet ejection further demonstrates the accuracy of the model.

The observed ejection modes were also visually different for the three orifice diameters. The 10 μm -orifice nozzle microarray produced a conical (plume-like) spray pattern, the 40 μm array ejected well-defined straight jets, and the 20 μm array exhibited a transitional behavior. This observation is not surprising as similar descriptions date to early investigations of jet breakup^{120, 121}. Indeed, we have reported various modes of ejection (discrete droplet, continuous jet, and transitional) from similar ultrasonic droplet generators with $\sim 4.5\text{--}16$ μm diameter orifices driven at ~ 500 kHz to 2.5 MHz^{8, 35}. Since the orifice size roughly dictates the diameter of ejected droplets, the same amount of energy is transferred to larger droplets ejected from larger orifices, yielding a lower droplet velocity; however, these larger droplets are less affected by drag from the surrounding gas⁸³⁻⁸⁶. While this fundamental understanding partially explains observations here, high resolution (in space and time) imaging at the orifice is required to confirm the exact mode of ejection^{8, 35}.

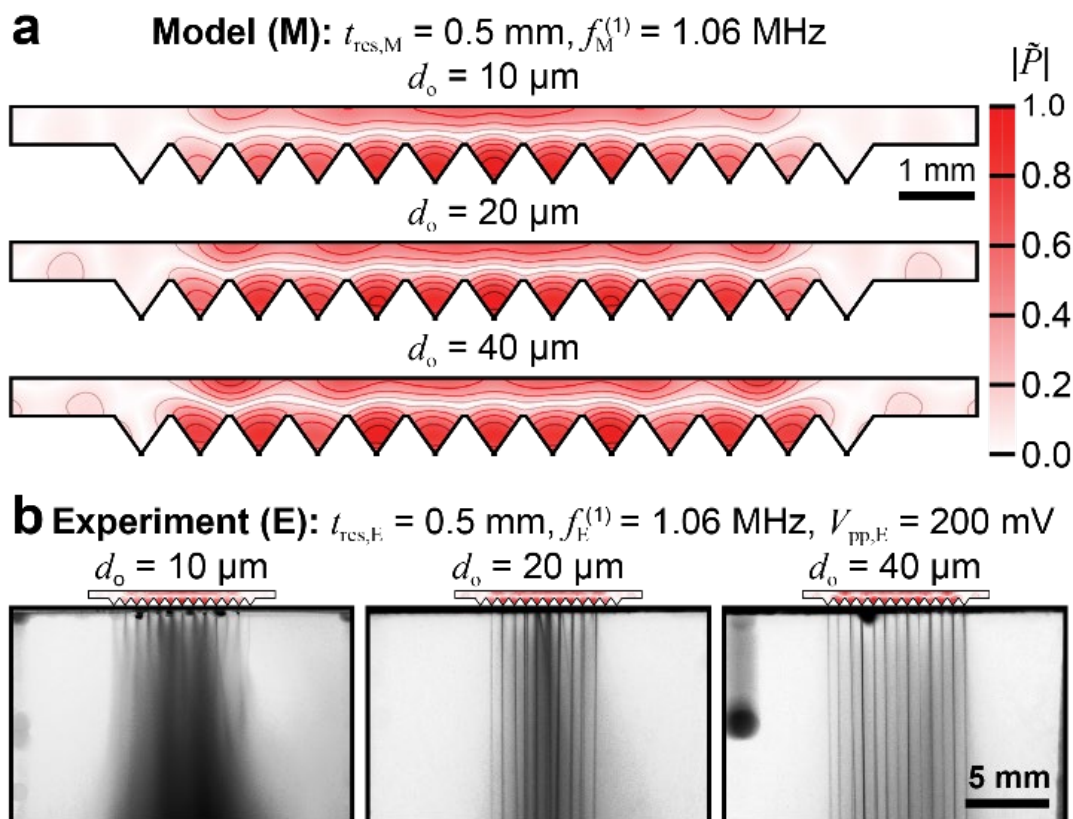


Figure 4.14 Effect of orifice size on sample spraying: (a) model (M) results showing the normalized pressure distribution within a reservoir of height $t_{\text{res},M} = 0.5$ mm with orifice diameter $d_o = 10$ μm , 20 μm , and 40 μm [the predicted first longitudinal resonant frequency $f_M^{(1)} = 1.06$ MHz for all three cases], and (b) experimental (E) images of ejection from 10 μm -, 20 μm -, and 40 μm -orifice nozzle microarrays obtained at the same operating frequency used in the simulations.

B. Identification of ejection modes for a fixed reservoir geometry

The first three longitudinal resonances for a reservoir with $t_{\text{res}} = 0.5$ mm and $d_o = 10$ μm were identified at $f_M = 1.06$ MHz, 1.60 MHz, and 2.19 MHz (see mode shapes in Figure 4.15). In the experiments, an input voltage $V_{\text{pp},E} = 300$ mV produced ejection from all nozzles at the model-predicted resonant frequencies. At these frequencies, a large pressure gradient near all orifices provided sufficient inertia for ejection to occur (with the interplay between surface tension and the oscillatory nature of the flow dictating the ejection mode)³⁵. Effective operation also requires

a uniform pressure gradient with longitudinal (z -direction) stratification throughout the reservoir. This was largely the case; however, the slightly elevated pressure gradient for the central nozzles led to stronger ejection, while ejection from the nozzles at the periphery was weaker.

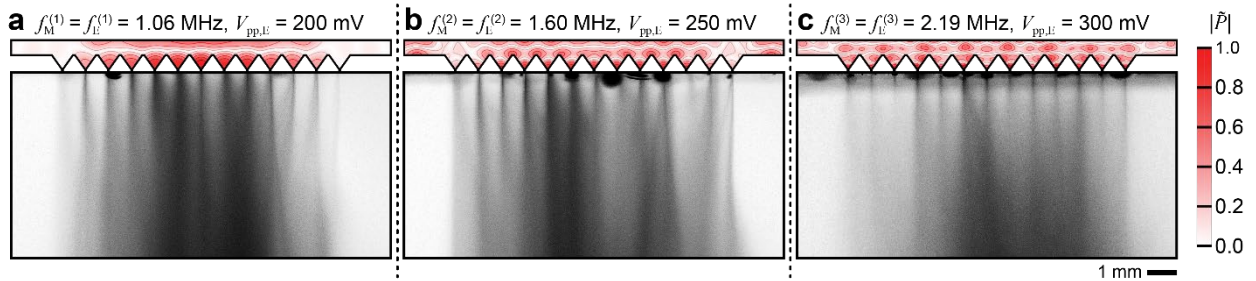


Figure 4.15 Ejection modes for a fixed reservoir geometry. Model-predicted normalized pressure distributions and experimental observation of spraying from a $t_{\text{res}} = 0.5$ mm-height reservoir with $d_o = 10$ μm orifices driven at the first three longitudinal resonances $f_M = f_E =$ (a) 1.06 MHz, (b) 1.60 MHz, and (c) 2.19 MHz. Model and experimental conditions are denoted by a subscript “M” and “E”, respectively.

The nonuniform distribution of the pressure gradient across the nozzle array shown in Figure 4.15 suggests that partial ejection (and a means of controlling sample mass flow rate) may be obtained by changing the drive amplitude. When the input voltage is sufficiently small, the pressure gradient near the orifices is not able to overcome inertia, and no liquid can escape; however, as the input voltage is slowly increased, the pressure gradient near the tips of the central nozzles will exceed the ejection threshold, while the peripheral nozzles remain in an idling mode.

To explore this concept, the piezoelectric transducer was driven at a model-predicted resonant frequency using a subthreshold input voltage (i.e., a low enough voltage that no ejection was observed). The input voltage was then increased gradually until all nozzles were ejecting. For a reservoir with $t_{\text{res}} = 0.5$ mm and $d_o = 10$ μm driven at the first longitudinal resonance [$f_M^{(1)} = f_E^{(1)} = 1.06$ MHz], three stages of ejection were observed [Figure 4.16 (a)]. For input voltages below

~60 mV_{pp}, all nozzles were in the idling mode. As the voltage reached ~60 mV, the central nine nozzles [Figure 4.16 (a), nozzles 3–11] started to eject. This observation is consistent with the model-predicted pressure distribution as these nozzles exhibited a relatively uniform, higher pressure gradient than that in the outer four nozzles. As the input voltage reached ~100 mV_{pp}, nozzles 2 and 12 began to eject, and finally, as the voltage exceeded ~200 mV_{pp}, all nozzles were active. A similar trend was seen at the second longitudinal resonant frequency [$f_M^{(2)} = f_E^{(2)} = 1.60$ MHz]; however, a single larger step from nine active nozzles to the entire array of thirteen nozzles ejecting occurred at a voltage of ~200 mV_{pp} [Figure 4.16 (b)]. Ejection from the outer four nozzles became stronger as the input voltage was further increased to 250 mV_{pp}. These results confirm that the pattern of ejecting nozzles (and potentially the mass flow rate) can be controlled by varying the amplitude of the drive signal.

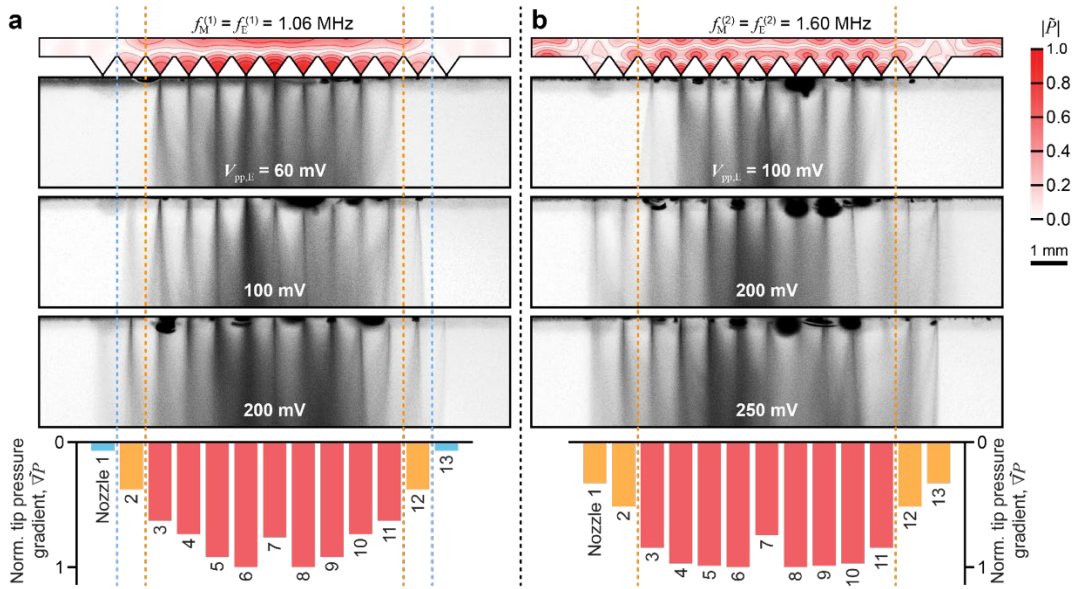


Figure 4.16 Effect of drive voltage: (a) pressure distribution, images of droplet ejection as a function of drive voltage, and model-predicted tip pressure gradients at the first longitudinal resonance of a 0.5 mm-height reservoir with orifice diameter $d_o = 10 \mu\text{m}$ [$f_M^{(1)} = f_E^{(1)} = 1.06$ MHz], and (b) results at the second longitudinal resonant frequency [$f_M^{(2)} = f_E^{(2)} = 1.60$ MHz].

C. Effect of lateral resonant frequencies

The model results indicated that large tip pressure gradients can also be obtained when lateral resonant frequencies are excited within the liquid reservoir (Figure 4.17). For example, an operating frequency $f_E = 0.630$ MHz ($f_M = 0.625$ MHz) for a 0.5 mm liquid height leads to a large pressure gradient at the center nozzle 7, while all other nozzles have small, subthreshold pressure gradients. In experiments, this resulted in a single active nozzle when driven at a voltage of 200 mV_{pp}. Similar distributed, sparse ejection behavior was also observed at $f_E = 0.808$ MHz ($f_M = 0.809$ MHz) and $f_E = 0.920$ MHz ($f_M = 0.915$ MHz), where the simulated pressure distributions indicated the presence of lateral resonance modes of shorter wavelength reducing the distance between active nozzles as the operating frequency was increased.

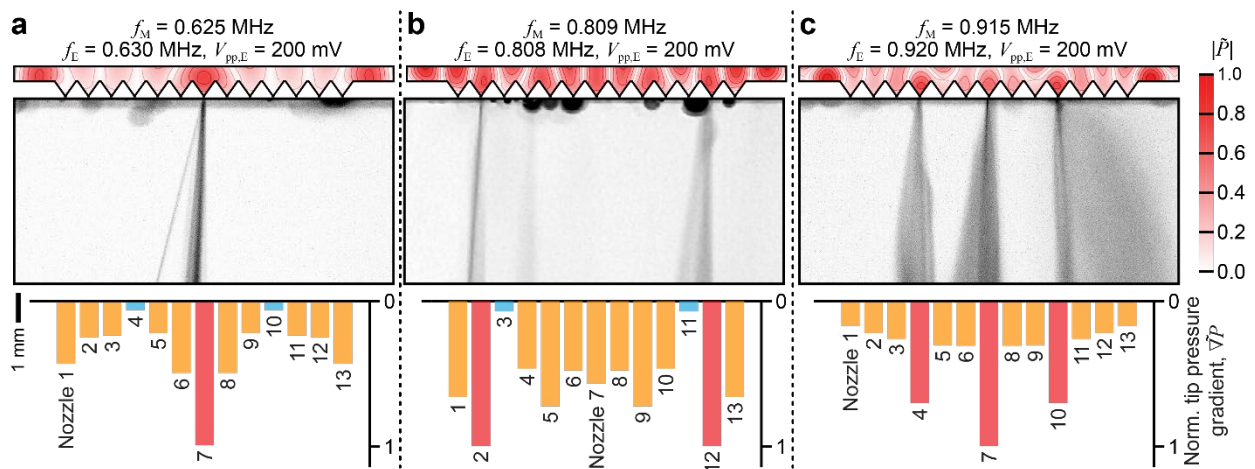


Figure 4.17 Distributed, sparse ejection driven by lateral resonant modes: (a)-(c) model-predicted normalized pressure distributions, images of droplet ejection, and model-predicted tip pressure gradients at three lateral resonances (a) $f_E = 0.630$ MHz ($f_M = 0.625$ MHz), (b) $f_E = 0.808$ MHz ($f_M = 0.809$ MHz), and (c) $f_E = 0.920$ MHz ($f_M = 0.915$ MHz). The orifice diameter $d_o = 10$ μ m and the liquid reservoir height $t_{res} = 0.5$ mm for all cases.

Although the results shown in Figure 4.17 are compelling, it is unlikely that the model exactly predicts the wave field within the chamber due to the sporadic nature of ejection when operating away from the longitudinal resonances described earlier. During an experiment, the ejection

reflecting a particular mode shape lasted for only a few seconds, after which the pattern of active nozzles would alternate between random distributions. Lateral resonances are influenced by the width of the liquid reservoir, which continuously decreases as liquid is expelled from the microarray. Thus, different pressure fields are expected to evolve over the course of an experiment. This behavior is largely absent at longitudinal resonances because the wave field is dominated by the liquid height, which is fixed by the geometry of the component assembly. Nonetheless, the ability to excite lateral resonant modes may prove useful for mass flow rate control if a continuous liquid supply is implemented to maintain a constant liquid reservoir width.

D. Multi-resonance operation via continuously varying liquid reservoir height

The PZT/Al actuator was mounted on a z-axis translation stage that allowed the liquid reservoir height to be continuously adjusted while the system was operating. As before, stable ejection patterns were obtained by operating the droplet generator at any longitudinal resonant frequency of the reservoir. Thus, when the actuator was driven at a fixed operating frequency, the resonance mode shape could be switched simply by adjusting the liquid reservoir height (e.g., to achieve a more or less uniform ejection).

An operating frequency of 1.00 MHz and an input voltage of 300 mV_{pp} were applied to the piezoelectric transducer while the liquid reservoir height was manually decreased from 3 mm to 0 mm (see Figure 4.18). For these drive conditions, all nozzles provided robust and stable ejection at four different reservoir heights, corresponding to the four longitudinal resonant modes predicted by the model: 2.73 mm (fourth longitudinal resonance), 2.09 mm (third), 1.13 mm (second), and 0.60 mm (first) (see pressure distributions in Figure 4.18).

In between the heights corresponding to longitudinal resonances, random ejection behavior was observed due to spurious system resonances or the various lateral resonances of the reservoir. A relatively large input voltage (300 mV_{pp}) was used to ensure identification of each mode, though in this experiment all modes appeared to be equally effective.

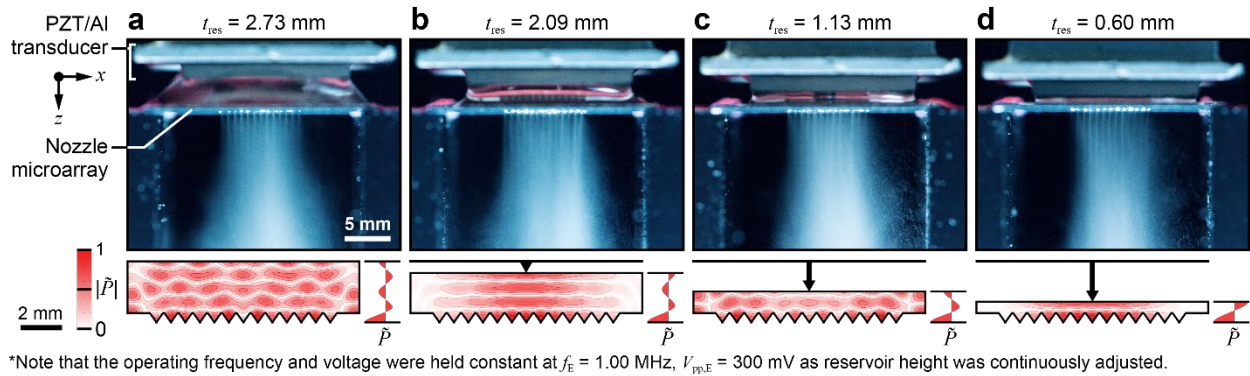


Figure 4.18 Multi-resonance operation by adjusting the liquid reservoir height: (a)-(d) images of droplet ejection and model-predicted normalized pressure distributions for excitation at $f_E = f_M = 1.00$ MHz and $V_{pp,E} = 300$ mV at gradually decreasing reservoir height: (a) $t_{res} = 2.73$ mm, (b) $t_{res} = 2.09$ mm, (c) $t_{res} = 1.13$ mm, and (d) $t_{res} = 0.60$ mm.

E. Sample isolation via insertion of a film separator

In many applications (e.g., materials synthesis with corrosive precursors or biological sample handling where sterilization is critical), it is desirable to isolate the PZT/Al actuator from the working liquid. Here, a thin plastic film can be used to separate a buffer liquid from the sample, with water contacting the aluminum coupling layer and the working fluid contacting the nozzle microarray (which is less susceptible to chemical attack, and also better suited as a single-use disposable in bio applications). The thin plastic film is acoustically transparent and should not affect the pressure field in the liquid chamber. To demonstrate this concept, a plastic polyethylene film was positioned in the water-filled reservoir at different heights as ejection was continuously monitored. A total liquid reservoir height $t_{res} = 2.0$ mm was used, and the drive

frequency and voltage were set to $f_E = 1.02$ MHz and $V_{pp,E} = 300$ mV, respectively. Figure 4.19 shows photos of ejection from the microarray without a plastic film, and for film-to-microarray distances $t_{FM} = 1.0$ mm and 1.5 mm. In each case, all nozzles are ejecting, confirming that the thin plastic film does not significantly alter the pressure distribution within the reservoir or the pressure gradient at the nozzle tips. Further, the position of the film does not seem to affect the ejection behavior. Thus, the film can be positioned very near the nozzle microarray to reduce the dead volume of the system in applications where sample is precious.

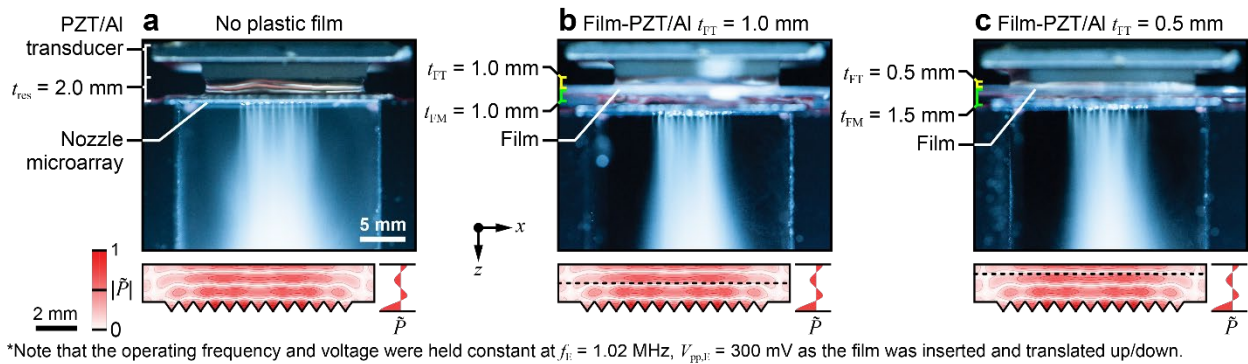


Figure 4.19 Use of a polyethylene film to bisect the liquid reservoir: (a)-(c) images of droplet ejection and model-predicted normalized pressure distributions for excitation at $f_E = f_M = 1.02$ MHz and $V_{pp,E} = 300$ mV with (a) no plastic film, and films positions such that (b) the film-to-microarray distance $t_{FM} = 1.0$ mm and (c) $t_{FM} = 1.5$ mm. The total liquid reservoir height was 2 mm in all cases.

4.3.4 Summary

In this section (4.3 Spray ejection from an array of micronozzles), a novel resonant ultrasonic droplet generator was introduced featuring an open architecture that enables a continuously variable liquid reservoir height. A comprehensive analysis was performed to show how different geometrical and operating parameters (e.g., orifice diameter, reservoir height, working frequency, and input voltage) affect system performance regarding ejection mode and uniformity. The study confirmed a previous finding that orifice diameter is too small to affect the

global pressure distribution in the liquid domain, but that different orifice sizes create sprays with different characteristics (e.g., a conical plume-like spray for $d_o = 10 \mu\text{m}$ versus well-defined, straight jets for $d_o = 40 \mu\text{m}$).

The dominant longitudinal and lateral resonances of the liquid reservoir were also investigated. Stable and robust ejection was observed at all predicted longitudinal resonances, while unstable, weak (and irregularly distributed) ejection was seen at resonances resembling predicted lateral resonance mode shapes. This result confirms that longitudinal resonances are preferred for most applications due to consistent, predictable performance; however, we also believe that less effective modes of operation can expand the potential mass flow rate range available to a microarray of a given size. If a continuous sample feed stabilizes the liquid reservoir width, lateral resonances may be used to achieve ejection from one to a few orifices of a larger array. Input voltage amplitude and reservoir height (by dictating available resonant frequencies) provide additional means to control the pattern of ejecting nozzles and mass flow rate. The ability to operate across a wide frequency spectrum enables tuning of the droplet size and size distribution (which are known to depend on frequency of operation)^{4, 8, 35}. Finally, a plastic film positioned within the reservoir of the droplet generator separated the liquid reservoir into buffer liquid and sample layers without altering the pressure field. These final demonstrations will prove useful for future applications in materials synthesis, combustion, and biological sample preparation as sample isolation is critical for corrosive working liquids and sensitive biomolecules and cells. In addition, real-time control over the droplet size and size distribution can enable spray tuning for desired micro-/nanoparticle production or graded fuel combustion.

Chapter 5: Future work for the investigation of microdroplets under quasi-steady and dynamic states

5.1 Droplets under quasi-steady states

The study of both morphologic evolution and evaporation behavior of microdroplets pinned at hollow micropillars at quasi-steady state has been performed. However, the heat removal rate generated from the single droplet evaporation is too small for real-world applications. Therefore, an array of hollow micropillars that has steadily pinned droplets can yield a larger heat transfer rate and may be used for thermal management of high heat flux sources. Still, some challenges need to be overcome before such implementation in a real-world application, and a thorough investigation of the heat transfer performance of hollow micropillar arrays must be performed, including both computational modeling and experimental validation. Some challenges and the direction of the future work related to quasi-steady state microdroplets are listed in the following sections.

5.1.1 Modification of micropillars' wettability

The current research was focused on the droplet morphology of bare silicon micropillars. The intrinsic contact angles of DI water and Novec 7500 on the substrate were $\sim 67^\circ$ and $\sim 0^\circ$, respectively. Therefore, water droplets were relatively hard to expand on the top surface while the largest liquid-gas interfacial area for the dielectric liquid was significantly small. To reduce the energy required during the expanding stage and increase the liquid-gas area of the pinned droplets, a biphilic surface can be used with a hydrophilic surface near the central through holes and a hydrophobic surface near the pillar edges. The liquids would be expanded more easily on the hydrophilic surface as they are pumped out and form a larger contact angle at the pillar edges

due to the constraints of hydrophobic surfaces.

5.1.2 Optimization of a micropillar array

The evaporation of a microdroplet is dictated by the vapor concentration gradient near the liquid-vapor interface. The vapor concentration decreases linearly from the interface to far-field when only one droplet is evaporating, and transport is dominated by the diffusion coefficient.

However, when an array of droplets evaporate at the same time, the high vapor concentration caused by the evaporation of nearby droplets would suppress the evaporation of individual droplets, therefore, hindering the overall evaporation rate and heat transfer performance. The decrease in the overall heat transfer rate is closely related to the distance between two micropillars. A smaller distance results in a larger decrease in the heat transfer performance of individual droplets. However, it will also increase the total number of micropillars in the array. Optimization of the array must be performed, considering both effects to find the best array design.

5.2 Droplets under dynamic states

In the current study, both macroscopic ejection behavior of the whole nozzle microarray and the microscopic ejection behavior of the central nozzle in the array were investigated separately.

There are still some investigations required for the full understanding of the ejection mechanism and the practical implementation of this technology in real applications. In addition, to thoroughly understanding the observed ejection behavior at both scales, the microscopic and macroscopic visualizations need to be performed at the same time while the nozzle microarray is actuated. The direction of related future work is discussed in the following sections.

5.2.1 Ejection behavior of other nozzles of the microarray

To get more insight into the nozzle microarray ejection behavior and mechanism, the

investigation of only the central nozzle is not enough. A thorough investigation of other nozzles in the microarray must also be performed microscopically to identify ejection modes, droplet sizes, and liquid velocities as a function of nozzle position, in addition to drive voltage and operating frequency. To avoid blocking of the visualization field, the central row of the microarray can be fabricated with desired sizes and all other nozzles can have a smaller orifice size ($\sim 1 \mu\text{m}$). The same experimental setup can be used for this study. Since the pressure gradient near the orifices (i.e., induced liquid inertia) is different across the microarray, the required energy inputs for the liquid to eject and the ejected liquid velocities are expected to be different for a given input voltage. In addition, the ejected droplet sizes from different orifices might also differ. Therefore, a thorough investigation of the ejection behavior of all nozzles will help to understand the fundamental ejection mechanism and overall performance of a nozzle microarray.

5.2.2 Ejection at lateral resonances

As mentioned in Chapter 4, when the nozzle microarray was actuated at lateral resonances, only selected nozzles that had a larger pressure gradient exhibited ejection while all other nozzles were in an idling mode. This ejection behavior provides a potential to control the mass flow rate of the working liquid, however, the ejection was unstable due to the constantly shrinking reservoir width as sample was ejected. To explore this potentiality, a closed liquid reservoir can be adopted with a continuous liquid supply while ejecting. This setup would enable a steady pressure field in the liquid reservoir while the nozzle microarrays are actuated. In addition, after fully characterizing the ejection behavior of all nozzles, selected nozzles can be actuated at lateral frequencies to realize more controllability over the ejected droplet sizes, velocities, and mass flow rate.

References

- ¹J. Ho, Y. Huang, M. K. Danquah, H. Wang and G. M. Forde European journal of pharmaceutical sciences **39**, (2010).
- ²J.-W. Kim, Y. Yamagata, M. Takasaki, B.-H. Lee, H. Ohmori and T. Higuchi Sensors and Actuators B: Chemical **107**, (2005).
- ³J. M. Meacham, K. Durvasula, F. L. Degertekin and A. G. Fedorov Scientific reports **8**, (2018).
- ⁴V. G. Zarnitsyn, J. M. Meacham, M. J. Varady, C. Hao, F. L. Degertekin and A. G. Fedorov Biomedical Microdevices **10**, (2008).
- ⁵Y. Lu, C. Kacica, S. Bansal, L. M. Santino, S. Acharya, J. Hu, C. Izima, K. Chrulski, Y. Diao and H. Wang ACS Applied Materials & Interfaces **11**, (2019).
- ⁶B. Joshi, J. Kaur, E. Khan, A. Kumar and A. Joshi Journal of Drug Delivery Science and Technology, (2020).
- ⁷I. Ibrahim, T. Farag, M. Abdel-baky, A. Abd El-samed and H. Gad Energy Reports **6**, (2020).
- ⁸J. Meacham, M. Varady, D. Esposito, F. L. Degertekin and A. G. Fedorov Atomization and sprays **18**, (2008).
- ⁹H. Chen, W.-l. Cheng, Y.-h. Peng, W.-w. Zhang and L.-j. Jiang International Journal of Heat and Mass Transfer **103**, (2016).
- ¹⁰W. He, Z. Luo, X. Deng and Z. Xia Heat and Mass Transfer, (2019).
- ¹¹A. G. Fedorov and J. M. Meacham IEEE Transactions on Components and Packaging Technologies **32**, (2009).
- ¹²D. H. Sharp, (Los Alamos National Lab., NM (USA), 1983).
- ¹³B. Edwards, J. Lesnick, J. Wang, N. Tang and C. Peters Journal of Laboratory Automation **21**, (2016).
- ¹⁴E. K. Sackmann, L. Majlof, A. Hahn-Windgassen, B. Eaton, T. Bandzava, J. Daulton, A. Vandenbroucke, M. Mock, R. G. Stearns and S. Hinkson Journal of laboratory automation **21**, (2016).
- ¹⁵P. Wu, C. Noland, M. Ultsch, B. Edwards, D. Harris, R. Mayer and S. F. Harris Journal of Laboratory Automation **21**, (2016).
- ¹⁶S. Marqus, L. Lee, T. Istivan, R. Y. K. Chang, C. Dekiwadia, H.-K. Chan and L. Y. Yeo European Journal of Pharmaceutics and Biopharmaceutics, (2020).
- ¹⁷L. Alhasan, A. Qi, A. R. Rezk, L. Y. Yeo and P. P. Chan Integrative Biology **8**, (2016).
- ¹⁸B. de Heij, B. van der Schoot, H. Bo, J. Hess and N. F. de Rooij Sensors and Actuators A: Physical **85**, (2000).
- ¹⁹T. S. Last, N. Roxhed and G. Stemme Journal of Microelectromechanical Systems **29**, (2020).
- ²⁰F. Zabihi and M. Eslamian Journal of Coatings Technology and Research **12**, (2015).
- ²¹L. E. Murr and W. L. Johnson Journal of Materials Research and Technology **6**, (2017).
- ²²A. D. Graham, S. N. Olof, M. J. Burke, J. P. Armstrong, E. A. Mikhailova, J. G. Nicholson, S. J. Box, F. G. Szele, A. W. Perriman and H. Bayley Scientific Reports **7**, (2017).
- ²³I. Fraunhofer Journal of Ceramic Science and Technology **8**, (2016).
- ²⁴J. Plog, Y. Jiang, Y. Pan and A. Yarin Additive Manufacturing **36**, (2020).
- ²⁵X. Li, J. M. Zhang, X. Yi, Z. Huang, P. Lv and H. Duan Advanced Science **6**, (2019).
- ²⁶D. D. Agonafer, H. Lee, P. A. Vasquez, Y. Won, K. W. Jung, S. Lingamneni, B. Ma, L. Shan, S. Shuai and Z. Du Journal of colloid and interface science **514**, (2018).
- ²⁷J. Berthier, F. Loe-Mie, V.-M. Tran, S. Schoumacker, F. Mittler, G. Marchand and N. Sarrut Journal of colloid and interface science **338**, (2009).

- ²⁸A. Cassie and S. Baxter Transactions of the Faraday society **40**, (1944).
- ²⁹J. W. Gibbs, *Scientific Papers: Thermodynamics* (Dover Publications, 1961).
- ³⁰J. Li, L. Shan, B. Ma, X. Jiang, A. Solomon, M. Iyengar, J. Padilla and D. Agonafer Journal of colloid and interface science **555**, (2019).
- ³¹B. Ma, L. Shan, B. Dogruoz and D. Agonafer Langmuir **35**, (2019).
- ³²L. Shan, J. Li, B. Ma, X. Jiang, B. Dogruoz and D. Agonafer Experimental Thermal and Fluid Science **109**, (2019).
- ³³A. H. Lefebvre and V. G. McDonnell, *Atomization and sprays* (CRC press, 2017).
- ³⁴J. Meacham, C. Ejimofor, S. Kumar, F. Degertekin and A. Fedorov Review of scientific instruments **75**, (2004).
- ³⁵J. Meacham, M. Varady, F. Degertekin and A. Fedorov Physics of fluids **17**, (2005).
- ³⁶J. M. Meacham, Georgia Institute of Technology, 2006.
- ³⁷K. X. Steirer, J. J. Berry, M. O. Reese, M. F. van Hest, A. Miedaner, M. W. Liberatore, R. Collins and D. S. Ginley Thin Solid Films **517**, (2009).
- ³⁸T. Kaydanova, A. Miedaner, J. D. Perkins, C. Curtis, J. L. Alleman and D. S. Ginley Thin Solid Films **515**, (2007).
- ³⁹C. Curtis, D. Schulz, A. Miedaner, J. Alleman, T. Rivkin, J. Perkin and D. Ginley MRS Online Proceedings Library Archive **676**, (2001).
- ⁴⁰G. Faeth, *Proceedings of Symposium (international) on combustion*, (Elsevier).
- ⁴¹F. A. Williams The physics of fluids **1**, (1958).
- ⁴²B. Abramzon and W. Sirignano International journal of heat and mass transfer **32**, (1989).
- ⁴³J. Yu and D. Kim Journal of nanoscience and nanotechnology **12**, (2012).
- ⁴⁴S. S. Yoo, H. L. Cho, O. N. Kwon, S. H. Nam, Y. G. Chang, K. Y. Kim, S. Y. Cha, B. C. Ahn and I. J. Chung Journal of Information Display **6**, (2005).
- ⁴⁵J. H. Lee, S. J. Na, C. D. Yoo and Y.-S. Kim Sensors and Actuators A: Physical **148**, (2008).
- ⁴⁶S. Joshi, H. Zuilhof, T. A. van Beek and M. W. Nielen Analytical chemistry **89**, (2017).
- ⁴⁷E. Dubuisson, V. Monnier, N. Sanz-Menez, B. Boury, Y. Usson, R. Pansu and A. Ibanez Nanotechnology **20**, (2009).
- ⁴⁸A. Battisti and R. Solaro The International Journal of Biological Markers **24**, (2009).
- ⁴⁹M. Imran and A. Bhattacharyya IEEE Sensors Journal **6**, (2006).
- ⁵⁰R. Zhong, X. Pan, L. Jiang, Z. Dai, J. Qin and B. Lin Electrophoresis **30**, (2009).
- ⁵¹K. Davitt, M. S. Pettersen and E. Rolley Langmuir **29**, (2013).
- ⁵²S. Semal, T. Blake, V. Geskin, M. J. De Ruijter, G. Castelein and J. De Coninck Langmuir **15**, (1999).
- ⁵³Y. V. Kalinin, V. Berejnov and R. E. Thorne Langmuir **25**, (2009).
- ⁵⁴Y. Zhu, Y.-X. Zhang, W.-W. Liu, Y. Ma, Q. Fang and B. Yao Scientific reports **5**, (2015).
- ⁵⁵D. Wu and C. Xu Journal of Manufacturing Science and Engineering **140**, (2018).
- ⁵⁶M. Nooranidoost, D. Izbassarov, S. Tasoglu and M. Muradoglu Physics of Fluids **31**, (2019).
- ⁵⁷H. Gudapati, M. Dey and I. Ozbolat Biomaterials **102**, (2016).
- ⁵⁸I. Gunduz, M. McClain, P. Cattani, G.-C. Chiu, J. Rhoads and S. Son Additive manufacturing **22**, (2018).
- ⁵⁹Z. Zheng, N. Kim, J. Wang, W. S. Wong and J. T. Yeow, *Proceedings of 2020 IEEE 15th International Conference on Nano/Micro Engineered and Molecular System (NEMS)*, (IEEE).
- ⁶⁰D. S. Jung, H. Y. Koo, S. E. Wang, S. B. Park and Y. C. Kang Acta Materialia **206**, (2021).
- ⁶¹J. Plateau The London, Edinburgh, and Dublin Philosophical Magazine and Journal of Science **14**, (1857).

- ⁶²N. B. Speirs, K. Langley, P. Taborek and S. T. Thoroddsen *Physical Review Fluids* **5**, (2020).
- ⁶³L. Rayleigh *The London, Edinburgh, and Dublin Philosophical Magazine and Journal of Science* **34**, (1892).
- ⁶⁴L. Rayleigh *Proc. R. Soc. London* **29**, (1879).
- ⁶⁵T. Driessen, R. Jeurissen, H. Wijshoff, F. Toschi and D. Lohse *Physics of fluids* **25**, (2013).
- ⁶⁶S. Saito, Y. Abe and K. Koyama *Nuclear Engineering and Design* **315**, (2017).
- ⁶⁷N. I. Kolev, *Multiphase Flow Dynamics 2*, (Springer, 2007).
- ⁶⁸A. Merrington and E. Richardson *Proceedings of the Physical Society (1926-1948)* **59**, (1947).
- ⁶⁹A. Haenlein, (1932).
- ⁷⁰V. Entov and A. Yarin *Journal of Fluid Mechanics* **140**, (1984).
- ⁷¹R. D. Reitz, *Atomization and other breakup regimes of a liquid jet* (Princeton University, 1978).
- ⁷²S. Chandrasekhar, *Hydrodynamic and hydromagnetic stability* (Courier Corporation, 2013).
- ⁷³J. Buckmaster *Journal of Fluid Mechanics* **61**, (1973).
- ⁷⁴J. Friend and L. Y. Yeo *Reviews of Modern Physics* **83**, (2011).
- ⁷⁵M. Kumaraswamy, S. Collignon, C. Do, J. Kim, V. Nizet and J. Friend *Applied Microbiology and Biotechnology* **102**, (2018).
- ⁷⁶J. M. Meacham, A. O'Rourke, Y. Yang, A. G. Fedorov, F. L. Degertekin and D. W. Rosen *Journal of manufacturing science and engineering* **132**, (2010).
- ⁷⁷G. T. Vladisavljević, I. Kobayashi and M. Nakajima *Microfluidics and Nanofluidics* **10**, (2011).
- ⁷⁸I. Kobayashi, T. Takano, R. Maeda, Y. Wada, K. Uemura and M. Nakajima *Microfluidics and nanofluidics* **4**, (2008).
- ⁷⁹C.-H. Lee and A. Lal *IEEE Transactions on Ultrasonics, ferroelectrics, and frequency control* **51**, (2004).
- ⁸⁰C. Pan, J. Shiea and S.-C. Shen *Journal of micromechanics and microengineering* **17**, (2007).
- ⁸¹M. Varady, L. McLeod, J. Meacham, F. Degertekin and A. Fedorov *Journal of Micromechanics and Microengineering* **17**, (2007).
- ⁸²A. D. Ledbetter, H. N. Shekhani, M. M. Binkley and J. M. Meacham *IEEE Transactions on Ultrasonics, Ferroelectrics, and Frequency Control* **65**, (2018).
- ⁸³A. U. Chen and O. A. Basaran *Physics of fluids* **14**, (2002).
- ⁸⁴G. Brenn and U. Lackermeier *Physics of fluids* **9**, (1997).
- ⁸⁵M.-C. Yuen *Journal of Fluid Mechanics* **33**, (1968).
- ⁸⁶M. Orme and E. Muntz *Review of scientific instruments* **58**, (1987).
- ⁸⁷A. Faghri, *Heat pipe science and technology* (Global Digital Press, 1995).
- ⁸⁸R. Ranjan, J. Y. Murthy and S. V. Garimella *International Journal of Heat and Mass Transfer* **54**, (2011).
- ⁸⁹E. Mason and T. Marrero, *Advances in Atomic and Molecular Physics*, (Elsevier, 1970).
- ⁹⁰X. Xu and J. Luo *Applied Physics Letters* **91**, (2007).
- ⁹¹F. Girard, M. Antoni and K. Sefiane *Langmuir* **24**, (2008).
- ⁹²M. Schmitt and H. Stark *Physics of Fluids* **28**, (2016).
- ⁹³S. Dash and S. V. Garimella *Physical Review E* **89**, (2014).
- ⁹⁴K. Gleason and S. A. Putnam *Langmuir* **30**, (2014).
- ⁹⁵R. W. Schrage, *A theoretical study of interphase mass transfer* (Columbia University Press, 1953).

- ⁹⁶H. K. Dhavaleswarapu, J. Y. Murthy and S. V. Garimella International Journal of Heat and Mass Transfer **55**, (2012).
- ⁹⁷P. Wayner Jr, Y. Kao and L. LaCroix International Journal of Heat and Mass Transfer **19**, (1976).
- ⁹⁸S. S. Panchangam, A. Chatterjee, J. L. Plawsky and P. C. Wayner Jr International Journal of Heat and Mass Transfer **51**, (2008).
- ⁹⁹R. W. Coutant and E. C. Penski Industrial & Engineering Chemistry Fundamentals **21**, (1982).
- ¹⁰⁰L. Liebermann Journal of Applied Physics **28**, (1957).
- ¹⁰¹S. M. Rowan, M. Newton and G. McHale The Journal of Physical Chemistry **99**, (1995).
- ¹⁰²M. Shanahan and C. Bourges International journal of adhesion and adhesives **14**, (1994).
- ¹⁰³P. Sáenz, A. Wray, Z. Che, O. Matar, P. Valluri, J. Kim and K. Sefiane Nature communications **8**, (2017).
- ¹⁰⁴P. Sáenz, K. Sefiane, J. Kim, O. Matar and P. Valluri Journal of Fluid Mechanics **772**, (2015).
- ¹⁰⁵S. Shuai, Z. Du, B. Ma, L. Shan, B. Dogruoz and D. Agonafer, *Proceedings of ASME 2018 International Technical Conference and Exhibition on Packaging and Integration of Electronic and Photonic Microsystems*, (American Society of Mechanical Engineers).
- ¹⁰⁶D. Foresti, K. T. Kroll, R. Amisshah, F. Sillani, K. A. Homan, D. Poulidakos and J. A. Lewis Science advances **4**, (2018).
- ¹⁰⁷W. Connacher, J. Orosco and J. Friend Physical Review Letters **125**, (2020).
- ¹⁰⁸D. Kirpalani and K. Suzuki Ultrasonics Sonochemistry **18**, (2011).
- ¹⁰⁹S. C. Tsai, S. K. Lin, R. W. Mao and C. S. Tsai Physical review letters **108**, (2012).
- ¹¹⁰C. S. Tsai, R. W. Mao, S. K. Lin, N. Wang and S. C. Tsai Lab on a Chip **10**, (2010).
- ¹¹¹G. Perçin and B. T. Khuri-Yakub Review of Scientific Instruments **73**, (2002).
- ¹¹²G. Perçin, G. G. Yaralioglu and B. T. Khuri-Yakub Review of scientific instruments **73**, (2002).
- ¹¹³G. Percin and B. T. Khuri-Yakub IEEE transactions on ultrasonics, ferroelectrics, and frequency control **49**, (2002).
- ¹¹⁴U. Demirci, G. G. Yaralioglu, E. Haeggstrom and B. Khuri-Yakub IEEE Transactions on Semiconductor Manufacturing **18**, (2005).
- ¹¹⁵Y.-R. Jeng, C.-C. Su, G.-H. Feng, Y.-Y. Peng and G.-P. Chien Microsystem Technologies **15**, (2009).
- ¹¹⁶T. Diepold, E. Obermeier and A. Berchtold Journal of Micromechanics and Microengineering **8**, (1998).
- ¹¹⁷L. Palm, L. Wallman, T. Laurell and J. Nilsson Journal of Imaging Science and Technology **44**, (2000).
- ¹¹⁸Q. Yan, W. Sun and J. Zhang Applied Sciences **10**, (2020).
- ¹¹⁹K. A. Brakke Experimental mathematics **1**, (1992).
- ¹²⁰A. Haenlein Forschung auf dem Gebiet des Ingenieurwesens A **2**, (1931).
- ¹²¹W. V. Ohnesorge ZAMM-Journal of Applied Mathematics and Mechanics/Zeitschrift für Angewandte Mathematik und Mechanik **16**, (1936).
- ¹²²Y. A. Cengel and M. A. Boles Sea **1000**, (2002).

Appendix

Appendix 1

Table A.1 Dimensionless numbers and time scales for process, inertia, capillary, and viscosity for all cases investigated experimentally.

Orifice Size ($O_d, \mu\text{m}$)	Frequency (f)	Ejection Mode	Velocity ($U, \text{m/s}$)	We	St	Re	t_f (μs)	t_U (μs)	t_σ (μs)	t_μ (μs)
5	0.5 MHz	DoD	4.42	0.68	1.13	12.38	2.00	0.57	0.47	7.01
5	0.5 MHz	DoD	6.12	1.30	0.82	17.16	2.00	0.41	0.47	7.01
5	0.5 MHz	DoD	8.53	2.53	0.59	23.92	2.00	0.29	0.47	7.01
5	0.5 MHz	DoD	11.17	4.33	0.45	31.32	2.00	0.22	0.47	7.01
5	0.5 MHz	DoD	15.77	8.64	0.32	44.22	2.00	0.16	0.47	7.01
5	0.5 MHz	Screw	30.76	32.86	0.16	86.23	2.00	0.08	0.47	7.01
5	1 MHz	DoD	12.26	5.22	0.20	34.37	1.00	0.20	0.47	7.01
5	1 MHz	DoD	14.34	7.14	0.17	40.19	1.00	0.17	0.47	7.01
5	1 MHz	DoD	15.35	8.18	0.16	43.04	1.00	0.16	0.47	7.01
5	1 MHz	DoD	16.98	10.02	0.15	47.61	1.00	0.15	0.47	7.01
5	1 MHz	DoD	17.47	10.60	0.14	48.97	1.00	0.14	0.47	7.01
5	1 MHz	Screw	22.78	18.02	0.11	63.86	1.00	0.11	0.47	7.01
5	1.6 MHz	DoD	12.56	5.48	0.32	35.21	0.63	0.20	0.47	7.01
5	1.6 MHz	DoD	13.14	6.00	0.30	36.85	0.63	0.19	0.47	7.01
5	1.6 MHz	DoD	17.93	11.16	0.22	50.26	0.63	0.14	0.47	7.01
5	1.6 MHz	DoD	21.14	15.52	0.19	59.28	0.63	0.12	0.47	7.01
5	1.6 MHz	DoD	26.20	23.83	0.15	73.44	0.63	0.10	0.47	7.01
5	1.6 MHz	Screw	34.39	41.05	0.12	96.39	0.63	0.07	0.47	7.01
5	2 MHz	DoD	14.34	7.14	0.35	40.20	0.50	0.17	0.47	7.01
5	2 MHz	DoD	18.88	12.37	0.26	52.91	0.50	0.13	0.47	7.01
5	2 MHz	DoD	22.52	17.61	0.22	63.14	0.50	0.11	0.47	7.01
5	2 MHz	DoD	24.29	20.48	0.21	68.09	0.50	0.10	0.47	7.01
5	2 MHz	DoD	26.24	23.91	0.19	73.57	0.50	0.10	0.47	7.01
5	2 MHz	DoD	27.89	27.01	0.18	78.19	0.50	0.09	0.47	7.01
5	2 MHz	Screw	36.18	45.45	0.14	101.42	0.50	0.07	0.47	7.01
10	0.5 MHz	Jet	14.10	13.77	0.18	79.03	2.00	0.85	1.32	28.03
10	0.5 MHz	Tran	17.69	21.69	0.14	99.18	2.00	0.68	1.32	28.03
10	0.5 MHz	Tran	19.41	26.11	0.13	108.82	2.00	0.62	1.32	28.03
10	0.5 MHz	Tran	20.21	28.30	0.12	113.29	2.00	0.59	1.32	28.03
10	0.5 MHz	Tran	20.04	27.82	0.12	112.34	2.00	0.60	1.32	28.03
10	0.5 MHz	Screw	29.18	59.03	0.09	163.63	2.00	0.41	1.32	28.03

10	1 MHz	Jet	24.54	41.75	0.20	137.62	1.00	0.49	1.32	28.03
10	1 MHz	Tran	26.52	48.74	0.19	148.68	1.00	0.45	1.32	28.03
10	1 MHz	Tran	29.54	60.49	0.17	165.65	1.00	0.41	1.32	28.03
10	1 MHz	Tran	29.35	59.69	0.17	164.54	1.00	0.41	1.32	28.03
10	1 MHz	Tran	31.41	68.39	0.16	176.13	1.00	0.38	1.32	28.03
10	1 MHz	Screw	32.87	74.88	0.15	184.30	1.00	0.37	1.32	28.03
10	1.5 MHz	Jet	24.63	42.06	0.30	138.12	0.67	0.49	1.32	28.03
10	1.5 MHz	Screw	27.71	53.22	0.27	155.37	0.67	0.43	1.32	28.03
10	1.5 MHz	Screw	37.27	96.26	0.20	208.95	0.67	0.32	1.32	28.03
10	2 MHz	Jet	18.87	24.68	0.53	105.79	0.50	0.64	1.32	28.03
10	2 MHz	Jet	22.18	34.09	0.45	124.34	0.50	0.54	1.32	28.03
10	2 MHz	Jet	29.43	60.03	0.34	165.01	0.50	0.41	1.32	28.03
10	2 MHz	Screw	33.83	79.31	0.30	189.67	0.50	0.35	1.32	28.03
15	0.5 MHz	Jet	7.19	5.37	0.52	60.46	2.00	1.04	2.42	63.08
15	0.5 MHz	Tran	8.31	7.17	0.45	69.86	2.00	0.90	2.42	63.08
15	0.5 MHz	Tran	10.23	10.88	0.37	86.02	2.00	0.73	2.42	63.08
15	0.5 MHz	Tran	10.94	12.44	0.34	91.99	2.00	0.69	2.42	63.08
15	0.5 MHz	Tran	10.88	12.31	0.34	91.52	2.00	0.69	2.42	63.08
15	0.5 MHz	Screw	12.23	15.56	0.31	102.90	2.00	0.61	2.42	63.08
15	1 MHz	Jet	20.16	42.24	0.37	169.52	1.00	0.37	2.42	63.08
15	1 MHz	Screw	31.01	99.97	0.24	260.80	1.00	0.24	2.42	63.08
15	1 MHz	Screw	32.89	112.45	0.23	276.60	1.00	0.23	2.42	63.08
15	1 MHz	Screw	35.71	132.56	0.21	300.31	1.00	0.21	2.42	63.08
15	1 MHz	Screw	38.53	154.31	0.19	324.02	1.00	0.19	2.42	63.08
15	1.5 MHz	Jet	19.73	40.48	0.57	165.96	0.67	0.38	2.42	63.08
15	1.5 MHz	Jet	25.37	66.92	0.44	213.38	0.67	0.30	2.42	63.08
15	1.5 MHz	J Screw	28.19	82.62	0.40	237.09	0.67	0.27	2.42	63.08
15	1.5 MHz	Screw	31.01	99.97	0.36	260.80	0.67	0.24	2.42	63.08
15	1.5 MHz	Screw	33.83	118.97	0.33	284.51	0.67	0.22	2.42	63.08
15	1.5 MHz	Screw	38.06	150.57	0.30	320.07	0.67	0.20	2.42	63.08
15	1.5 MHz	Screw	45.11	211.50	0.25	379.34	0.67	0.17	2.42	63.08
15	2 MHz	Jet	24.24	61.10	0.62	203.90	0.50	0.31	2.42	63.08
15	2 MHz	Screw	26.33	72.07	0.57	221.44	0.50	0.28	2.42	63.08
15	2 MHz	Screw	29.63	91.26	0.51	249.18	0.50	0.25	2.42	63.08
15	2 MHz	Screw	34.33	122.50	0.44	288.69	0.50	0.22	2.42	63.08
15	2 MHz	Screw	36.11	135.57	0.42	303.71	0.50	0.21	2.42	63.08

Appendix 2

Uncertainty Analysis for heat transfer experiments

1. Droplet morphology uncertainty

The microdroplets' equilibrium profiles were obtained from Surface Evolver. These profiles were then exported to COMSOL Multiphysics® for calculating the height-to-diameter or height-to-side-length ratios. However, when matching these geometric features between the experimental image and the modeling profile, it is difficult to precisely delineate the liquid-vapor interface from droplet images taken by the camera. Specifically, when determining the maximum height of the microdroplets, there was a 5-pixel uncertainty due to the blurred liquid-vapor interface, which leads to $\pm 3\%$ ($\pm 1.5 \mu\text{m}$) uncertainty for microdroplet maximum height.

2. Pt heater and RTD resistance uncertainty

The resistances of the RTD elements were calibrated in an oven at different temperatures after each sample was bonded with a NanoPort and submerged in a DI water bath to account for any decrease in temperature resulting from the in-device thermal resistance. The relationship between the electrical resistance and the temperature for different RTD elements were fitted by linear curves. By comparing the fitted value and the actual temperature provided by the oven, the uncertainty in temperature measurements by the RTD was found to be $\pm 0.3^\circ\text{C}$.

3. Evaporation rate and heat transfer coefficient

During our evaporation experiment, the microdroplet was held in constant geometry where the evaporated liquid was replenished by a continuous liquid supply through the center holes of the micropillars. Considering mass conservation and negligible compressibility of the working fluid, the total evaporation rate, \dot{m}_v must be equal to the flow rate measured by the mass flow meter, which has a standard error of $\pm 0.01 \text{ uL/min}$. The evaporation heat transfer coefficient was

$$h = \frac{m_v h_{fg}}{A_{sl}(T - T_\infty)}$$

where m_v is the total evaporation rate, A_{sl} is the solid-liquid interfacial area, T_{lv} is the liquid-vapor interfacial temperature, and T_∞ is the ambient temperature. The latent heat of vaporization, h_{fg} , was determined by the corresponding substrate temperature, T_{sub} . Errors in the solid-liquid interfacial areas for the three microdroplets resulted from the microfabrication process. By comparing the SEM images of the micropillar sample with the design feature, the error in the feature length was found to be $\pm 1 \mu\text{m}$. Combining these errors together, the accumulated heat transfer coefficient error for three shapes of microdroplets varies from 15% – 5% as the temperature increases from 60°C to 98°C. It should be noted that the primary error comes from the uncertainty in flow rate reading which becomes smaller with increasing evaporation rate under higher temperature conditions.

Appendix 3

Computational modeling for sessile droplet evaporation

To gain more insight into the evaporation transport of microdroplets on different micropillar structures and validate the experimental measurements, a Multiphysics simulation model was developed using COMSOL to predict the evaporation rate from axisymmetric and asymmetric microdroplets under different substrate temperature conditions. The evaporation process was analyzed in a steady-state condition, in which the shapes of the microdroplets and the evaporation rate were both constant over time. In the liquid domain, the heat transport is attributed to both conduction and convection. The convection current originates from three sources: (1) the continuous inlet flow from the center pore of the micropillar; (2) the buoyancy flow induced by the temperature difference between the bottom and top part of the microdroplet and (3) Marangoni flow induced by the temperature difference along the liquid-vapor interface. The magnitude of convection induced by these three sources can be assessed by calculating the Péclet number (Pe), Rayleigh number (Ra), and Marangoni number (Ma) of the evaporating droplet, respectively, based on the experimental measurement of evaporation rate and substrate temperature. In this study, all these three non-dimensionalized numbers are found to be sufficiently small such that the convective heat transfer inside the droplet is insignificant compared to heat transport by conduction. Therefore, in the liquid and solid domain, the heat transfer process is governed by the heat conduction equation given by:

$$\nabla^2 T = 0 \tag{A.1}$$

where T is the continuous temperature functions in both the liquid and solid domain. A constant temperature boundary condition, equal to the temperature used in the experiments, was assigned

to the base surface of the micropillar. In the experiments, the substrate temperature was measured by the RTD, and the distance from the RTD to the base of the micropillar was 200 μm . Given a thermal conductivity of 130 W/m-K for silicon, the temperature difference between the RTD and the bottom wall of the micropillar can be neglected. For example, the temperature difference across the micropillar is only 0.5 $^{\circ}\text{C}$ when the substrate temperature is 90 $^{\circ}\text{C}$. The vapor concentration in the gas domain is solved by the steady-state species transport equation:

$$-\vec{V} \cdot \nabla C_v + \nabla \cdot (D_{diff} \nabla C_v) = 0 \quad (\text{A.2})$$

In our study, the Rayleigh, $Ra < 0.1$. Therefore, natural convection in the gas domain is neglected. Considering that there is no forced convection in the ambient environment, the advection term found in equation (A.2) is neglected. A constant concentration boundary condition was assigned at the far-field. This concentration equals to the concentration of vapor in air where the relative humidity and temperature are 25% and 22 $^{\circ}\text{C}$, respectively. A no-penetration (i.e. zero diffusive flux) conditions were assigned to the solid-vapor interfaces. During the simulation, the thermal and vapor concentration boundary conditions at the liquid-vapor interface are obtained by an iterative process which couples the solution of the temperature field to the concentration fields by

$$k_l \left(\frac{\partial T}{\partial \vec{n}} \right)_{lv} = D_{diff} h_{fg} \left(\frac{\partial C_v}{\partial \vec{n}} \right)_{lv} \quad (\text{A.3})$$

$$C_{v,lv} = C_{sat}(T_{lv}) \quad (\text{A.4})$$

Where k_l is the thermal conductivity of water, h_{fg} is the latent heat of vaporization, D_{diff} is the air-vapor molecular diffusion coefficient, and $C_{v,lv}$ is the vapor concentration at the liquid-vapor interface. The left term in equation (7) represents the conduction heat flux at the liquid-vapor

interface while the right term represents the evaporation heat transfer associated with the vapor diffusion at the liquid-vapor interface. The saturation concentration shown in equation (A.4) can be derived based on the Clausius-Clapeyron equation and ideal gas law given by

$$p_{sat}(T_{lv}) = p_{sat_{ref}} \exp \left[\frac{\bar{M} h_{fg}}{\bar{R}} \left(\frac{1}{T_{sat_{ref}}} - \frac{1}{T_{lv}} \right) \right] \quad (\text{A.5})$$

$$pV = nRT \quad (\text{A.6})$$

where p_{sat} is the saturation pressure at the liquid-vapor interface, T_{lv} is the liquid-vapor interfacial temperature, $p_{sat_{ref}}$ is the saturation pressure associated with a reference temperature of $T_{sat_{ref}}$, \bar{M} is the molar mass, and \bar{R} is the universal gas constant. Based on equation (A.5) and (10), the saturation concentration can be derived by

$$c_{sat}(T_{lv}) = \frac{n_{sat}(T_{lv})}{V} = \frac{p_{sat}(T_{lv}) \cdot V / R \cdot T_{lv}}{V} = \frac{p_{sat_{ref}}}{\bar{R} \cdot T_{lv}} \exp \left[\frac{\bar{M} h_{fg}}{\bar{R}} \left(\frac{1}{T_{sat_{ref}}} - \frac{1}{T_{lv}} \right) \right] \quad (\text{A.7})$$

While the ideal gas law is most accurate at high temperature and low pressure, the saturated vapor concentration calculated by equation (9) was found to be in good agreement with the literature data (less than 2% error)¹²². Table 2 summarizes the simulation parameters and the details of the solution method. Fig. 8 shows the schematic representation of the boundary conditions used in the simulations. The far-field shape of the vapor domain is a hemisphere, set as 100 times larger than the characteristic length of the microdroplet ($\sim 100 \mu\text{m}$). To simplify the simulations and reduce computational time, symmetrical boundaries were used for the triangular and square microdroplets. In other words, only 1/6 of triangular microdroplets 1/8 of the square microdroplets were simulated in our model as shown in our previous work¹⁰⁵. The microdroplets' shapes were imported from Surface Evolver.

Table A.2. Simulation setup.

Input parameters	Value		
Outer diameter, D	100 μm		
Inner diameter, d	25 μm		
Interfacial area, A_{lv}	$1.2 \times 10^{-8} \text{ m}^2$		
Perimeter, L	$3.14 \times 10^{-4} \text{ m}$		
Operating pressure, p_{amb}	101325 Pa		
Solution methods	Setup		
Mesh type	Tetrahedral		
Number of cells	Circular	Triangular	Square
	189,219	3,653,713	3,49,3573
Study type	Stationary		
Solver	Segregated		
Geometric Multigrid Solver	GMRES		
Preconditioning	Left		

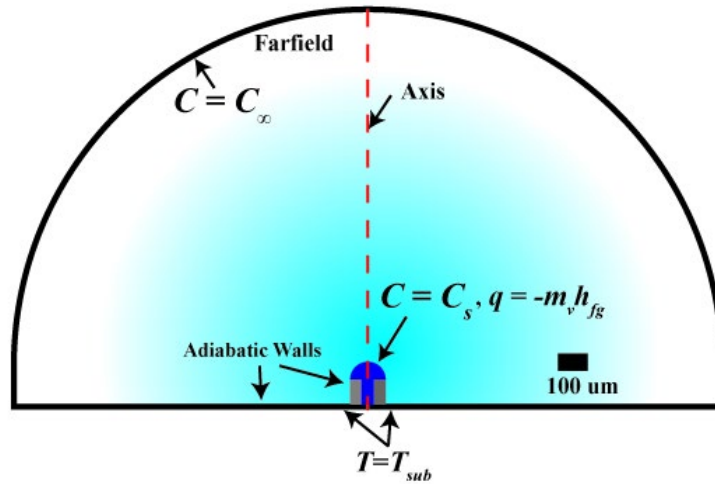


Figure A.1 The boundary conditions for the numerical simulation of microdroplets evaporating on heated micropillars. At far field, the vapor concentration and the temperature are assigned as the ambient condition (the relative humidity and temperature are 25% and 22°C); a vapor concentration boundary condition was assigned at the liquid-vapor interface, which equals to the local saturation concentration; a constant temperature boundary condition is applied at the pillar bottom surface; and all other walls are assigned as no-penetration boundary condition.

A mesh independent study was conducted to investigate the influence of mesh size on the evaporation rate. As shown in Table 3, for triangular microdroplets, four levels of mesh with different element sizes (1.0 μm , 0.5 μm , 0.3 μm , and 0.2 μm) were generated for the mesh independence study. The total evaporation rates for the coarse, medium, fine, and finest meshes were 1.15×10^{-10} kg/s, 1.17×10^{-10} kg/s, 1.18×10^{-10} kg/s, and 1.1985×10^{-10} kg/s, respectively. The difference in the rate for fine mesh and the finest mesh was only 1.5%. Therefore, the fine mesh with a element size of 0.3 μm was finally used for conducting the simulations.

Table A.3 Mesh independence study.

Mesh size	Coarse	Medium	Fine	Finest
	1.06 million	1.38 million	2.58 million	4.05 million
Max element size on droplet surface (μm)	1.0	0.5	0.3	0.2
Evaporation rate (kg/s)	1.15×10^{-10}	1.17×10^{-10}	1.18×10^{-10}	1.19×10^{-10}
Variation with respect to 'Finest' mesh	3.7%	2.8%	1.5%	0%